

Fluoridation of Hydroxyapatite: A Physicochemical View on Caries Prophylaxis via Fluoride Application

Dissertation

zur Erlangung des Grades
des Doktors der Naturwissenschaften
der Naturwissenschaftlich-Technischen Fakultät
der Universität des Saarlandes

von

Thomas Faidt

Saarbrücken

2019

Tag des Kolloquiums: 13. Dezember 2019

Dekan: Univ.-Prof. Dr. rer. nat. Guido Kickelbick

Berichterstatter: Univ.-Prof. Dr. rer. nat. Karin Jacobs
Univ.-Prof. Dr. med. dent. Matthias Hannig
Univ.-Prof. Dr. rer. nat. Rudolf Merkel

Vorsitz: Univ.-Prof. Dr.-Ing. Michael Vielhaber

Akad. Mitarbeiter: Dr. Michael Jung

Abstract

Since decades the application of fluoride containing dental health care products is a well established method in caries prophylaxis. According to current knowledge, fluoridation supports the remineralization of damaged enamel, inhibits demineralization of enamel by decreasing its demineralization-threshold, and decreases adhesion forces of bacteria.

However, the exact mechanisms of fluoride uptake in the mineral component of tooth enamel, i.e., hydroxyapatite (HAp), are not yet completely understood. Therefore, in this work, experiments have been designed in order to enhance our understanding of how fluoride is taken up by HAp and how it alters the behavior of HAp surfaces under external influences, such as acid attacks.

Sintered HAp pellets have been used as model systems for the tooth mineral. Fluoridation experiments have shown that the fluoridated layer forming on the HAp surface is only a few nanometers thick and that the layer thickness and the overall amount of fluoride taken up approach a point of saturation on a timescale of about 3 min. Although the layer is very thin and contains only minute amounts of fluoride, a very strong effect on the acid resistance of HAp could be observed: The surface was apparently inert to acid attacks for several minutes.

These results give new insight into the mechanisms and especially into the timescale of fluoride uptake by HAp and they show how the incorporated fluoride in HAp correlates with its protective impact.

Kurzzusammenfassung

Die Anwendung von Fluoriden in Zahnpflegeprodukten ist seit Jahrzehnten fester Bestandteil der Kariesprophylaxe. Nach heutigem Kenntnisstand unterstützen Fluoride die Remineralisierung beschädigten Zahnschmelzes. Sie mindern die Demineralisierung des Schmelzes und sie verringern die Haftkräfte von Bakterien.

Bis heute sind die genauen Mechanismen der Fluoridaufnahme in die mineralische Komponente des Schmelzes, d.h. Hydroxylapatit (HAp), noch nicht vollständig verstanden. In der vorliegenden Arbeit wurden Experimente entwickelt, die zu einem besseren Verständnis der Fluoridaufnahme beitragen, und die zeigen, wie die Fluorierung das Verhalten der HAp-Oberfläche bei einem Säureangriff verändert.

Als Modellsysteme für die mineralische Komponente des Schmelzes wurden gesinterte HAp-Prüfkörper verwendet. Die fluorierte Schicht, die sich an der HAp-Oberfläche bildet, ist nur wenige Nanometer dick. Die Schichtdicke und die Gesamtmenge an Fluorid, die aufgenommen wird, erreichen nach etwa 3 min einen Zustand der Sättigung. Trotz der geringen Dicke und des geringen Fluoridgehalts der Schicht konnte eine starke Auswirkung auf die Säureresistenz von HAp nachgewiesen werden: Die Oberfläche war für einige Minuten immun gegenüber Säureangriffen.

Die Ergebnisse dieser Arbeit liefern neue Erkenntnisse über die Mechanismen und insbesondere über den zeitlichen Verlauf der Fluoridaufnahme in HAp und zeigen die schützenden Auswirkungen aufgenommenen Fluorids auf HAp-Oberflächen.

Contents

1	Introduction	1
2	Overview and Connectivity	3
3	Background and State of the Art	5
3.1	Intermolecular Forces	5
3.1.1	The Coulomb Force	5
3.1.2	Ionic and Covalent Bonds	6
3.1.3	Van der Waals Forces	6
3.1.4	Electric Double Layers and DLVO theory	7
3.2	Acids and Bases	7
3.2.1	The Law of Mass Action and pH Values	7
3.2.2	Buffer Solutions	8
3.2.3	The Solubility Product	9
3.3	Hydroxyapatite and Dental Enamel	10
3.3.1	Atomic and Microscopic Structure of Hydroxyapatite and Dental Enamel	10
3.3.2	Synthesis	12
3.4	Biofilm Formation on Dental Surfaces	12
3.4.1	Bacteria	12
3.4.2	The Acquired Enamel Pellicle	13
3.5	Etching and Solubility of Hydroxyapatite	14
3.6	Fluoridation	15
3.6.1	Fluoride in Caries Prophylaxis	15
3.6.2	Fluoride Uptake in Hydroxyapatite	16
4	Materials and Methods	19
4.1	Hydroxyapatite	19
4.2	Sintering	20
4.3	X-ray Photoelectron Spectroscopy	20
4.4	Atomic Force Microscopy	21
4.5	Electron Microscopy and Electron Backscatter Diffraction	22
4.6	Materials and Instrumentation	22

5	Results and Discussion	25
5.1	Synthesis and Characterization of Hydroxyapatite Substrates	25
5.2	Fluoride Uptake in Hydroxyapatite from Aqueous Solution	27
5.3	The Acid Resistance of Fluoridated Hydroxyapatite	28
5.4	Bacterial Adhesion to Hydroxyapatite Surfaces	29
5.5	Protein Adsorption and Single Molecule Force Spectroscopy	30
5.6	Plasma Polymerization of Bioceramics	31
6	Summary and Outlook	33
6.1	Summary	33
6.2	Outlook	34
	References	37
	Publications:	
	Appendix I: Synthesis of Hydroxyapatite Substrates: Bridging the Gap between Model Surfaces and Enamel	49
	Appendix II: Time Dependence of Fluoride Uptake in Hydroxyapatite	61
	Appendix III: Effect of Fluoride Treatment on the Acid Resistance of Hydroxyapatite	71
	Appendix IV: Enhanced Adhesion of <i>Streptococcus Mutans</i> to Hydroxy- apatite After Exposure to Saliva	81
	Appendix V: Photoactivatable Mussel-Based Underwater Adhesive Proteins by an Expanded Genetic Code	89

List of Abbreviations

- AmF – amine fluoride
- AFM – atomic force microscopy
- BSA – bovine serum albumin
- DOPA – dihydroxyphenylalanin
- EBSD – electron backscatter diffraction
- FAP – fluorapatite
- FAST – field assisted sintering technique
- HAp – hydroxyapatite
- MD simulations – molecular dynamics simulations
- NaAc – sodium acetate
- NaF – sodium fluoride
- PEG – polyethylene glycol
- PLS – pressureless sintered
- RMS – root mean square
- S. carnosus* – *Staphylococcus carnosus*
- S. mutans* – *Streptococcus mutans*
- SEM – scanning electron microscopy
- SPS – spark plasma sintering
- TCP – tricalcium phosphate
- TEM – transmission electron microscopy
- XPS – X-ray photoelectron spectroscopy
- XRD – X-ray diffraction

1 Introduction

The prevalence of dental caries is a concerning health issue. In 2016, caries of permanent teeth was the most widespread disease with a prevalence of 2.44 billion cases worldwide [1]. Therefore, scientists around the world try to understand the mechanisms that lead to the onset and progression of dental caries in order to be able to control them.

The first step to a developing caries lesion is the formation of a microbial biofilm (plaque) on a tooth. As a result of their metabolism, some of the bacteria in such a biofilm produce acids and thereby locally lower the pH. Depending on the pH drop and other ambient factors such as calcium and phosphate concentrations, the mineral component of the enamel, namely hydroxyapatite (HAp), then starts to dissolve which may result in a caries lesion [2].

There are two main areas to be explored to understand the mechanisms of caries development: (i) The process of biofilm formation and (ii) the behavior of the tooth mineral substance upon an acidic attack. Since decades fluoride containing products are used in health care because of their caries prophylactic effect. However, the exact mechanisms of fluoride uptake in HAp and the origin of its protective impact are not conclusively clarified. Therefore, in area (i) as well as in area (ii), the influence of surface modifications by fluoride treatment needs to be evaluated.

Ideally, all experiments would be performed on natural teeth and under the physiological conditions of the oral cavity. However, because of natural variations between individuals and even between teeth from the same individual, the tooth material is not available in a reliable chemical composition. For similar reasons, “the oral cavity” is a rather undefined space for experiments. In order to overcome these obstacles and gain general insights into the fundamental mechanisms of caries development, this work uses well-defined synthetic model tooth material. Choosing this pathway implies that not all results found in model systems will apply directly to the natural systems. Therefore, care must be taken that the “best” model system available is chosen and that the implications and limitations of the results are discussed.

In this thesis, HAp pellet samples have been produced and characterized. The mechanisms of fluoride uptake of HAp from sodium fluoride (NaF) solutions were explored and the behavior of the HAp surface upon an acidic attack before and after surface modification with fluoride was investigated.

The results of this thesis led to new insights into the timescale and the saturation values of the fluoridation mechanism and improved our understanding of the etching behavior of fluoridated HAp surfaces.

2 Overview and Connectivity

This thesis includes five articles that have been published in peer-reviewed scientific journals. The common goal of all of these studies is to extend the current knowledge about the emergence and the prevention of dental caries from a physical and chemical point of view.

The publication by **Zeitz et al. in *ACS Applied Materials & Interfaces* 2016** (Addendum I) describes two different synthesis routes for HAp pellets of very high density and surface quality. Beyond a detailed characterization of the base material, i.e. a commercial HAp powder, and the produced pellets, an example is presented on how these samples can serve as model surfaces in future biophysical studies: It is shown that, due to the high surface quality of the produced HAp samples, it is possible to observe the adsorption of single bovine serum albumin (BSA) proteins onto the HAp surface via AFM. The pressureless sintered samples characterized in this study served as a simplified model system for dental enamel in further three of the five enclosed publications (Addenda II, III, and IV).

The most widely used method of dental caries prophylaxis, i.e., the application of fluoride, is investigated in the publication by **Faidt et al. in *ACS Biomaterials Science & Engineering* 2017** (Addendum II). There, it has been found that the uptake of fluoride in HAp from an aqueous NaF solution is limited by time. After ca. 3 min, a fluoridated layer with a fluoride concentration of around 3 at-% and a thickness, i.e., a mean penetration depth of fluoride ions into the HAp, of around 13 nm is formed. Both these parameters do not increase significantly with extended exposition to the fluoride solution. The main aspect of this study, namely the development of a fluoridated layer on HAp over time, was hitherto unknown.

Especially in consideration of the very low thickness of the fluoridated layer, the question arose if such a layer can even act as an efficient barrier against acid attacks on a HAp surface. The answer to this question has been revealed in the publication by **Faidt et al. in *Langmuir* 2018** (Addendum III). The results of this study show that even minute amounts of fluoride in HAp can render the surface topography immune to acid attacks for several minutes.

Alongside the knowledge about the behavior of HAp in the face of an acid attack, it is also important to fundamentally understand the interactions of HAp with the main source of these acids: bacteria. Therefore, in the publication by **Spengler et al. in *Journal of Molecular Recognition* 2017** (Addendum IV) the adhesion of *Streptococcus mutans* to HAp surfaces was explored before and after the bacterial cell was incubated in saliva. It could be concluded that *S. mutans* is well adapted to the oral environment, as its adhesion force, rupture length and de-adhesion work are significantly increased after the saliva treatment.

Bacteria are most harmful when they conglomerate in a biofilm. On hard tissues in the oral cavity, this biofilm is also called dental plaque. Its development starts with the adsorption of proteins which almost instantaneously form the so-called acquired pellicle, an acellular proteinaceous layer that, among other functions, facilitates bacterial adhesion. Hence, it is desirable to achieve a comprehensive understanding of the adsorption and adhesion of pellicle proteins to HAp. Besides the flow chamber experiments, the results of which are shown in Addendum I, a technique has been introduced in our lab that allows for the functionalization of AFM tips with individual proteins, enabling single molecule force spectroscopy. First results using this method have been published in the publication by **Hauf et al. in *ChemBioChem* 2017** (Addendum V).

In the publication by **Khurana et al. in *European Polymer Journal* 2018** [3] it has been shown that calcium phosphate ceramics can be coated with polymers while maintaining their biocompatible or even bioactive properties. These results can open up new perspectives in the design of dental restorations or implants.

This thesis is sectioned into the following chapters:

- The chapter **Background and State of the Art** introduces the organisms and biological and synthetic materials that are of relevance for this thesis. The current scientific knowledge concerning the production, the fluoridation and the etching behavior of synthetic HAp surfaces is reviewed and a brief overview over biofilm formation and strategies in caries prophylaxis is given.
- In the chapter **Materials and Methods** the methods that were applied in the experiments are briefly described and all materials and instrumentation are listed.
- The chapter **Results and Discussion** highlights the results of this thesis, discussing the findings of the enclosed publications.
- The chapter **Summary and Outlook** summarizes the presented work and turns the focus to future research.

3 Background and State of the Art

3.1 Intermolecular Forces

All matter in our universe is held together by four fundamental forces. The strong and weak interactions act on the subatomic level and are responsible, e.g., for nucleons binding together. The electromagnetic and gravitational interactions are effective on a much larger spatial range. For example, electromagnetic forces act between the protons of atomic nuclei, yet they can also be effective over billions of light years [4], which is the reason why we can observe distant galaxies with astronomical radio telescopes. The following description of interactions that are most relevant for this thesis is textbook knowledge in physics (see, e.g., textbooks by Israelachvili [5] or by Kopitzki and Herzog [6]), yet not necessarily in the life sciences which is the background of a large part of the targeted readership.

3.1.1 The Coulomb Force

The Coulomb force acts between two bodies or particles which carry a charge. Depending on whether the charges have opposite or equal signs, the Coulomb force may be attractive or repulsive, respectively. Mathematically, Coulomb's law is described as

$$F_C = \frac{Q_1 Q_2}{4\pi\epsilon_0\epsilon_r r^2}, \quad (3.1)$$

where Q_1 and Q_2 denote the charges of the two bodies or particles, ϵ_r is the dielectric permittivity of the medium through which the interaction occurs, r is the distance between the two bodies, and ϵ_0 , the vacuum permittivity, is the scaling factor for SI units.

Although the electrostatic interaction between two isolated charges is long-ranged as the inverse square dependence of Coulomb's law suggests, in reality, i.e., in a crystal lattice or in a liquid, there are not only two, but many charges that influence each other. In an overall neutral crystal lattice, every charge is compensated by a countercharge. Thus, all opposing charges screen each other which leads to the total electric field outside of the lattice to decay not according to $1/r^2$, but exponentially with a decay length that is even smaller than the distance between the ions in the lattice [5]. Similarly, a positively charged ion in a liquid will be surrounded by negatively charged ions that screen the positive charge, which also leads to an exponential decay of the electric field of the positive ion.

3.1.2 Ionic and Covalent Bonds

The ionic bond is a direct consequence of the Coulomb force: Positively and negatively charged ions attract each other and the strength of their attraction is stronger the smaller their distance is from each other. Since in an ionic crystal the next neighbors of an ion are always oppositely charged, the attractive forces predominate the repulsive forces and the crystal is bound by the net attraction.

The ionic bond occurs when an atom (usually a metal atom) releases an electron that is then taken up by another atom (usually a non-metal atom), yielding a pair of oppositely charged ions. If, however, both involved atoms tend to keep their electrons, a covalent bond can be formed by a pair of electrons that is shared by two atoms. For example, every H atom has one electron in the 1s orbital surrounding the atomic core. When two of these atoms approach each other, the orbitals can overlap with both electrons then belonging to both H atoms, forming a covalent bond in a hydrogen molecule (H_2). The covalent bond is based on the exchange interaction between electrons which is a quantum mechanical effect and, therefore, cannot be explained by classical physics.

In contrast to ionic bonds, a characteristic feature of covalent bonds is their directionality which means that bonds from one atom to several other atoms can only be established under distinct angles leading to the formation of distinct crystal structures like, e.g., the diamond structure. Covalent bonds can also be formed between elements of different types (e.g., phosphorous and oxygen, forming PO_4^{3-} ions), however, usually such bonds are not purely covalent, but mixtures of covalent and ionic bonds.

3.1.3 Van der Waals Forces

The interactions between permanent dipoles (Keesom interactions), between a permanent and an induced dipole (Debye interactions) and between a fluctuating dipole and an induced dipole (London dispersion interactions) are the three contributors to the van der Waals force. The dispersion forces arise from fluctuations of the electron shells around the atomic cores. Due to the core and the surrounding electrons having opposite charge, these fluctuations lead to changing dipoles that, when two atoms or molecules approach each other, will align and attract each other. Generally, the strength of this attraction exceeds the strength of the Keesom and Debye interactions.

Although the van der Waals interaction between two single particles is short-ranged and its potential follows a power-law dependence of $1/r^6$, where r is the distance between the two particles, this dependence is drastically changed when the geometry of the involved interaction entities is taken into account. For example, the interaction potential between two flat surfaces depends on their distance with $1/r^2$, while the potential between a sphere (or a macromolecule) and a flat surface proceeds according to $1/r$ [7] and can therefore be regarded as long-ranged.

3.1.4 Electric Double Layers and DLVO theory

In liquids, charged surfaces attract oppositely charged ions that may either attach loosely to the surface, building the so-called Stern or Helmholtz layer, or stay in a diffuse layer near the surface. The system of a charged surface and the oppositely charged counter-ions is known as the electric double layer. Like van der Waals forces, the forces between two objects caused by the electric double layer are dependent on the geometry of the interaction entities. However, the electric double layer interaction decays exponentially with the decay constant κ . The characteristic decay length of these interactions is termed the Debye length and is defined as the inverse of κ . The Debye length is about 1 μm in pure water and decreases with increasing ion concentration in a solution. Under physiological conditions, the Debye length typically is around 10 nm [7].

The combined effect of forces arising from electric double layers and van der Waals interactions is described in the DLVO theory, which is named after its developers B. V. Derjaguin and L. Landau [8] and E. J. W. Verwey and J. T. G. Overbeek [9]. For the interaction between two bodies (e.g., a colloidal particle and a flat surface), the DLVO theory features the following main propositions: (i) At small enough distances, the van der Waals forces are dominant due to their power law dependence, leading to the primary minimum in interaction energy at contact. (ii) Due to the electric double layer, there is a repulsive energy barrier whose strength depends on the charge density of the surfaces and the ionic strength (i.e., the Debye length) of the surrounding medium. (iii) Also depending on the ion concentration of the solution, a secondary interaction energy minimum at a separation beyond the energy barrier may occur. Since the secondary minimum is far weaker than the primary minimum, particles that approach the surface and cannot overcome the energy barrier are only weakly bound to the surface [5].

3.2 Acids and Bases

As discussed in Section 3.1, the types and concentrations of ions in a solution can have a significant influence on the interactions occurring between objects in that medium. Therefore, knowledge about the solubility and reaction behavior of materials in liquids is crucial. In the following subsections, the relevant effects are described based on the explanations in the textbook by Mortimer [10].

3.2.1 The Law of Mass Action and pH Values

When two substances interact in a reversible reaction, at a particular time they will reach a state of dynamic chemical equilibrium which means that the forward reaction and the reverse reaction occur at the same speeds. The chemical equation for an equilibrium with two reactants A, B and two products X, Y (with their respective stoichiometric coefficients a , b , x , and y) is



The reaction speeds of the forward (v_f) and the reverse (v_r) reaction can then be expressed as

$$v_f = k_f \cdot c^a(\text{A}) \cdot c^b(\text{B}) \quad (3.3)$$

$$v_r = k_r \cdot c^x(\text{X}) \cdot c^y(\text{Y}), \quad (3.4)$$

where k_f and k_r denote the rate constants of the forward and reverse reactions and c describes the concentration of the respective substance. Since these reaction speeds are equal in equilibrium, equations 3.3 and 3.4 yield

$$\frac{c^x(\text{X}) \cdot c^y(\text{Y})}{c^a(\text{A}) \cdot c^b(\text{B})} = \frac{k_f}{k_r} = K \quad (3.5)$$

which is known as the law of mass action that allows for predictions of concentration ratios in chemical equilibrium. The constant K is termed the equilibrium constant and is temperature dependent.

With the law of mass action applied to the intrinsic dissociation of water and the ion product of water ($K_W = c(\text{H}^+) \cdot c(\text{OH}^-) = 1.0 \times 10^{-14} \text{ mol}^2 \text{ L}^{-2}$), the concentration of H^+ ions $c(\text{H}^+) = 1.0 \times 10^{-7} \text{ mol L}^{-1}$ can be calculated. The pH value is defined as the negative decadic logarithm of the concentration of H^+ ions¹ (in mol L^{-1}) and, therefore, the pH of pure water is 7. Solutions with $\text{pH} = 7$ are called neutral, whereas solutions with lower and higher pH values are called acidic and basic, respectively.

3.2.2 Buffer Solutions

While it is fairly easy to produce a solution of a certain pH by dissolving the needed amount of an acid or base in water, keeping that pH on an extended timescale might pose a problem as even very small amounts of acidic (e.g., CO_2 from air) or basic components can change the pH of the solution. To encounter this problem, buffer solutions (also termed pH buffers or hydrogen ion buffers) are commonly used. A buffer solution contains a weak acid and its conjugate base.

Depending on their dissociation behavior in water, acids are classified as weak or strong. A strong acid dissociates completely, whereas a weak acid dissociates only partially. An acid and a base that belong together to the effect that they can transform into each other by transferring one proton between them are called a conjugate acid-base pair. For example, in a system containing acetic acid ($\text{C}_2\text{H}_4\text{O}_2$) and sodium acetate ($\text{C}_2\text{H}_3\text{NaO}_2$), $\text{C}_2\text{H}_4\text{O}_2$ acts as a proton donator, i.e., as an acid, and $\text{C}_2\text{H}_3\text{O}_2^-$ acts as a proton acceptor, i.e., as a base. The two components form a conjugate acid-base pair since the transfer of one proton turns $\text{C}_2\text{H}_4\text{O}_2$ into $\text{C}_2\text{H}_3\text{O}_2^-$ and vice versa. The Na^+ ions in this system do not play a role in the buffering capability of the solution.

If an acid, i.e., an amount of H^+ ions, is added to a buffer solution, the H^+ ions will react with the basic component in the buffer, whereas if a base is added, the introduced

¹More precisely, the definition is $\text{pH} = -\log_{10} a(\text{H}^+)$, with $a(\text{H}^+)$ being the hydrogen ion activity. However, for reasons of simplicity, this definition is rarely used. Instead, the approximation $-\log_{10} a(\text{H}^+) \approx -\log_{10} c(\text{H}^+)$ is applied.

OH^- ions will react with the acidic component in the buffer. In both cases, the pH of the buffer solution remains (almost) unchanged. However, a pH buffer cannot absorb infinite amounts of added acid or base, but has a finite buffer capacity that is determined by the concentrations of the buffer components and their ratio.

The pH of a buffer solution can be calculated with the so-called Henderson-Hasselbach-equation:

$$\text{pH} = -\log K_a - \log \frac{c(\text{HA})}{c(\text{A}^-)} = \text{p}K_a - \log \frac{c(\text{HA})}{c(\text{A}^-)}, \quad (3.6)$$

where $c(\text{HA})$ and $c(\text{A}^-)$ are the concentrations of the acid and the base, respectively. K_a is the dissociation constant of the acidic component of the buffer that describes how much of an acid dissociates in water.

In this work, two different buffers have been used: sodium acetate (NaAc) buffers and phosphate buffers. NaAc buffers at pH 4.5 have been used to etch the HAp surfaces. At pH 5.5, NaAc buffers were utilized to buffer the NaF solutions in fluoridation experiments. In this case, using buffer solutions allowed for a precise control of both the pH and the fluoride concentration. In protein adsorption experiments, where rather physiological conditions are desirable, phosphate buffers at pH 7 have been used.

3.2.3 The Solubility Product

When a difficultly soluble solid is brought into contact with water, ions will be released from its surface and material will reprecipitate at the solid-water interface. At some point, an equilibrium will be reached where the rates of these two processes are equal. The solution is then called saturated with respect to the solid.

Using calcium fluoride (CaF_2) as an example, application of the law of mass action (equation 3.5) leads to

$$\frac{c(\text{Ca}^{2+}) \cdot c^2(\text{F}^-)}{c(\text{CaF}_2)} = K \quad (3.7)$$

$$c(\text{Ca}^{2+}) \cdot c^2(\text{F}^-) = c(\text{CaF}_2) \cdot K = K_{\text{sp}}. \quad (3.8)$$

K_{sp} is the (temperature dependent) solubility product constant that can be used to calculate the solubility of a substance.²

The solubility behavior of HAp becomes particularly important in the Sections 5.2 and 5.3 (and corresponding Addenda II and III), where dissolution and precipitation processes play major roles during the etching and fluoride uptake experiments.

²In this example: $K_{\text{sp}} = 3.9 \times 10^{-11} \text{ mol}^3 \text{ L}^{-3} \Rightarrow c(\text{CaF}_2) = 2.1 \times 10^{-4} \text{ mol L}^{-1}$, i.e., $2.1 \times 10^{-4} \text{ mol L}^{-1}$ of CaF_2 dissolve in water. [10]

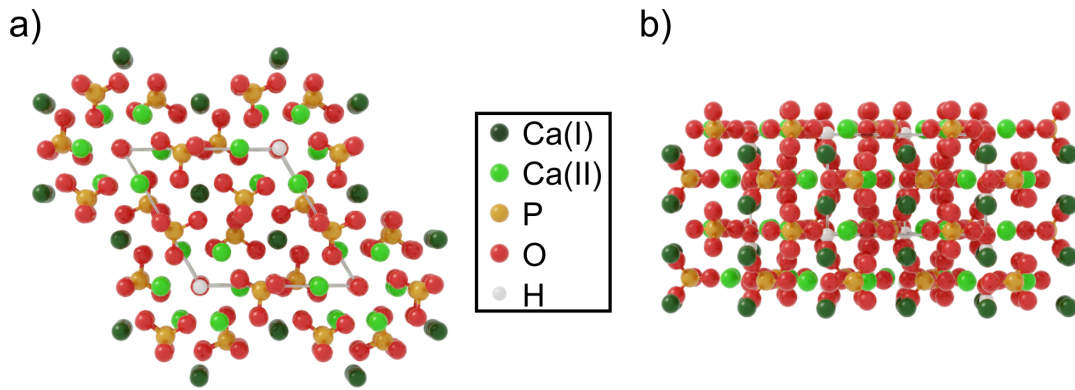


Figure 3.1: Crystal structure of HAp. a) Top view along the crystal's c -axis. Ca(II) atoms are arranged in triangles, forming ion channels that are occupied by OH groups. A unit cell is marked in the center of the structure. b) Side view. Ca(I) atoms form columns parallel to the c -axis. Relative atomic positions are depicted according to Ref. [12]

3.3 Hydroxyapatite and Dental Enamel

3.3.1 Atomic and Microscopic Structure of Hydroxyapatite and Dental Enamel

Hydroxyapatite (HAp) is a calcium phosphate mineral that is part of the hard tissues in mammals. As its name reveals, it is part of the group of apatites, which are calcium phosphate minerals with the chemical formula $\text{Ca}_5(\text{PO}_4)_3\text{X}$, where X stands for the ion giving the apatite its name. This can be, e.g., fluoride (F^-) in fluorapatite (FAp), chloride (Cl^-) in chlorapatite or, in the case of HAp, a hydroxy group (OH^-). Apatites feature a hexagonal crystal structure with lattice parameters of $a = b = 9.635 \text{ \AA}$ and $c = 6.595 \text{ \AA}$ in the case of HAp as calculated by Snyders et al. [11]. According to their position, Ca atoms in the HAp crystal lattice can be classified into two groups, Ca(I) and Ca(II), where the Ca(I) forms columns along the crystal's c -axis (c.f. Figure 3.1). The Ca(II) atoms are arranged in triangles that build ion channels along the c -axis. In HAp, these channels are occupied by hydroxy groups. The PO_4 tetrahedrons are placed around the Ca(II) triangles with the P atoms lying in plane with the Ca(II) atoms [12]. The apatite structure is very forgiving in terms of ionic substitutions. Actually, every ion in an apatite can be substituted while the structure (but not the metrics in terms of lattice parameters) is still maintained [13].

Dental enamel contains about 97% HAp, the rest being water (1.5%) and organic material (1.5%) [14]. However, the biological apatite of dental enamel is calcium deficient and contains around 3.5 wt-% carbonate ions (CO_3^{2-}) [15, 16] that substitute for either the phosphate or the hydroxy groups [17, 18, 19].

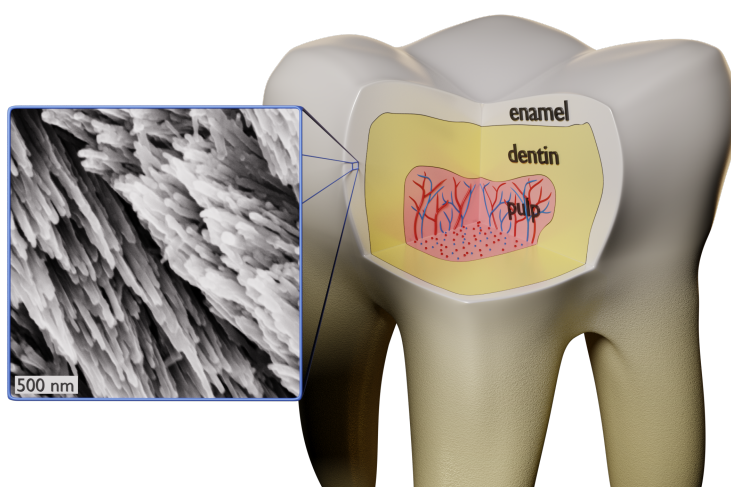


Figure 3.2: Depiction of the general structure of the crown of a tooth consisting of pulp (hosting blood vessels and nerves), dentin, and enamel. The inset shows an SEM image (adapted from [23]) of dental enamel etched in phosphoric acid to uncover the needle-like crystallites.

The microscopic structure of the synthetic HAp samples used in the present work is typical for a body sintered from fine powder. As shown in Addendum I, the samples are polycrystalline with crystallite diameters of around $1\ \mu\text{m}$. Natural dental enamel, in contrast, is a much more complex, hierarchically structured material in which enamel crystallites are parallelly bundled together to form enamel prisms, also called enamel rods. The crystallites are wires of biological apatite (c.f. Fig. 3.2) and are typically around $50\ \text{nm}$ thick and some $10\ \mu\text{m}$, sometimes even more than $100\ \mu\text{m}$, long [14, 20, 21]. The enamel prisms are arranged in a prism pattern and extend from the dentin-enamel junction to the surface of a tooth, forming the so-called prismatic enamel [22]. Between the prisms, there are also enamel crystallites which form the interprismatic enamel. The differences in prismatic and interprismatic enamel lie only in the orientation and the arrangement of the crystallites [22].

During their development and in the course of an individual's whole life, the teeth are subject to numerous external influences, like nutritional habits or dental health care, that cause variations between teeth of different individuals, but also between different teeth of the same individual and even between different sites on one and the same tooth. In terms of standardized samples, these variations in the structure and especially in the stoichiometry of natural enamel make tooth surfaces non-ideal systems for experimental research. Therefore, model systems are desirable that can be synthesized in a more controlled and reproducible way.

3.3.2 Synthesis

There are several ways to synthesize HAp powder. Various methods of precipitation from aqueous solution have been reported [13, 24, 25, 26], but also mechanochemical methods [26] and the acquisition of HAp from natural materials like eggshells [27] are possible. The synthesized HAp grains are typically needle-shaped or spherical with a size of some 10 to some 100 nm [24, 25, 26]. The synthesis of large needle-shaped HAp single crystals with lengths in the mm-range is possible, but requires very high temperatures (200 – 900 °C) and pressures (10 – 400 MPa) [13, 28].

For the production of macroscopic solid HAp bodies, different sintering techniques are available. Hot isostatic pressing [29], microwave sintering [30, 31], field assisted sintering technique (also called spark plasma sintering) [32] or pressureless sintering [33, 34] have all been reported to give similar results, depending on the respective parameters like, e.g., pressure, temperature, or sintering duration.

In our group, HAp specimens have been produced prior to this work by pressureless sintering [35, 36] and via the field assisted sintering technique [36, 37]. In this work, the parameters for processing this material have been optimized in order to get better results in terms of density, stability, and surface quality of the HAp samples.

The attempts to produce a material that mimics the microscopic structure and the mechanical and chemical properties of natural enamel have made great advances in the last decade [38, 39]. In 2005, Chen et al. first reported on synthetic HAp crystallites assembled into an enamel prism-like structure [40]. Recent publications have shown for the first time biomimetic enamel-like materials which match, or may even surpass, the mechanical and chemical properties of natural tooth enamel [41] or which can be produced in cm-range size with well-defined shapes [42].

3.4 Biofilm Formation on Dental Surfaces

The formation of a biofilm on dental hard tissues is the first step in the development of a caries lesion. With hundreds of bacterial species [43, 44], over 1000 different proteins [45] and the complex structure of dental surfaces, the oral cavity constitutes a very complex environment. Therefore, the choice of a model system that allows for the control of intermolecular forces, while resembling the enamel surface as close as possible, is crucial. Besides the choice of suitable buffers, this means that appropriate bacterial species and proteins need to be used according to the respective experiment.

3.4.1 Bacteria

Dental caries, or dental decay, is caused by acids that are produced by bacteria in the course of their metabolism. In 2001, Paster et al. estimated that around 500 different bacterial species populate the human oral cavity [43]. 15 years later, Marsh reported that over 700 bacterial species were found in the human mouth [44]. Fortunately, not all bacteria, but only those which feature distinct characteristics can be held responsible for the progression of dental decay: Cariogenic bacteria need to be able to quickly transport sugars and

convert them to acids. They must survive extreme environmental conditions, such as low pH, and they have to be able to produce extra- and intracellular polysaccharides which serve as an energy storage when no free sugars are available in the oral cavity [44, 46]. Many bacterial species are known to play a role in caries progression, for example *S. mutans* and members of the genera *Lactobacillus*, *Bifidobacterium*, *Propionibacterium*, *Actinomyces* and *Atopobium* [44, 47].

In Addendum IV, we used *S. mutans* and *S. carnosus* bacteria, the former being a species well known for its occurrence in the human mouth and its role in the emergence of caries while the latter is usually not found in the oral cavity and was therefore suspected to behave differently when exposed to oral ambient conditions.

3.4.2 The Acquired Enamel Pellicle

Before the first bacterial cells attach, an acellular proteinaceous layer forms almost immediately on a freshly cleaned or erupted tooth surface [48, 49]. This layer of proteins, termed the acquired enamel pellicle, is initially, i.e., after 2 – 3 min, 10 – 20 nm thick [49, 50, 51] and grows further until reaching a final thickness of 100 – 1000 nm within 60 min [49, 50, 51, 52]. The formation of the acquired enamel pellicle has been found to be a highly selective process [49, 53]. In the initial 3 min aged pellicle, a total of 190 proteins have been identified, of which 72 play a major role in the pellicle composition, including, e.g., lysozyme, serum albumin and α -amylase [54]. In contrast, more than 1050 proteins in whole saliva have been catalogued [45].

The acquired enamel pellicle has several functions: It lubricates the tooth surfaces and, thereby, reduces enamel abrasion [49, 55]. It acts as a semi-permeable barrier, controlling the transport of ions, such as calcium and phosphate ions, and acids [49, 56]. Notably, the uptake of fluoride by dental enamel is not altered in the presence of pellicle or plaque [49, 57]. And it modulates the interactions between the tooth surface and bacterial cells [49, 58]. Depending on the species, the adsorption rates of bacteria on saliva-treated HAp may be increased (e.g., *S. mutans*, *S. salivarius*, *A. naeslundii*) or decreased (e.g., *S. sanguis*, *S. mitis*, *A. viscosus*) because of an altered number of adsorption sites provided by the surface [58, 59].

In experiments, a commonly used method to investigate the acquired enamel pellicle is to carry specimens of enamel, HAp or another substrate of interest attached to splints in the mouth. After the desired maturation period, the splints can be easily removed from the oral cavity to examine the pellicle with various measuring techniques depending on the specific issue, e.g., thickness [49, 50, 51], topography [49, 50, 58], or proteome [49, 53, 54, 58]. Another possibility is to extraorally cover the specimen's surface with saliva or protein solutions to simulate the pellicle development in a less complex environment [57, 60].

In this work, fundamental interactions between single proteins and substrates have been investigated to enhance our understanding of the very first step of pellicle formation: the arrival and attachment of the first proteins. Therefore, AFM fluid cell experiments (Addendum I) as well as AFM based single molecule force spectroscopy have been utilized (Addendum V).

3.5 Etching and Solubility of Hydroxyapatite

Bacteria in the dental biofilm lower the pH in their vicinity by producing acids in the course of their metabolism. This change in pH can lead to the dissolution of the tooth mineral substance and therefore it is important to understand the solubility behavior of HAp in the face of an acidic attack.

The etching of HAp is highly anisotropic. Parallel to the crystal's *c*-axis, the mineral dissolves quickly upon an acidic attack, whereas the etching rates perpendicular to the *c*-axis were found to be negligible [61]. On synthesized single crystals, the formation of hexagonal etch pits on the HAp surface has been observed: The symmetry of these pits depends on the crystal face they are forming on and is therefore determined by the underlying crystal structure [61, 62].

In addition to the crystal structure, the dissolution rates of HAp are also affected by its degree of crystallinity and the amount and types of ionic substitutions in the crystal lattice. Generally, a higher crystallinity of HAp leads to a lower solubility [63, 64]. In the case of ionic substitutions, the change in solubility depends on the ion that is incorporated into the crystal lattice [13]. For example, carbonate ions have been shown to increase the solubility [64], whereas the incorporation of fluoride leads to a strong decrease in solubility [17, 65, 66, 67].

The dissolution behavior of HAp is also depending on the agent exerting the acidic attack. The dissolution of HAp is often reported to start at a pH of 5.5 and below, whereas this demineralization-threshold is at pH 4.6 for FAp [68]. It is, however, important to note that these values are not constants as they depend on the concentrations of, e.g., calcium and phosphate in the surrounding medium [69]. That is, the rates of dissolution depend on the degree of saturation with respect to HAp and on the pH of the acidic agent. The lower the degree of saturation and the lower the pH of an acidic solution, the faster dissolution will progress [70]. Ultimately, it has been shown that the dissolution rates caused by organic acids like acetic or lactic acid are at least one order of magnitude higher than the rates observed upon dissolution in an inorganic acid, e.g., phosphoric acid, when compared at the same pH and degree of saturation [70].

Numerous studies have reported the protective effects of fluoride treatment on HAp [71, 72, 73], carbonated HAp [65] and dental enamel specimens [74, 75, 76, 77]. In dental research, a distinction is made between loosely bound and tightly bound, or tooth-bound, fluoride. The term "loosely bound fluoride" refers to fluoride ions that are adsorbed on the HAp or enamel surface and are therefore only weakly bound. This type of fluoride was for a long time presumed to be "mainly responsible for caries prevention in enamel as far as mineral loss is concerned" [77]. However, later it has been shown that tooth-bound fluoride also has a significant impact on the resistance of enamel against the formation of caries lesions [74] and that the solubility behavior of fluoridated apatite is independent of the fluoride ions' origin in terms of whether it is located in the solid or in the surrounding medium [65].

The extent of the protective effect of fluoride treatment is dependent on the fluoride compound. Significant differences in efficacy have been reported between stannous fluoride

(SnF_2), sodium fluoride (NaF), and amine fluoride (AmF) [75], with SnF_2 causing the largest decrease in solubility [72, 75]. The protective effect of fluoride treatment can be further increased when fluoride compounds are applied in combination with phosphates [73] which may shift the demineralization threshold by providing additional phosphate ions.

While there are many studies that use powder or compacted powder samples to determine the solubility of HAp [16, 63, 64, 70, 72], data on the etching behavior of sintered polycrystalline HAp surfaces is rather scarce. To close this gap and in order to explore the efficacy of ultra-thin fluoridated layers, the etching behavior of pristine and NaF -fluoridated HAp has been investigated in Addendum III, in terms of material ablation due to the acid attack.

3.6 Fluoridation

3.6.1 Fluoride in Caries Prophylaxis

Topical application of fluoride-containing agents is an integral part of dental healthcare since decades. In 1942, Dean et al. found in a controversial study that there is “a general inverse correlation between the fluoride concentrations of the public water supplies ... and the amount of dental caries” [78]. Since then, many studies have shown further evidence that fluoride treatment can prevent dental caries and enamel erosion [74, 76, 79, 80].

The cariostatic effect of fluoride treatment is based on three mechanisms:

- (i) Together with solute calcium and phosphate ions, fluoride ions form FAp that precipitates on the HAp surface and thereby support the remineralization of dental enamel [81, 82].
- (ii) Fluoride inhibits enamel demineralization due to the increased demineralization-threshold of fluoridated HAp [81, 82]. The presence of fluoride ions can also hinder the production of acids by inhibiting enolase [83], an enzyme that plays an important role in the production of phosphoenolpyruvate. Phosphoenolpyruvate is used by oral bacteria to transport mono- and disaccharides through their cell membrane [84], stimulating the production of acidic metabolic products.
- (iii) Fluoridation of HAp decreases the adhesion forces of bacteria to the HAp surface. Loskill et al. have shown that the adhesion forces of three different bacterial species to a fluoride treated HAp surface were 50% weaker than to a pristine HAp surface [37].

There are numerous different fluoride-containing dental healthcare products on the market, ranging from standard over-the-counter products like mouthwashes (ca. 200 – 500 ppm F^-) and toothpastes (1000 – 1500 ppm F^-) to professional products such as fluoride gels (4000 – 6000 ppm F^-) and varnishes (> 22000 ppm F^-) [84]. To add fluoride to these products, manufacturers can resort to a wide range of compounds, e.g., sodium fluoride, stannous fluoride, sodium monofluorophosphate ($\text{Na}_2\text{PO}_3\text{F}$) or amine fluorides like Olafur and Dectafur. Apart from the fluoride concentration and compound, the cariostatic efficacy is also dependent on the application time, the delivery method and the

ability of the fluoride agent to actually reach an exposed apatite surface [84]. While the fluoride uptake in HAp is known to be dependent on pH (see Section 3.6.2), data on the impact of pH on the efficacy of health care products is sparse and studies investigating acidulated [85] or alkaline [86] dentifrices could not show significantly altered efficacies compared to regular neutral dentifrices.

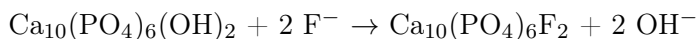
Some countries, e.g., USA, Brazil, Great Britain and Australia, provide fluoride to their population via artificially fluoridating the public water supply [87, 88]. Other countries, including Germany, refrain from this approach because of ethical and legal concerns (compulsory mass medication) and possible health risks like skeletal [89] and dental fluorosis [84] or adverse effects on the neurodevelopment in children [90, 91]. Instead, for infants, the German Federal Institute for Risk Assessment, BfR, recommends the intake of fluoride supplements depending on the age of the child, the nutritional habits (e.g., use of fluoridated table salt), and the fluoride content in the local public water supply [92] to ensure a controlled influx of fluoride.

3.6.2 Fluoride Uptake in Hydroxyapatite

When a HAp surface is exposed to a fluoride containing solution, there are three conceivable mechanisms of fluoride uptake: (i) surface adsorption, (ii) incorporation into the crystal lattice, and (iii) dissolution of HAp followed by precipitation of a fluoridated phase [93].

During surface adsorption, fluoride ions can bind to reactive sites on the HAp surface, e.g., CaOH sites, which may lead to an exchange of water or hydroxide ions with the surrounding medium [93, 94].

The incorporation of fluoride ions into the crystal lattice is possible via a substitution of hydroxy groups [95], leading to the formation of FAp:



As molecular dynamics (MD) simulations have shown, thin films of fluoridated, i.e., partially transformed HAp easily form on a HAp surface [96, 97] with a mixed phase of 50 % HAp and 50 % FAp being the most stable phase [97]. This fluoridation behavior has been confirmed in Addendum II and has also been reported in several other experimental studies [35, 76, 93, 98, 99, 100], albeit often in conjunction with the formation of additional phases forming on the HAp surface through precipitation [35, 76, 100].

Precipitation of HAp or FAp takes place when the ambient medium is supersaturated with respect to the respective mineral. As HAp dissolves, the calcium and phosphate concentrations in the medium near the HAp surface increase, enabling fluoride ions in the surrounding to form FAp or calcium fluoride (CaF_2) that precipitates on the HAp surface. Since this mechanism relies on dissolution, it is strongly pH dependent. At a low pH of 4.0, the formation of CaF_2 [98, 99] or a “ CaF_2 -like material” [101] has been observed. This CaF_2 -like material precipitates in globular particles on the HAp surface and also contains phosphorous and oxygen which affect the solubility and, thereby, control the fluoride release rate [101]. In this way, a CaF_2 -like layer can act as a fluoride reservoir [100]. Overall, in the acidic regime, fluoride treatment of HAp leads to the formation of a

three layer structure containing FAp reaching into the bulk, $\text{Ca}(\text{OH})_2$, and a CaF_2 layer on top [35, 100].

At low pH values, the fluoride uptake capacity is higher than in the almost neutral or alkaline range [35, 93] where the incorporation of fluoride ions into the crystal lattice seems to be the predominant mechanism [35]. While after the fluoridation in the near neutral regime the concentration of fluoride decreases exponentially from the surface into the bulk material [35], a significantly different depth distribution has been found after the fluoridation in the alkaline range, where a subsurface accumulation of fluoride at a depth of about 6 – 7 nm has been measured [37]. A possible explanation for this observation is that alkaline solutions can lead to the desorption of fluoride ions from the HAp surface [102]. That way, the fluoride ions directly at the surface may be depleted while the fluoride in the subsurface remains unaffected.

The thickness of the fluoridated layer that forms on a HAp surface is in the range of a few nm [35, 93, 103]. Some studies performed on natural enamel, synthetic powder, or compacted synthetic powder reported significantly higher layer thicknesses of some 100 nm [104] or even in the μm -range [100, 105]. However, in the rather porous samples used in these studies, diffusion of the fluoride solution into the pores must be considered. Since sodium ions do not get incorporated into the HAp lattice [99], the simultaneous detection of sodium and fluoride in large depths below the HAp surface [104] indicates that the diffusion length of the NaF-solution is measured rather than the actually targeted thickness of the fluoridated layer on the enamel crystallites or powder grains [35].

In this work, the time dependence of fluoride uptake in HAp from a NaF-solution has been determined – an aspect that apparently has not been explored before in detail. In Addendum II, the previously reported nm-thickness of fluoridated layers on HAp [35] has been confirmed and the progress of fluoride uptake in terms of timescale and saturation could be described.

4 Materials and Methods

In this chapter, the used materials and techniques are briefly described. For more detailed information on the presented experimental techniques the reader is referred to the corresponding textbooks. Section 4.6 provides a comprehensive list of materials and instrumentation used in the experiments.

4.1 Hydroxyapatite

Because of the need for chemically and topographically well reproducible surfaces, a procedure was developed to prepare hydroxyapatite pellet samples. The preparation and the characteristics of these samples are described in detail in Addendum I.

As base material, commercially available HAp powder with a mean particle diameter of about 70 nm was used. In order to remove water soluble impurities such as sodium or chlorine, the powder was dispersed in demineralized water and then filtered in a vacuum filtration setup. Subsequently, the wet powder was dried in a drying cabinet and then finely ground in a mortar.

For the production of sintered HAp pellets, two different synthesis routes have been applied: field assisted sintering technology (FAST) and pressureless sintering (PLS). In the FAST method, the powder was compressed with a uniaxial force while being heated to a temperature of 1000 °C. The resulting pellets featured a density of around 3.0 g cm^{-3} , or 95 % relative density when compared to a perfect HAp single crystal with a density of 3.156 g cm^{-3} [33]. In the case of pressureless sintering, the HAp powder was compacted with a uniaxially applied pressure of 100 MPa before sintering the so called green body at a maximum temperature of 1250 °C following a temperature profile suggested by Prokopiev and Sevostianov [34]. More information on sintering processes in general is given in Section 4.2.

In order to achieve flat and smooth HAp surfaces, a grinding and polishing process based on the approach introduced by Zeitz [36] was applied: The samples were ground with silicon carbide (SiC) abrasive paper of decreasing grain sizes (P600 – P4000, FEPA standard) and then polished with diamond solutions of 3 μm and $< 30 \text{ nm}$ particle size. After every grinding and polishing step, the samples were cleaned in an ultrasonic bath in pure water for 5 min. After the last polishing step, the surface was etched for 10 s in a NaAc buffer solution (10 mmol L^{-1} , pH 4.5) followed by another 5 min ultrasonic water bath to remove remaining diamond nano-particles.

4.2 Sintering

Sintering is a thermal processing technique that aims for the stabilization and densification of a compacted body (the so-called green body) of metal or ceramic powders. The driving force in a sintering process is the minimization of the surface and interface energy of a body. Usually, high temperatures are needed to enable material transport in the body. The process itself can be described in three phases: In the initial stage, the particles start to link by forming necks, i.e., the contact points of powder particles transform to contact areas. This leads to an increased stability of the body and to a slight decrease of its volume. In the intermediate stage of the sintering process, the necks grow to form grain boundaries and the grains begin to grow. In this phase, most of the shrinkage of the body takes place. In the final stage of the process, the previously open porosity is converted into a closed porosity by material transport along the grain edges. The grains continue to grow and the number of pores decreases while the remaining pores grow, e.g., through the coalescence of many smaller pores into fewer bigger pores. More detailed and comprehensive information about the processes that occur during sintering can be found, e.g., in the textbooks of Salmang and Scholze [106] or Kang [107].

In Addendum I, two different sintering techniques were applied: the field assisted sintering technique (FAST), also known as spark plasma sintering (SPS) (see, e.g., Ref. [108] for details), and pressureless sintering (PLS) of pre-compacted green bodies in a conventional high-temperature oven. In FAST, the sample is sintered by applying pressure while simultaneously heating it using a pulsed current either through the sample itself in the case of a conductive powder or through a conductive press tool, if the sample is insulating. While both techniques provided similar results, all subsequent experiments were done on PLS samples because of the less sophisticated sintering procedure.

4.3 X-ray Photoelectron Spectroscopy

X-ray photoelectron spectroscopy (XPS) was used to determine the chemical composition of HAp surfaces. Its measuring principle is based on the photoelectric effect that was discovered by Hertz and Hallwachs in 1887 [109, 110], who observed that electrons can be released from a material that is irradiated with light. The theoretical description of this discovery was delivered by Einstein in 1905 [111]. He discerned that light can be interpreted as particles with the energy $E = h\nu$, where h denotes the Planck constant and ν the frequency. Consequently, it is possible to describe the kinetic energy of the released electrons as $E_{\text{kin}} = h\nu - E_{\text{B}} - \Phi$, with E_{B} being the binding energy of a released electron and Φ the work function, a material constant, describing the energy that is needed to remove the electron from the solid. Since the binding energies of core electrons are unique for every element, a measurement of the kinetic energy of released electrons at a known light frequency can be used to identify the types and ratios of atoms present in a sample. X-rays are used in this technique because of their high energy which is needed to release core electrons.

XPS is a very surface sensitive method. While the escape depth, i.e., the mean free path in a material, of electrons ultimately depends on the investigated material, the probing depth in XPS typically lies in the order of only a few Å [112, 113]. In combination with an accurate surface ablation technique such as argon ion etching, XPS becomes a very powerful tool to precisely characterize the chemical composition of thin surface layers.

4.4 Atomic Force Microscopy

The atomic force microscope (AFM) was developed in the 1980s by Binnig, Quate, and Gerber [114] who aimed to overcome the limitation of the conductivity of samples which is necessary for scanning tunneling microscopy (STM) measurements. The probe of an AFM is a microscopic tip underneath a cantilever. When scanning the tip over a surface, the cantilever is displaced due to interactions between the tip and the surface. Under most conditions, this displacement is a direct measure for the surface topography. Modern AFMs are able to resolve height differences in the sub-nm range. The lateral resolution is determined by the geometry of the probe and is typically in the range of a few nm. Further information about the setup and the operating principle of AFMs can be found in appropriate textbooks [115, 116, 117, 118].

Beyond the benefit that non-conductive samples can be imaged – under certain conditions even with atomic resolution [119] – the AFM features several further advantages, one of the most important certainly being its ability to measure surfaces in liquids, which is particularly helpful with biological samples and measurements under physiological conditions. With modern modes of operation, the AFM is furthermore not limited to imaging topography but can also map, e.g., adhesion forces at or Young's moduli of surfaces.

To achieve such enhanced functionality, the AFM is used as a force spectrometer to determine the interaction between the AFM tip and the probed surface in detail. The experimentalist is, however, not limited to using the typically employed silicon or silicon nitride tips, but he/she can also functionalize tips with single molecules, e.g., proteins [120, 121], or use tipless cantilevers with larger structures like beads or even living cells attached as a probe [122, 123, 124].

In this work, AFM was used with various purposes: In Addendum I, it was used to characterize the topography and the roughness of HAp surfaces and to image protein adsorption in a micro volume fluid cell. In Addendum III, the ablation of HAp material due to an acid attack has been measured with AFM. Since AFM does not provide absolute height values, but only relative height differences between regions in one scan area, an experimental design had to be developed for these experiments that enabled an absolute height reference. In Addenda IV and V, the AFM has been used as a force spectrometer to determine adhesion forces of bacteria and proteins.

4.5 Electron Microscopy and Electron Backscatter Diffraction

In scanning electron microscopy (SEM), a beam of electrons with high energy (0.1–30 keV) is used as a probe to image a surface. Due to their shorter wavelengths, the use of high-energy electrons enables higher resolutions compared to classical light microscopy. However, this benefit comes at the prize of higher demands on the sample and the measurement setup: Since the electrons must not be scattered by atmospheric atoms on their way to or from the sample, the SEM needs to be operated under high vacuum conditions ($< 10^{-4}$ Pa). Furthermore, charging of the sample would deflect electrons and hence prevent a clear image of the surface. Therefore, samples for SEM need to be conductive or must be prepared by evaporating a thin conductive layer (e.g., carbon, gold, or platinum) on their surface.

In SEM, two kinds of electrons can be detected: secondary electrons that are emitted from the surface, and backscattered electrons from the primary electron beam which are reflected after multiple scattering events in the sample's surface. An analysis of the spatial distribution of these backscattered electrons, the so-called Kikuchi pattern, yields information about the crystal structure and the crystallite orientation of the probed material.

This technique, called electron backscatter diffraction (EBSD), has been used, e.g., in Addendum I to characterize the grain sizes and orientations of HAp crystallites and to relate the grain orientations to etching rates. In order to correlate an AFM scan with an EBSD image, a strategy had to be developed that allowed both techniques to measure the very same area. Therefore, the HAp surface was mapped with AFM and a coordinate system based on prominent surface features (e.g., cracks or holes) was established. With the help of these coordinates it was possible to rediscover locations from the AFM measurement with SEM and then perform the EBSD scan.

4.6 Materials and Instrumentation

Chemicals and other consumables:

- Acetic acid (100 %, CAS: 64-19-7), VWR International GmbH, Darmstadt, Germany
- Acetone (99.98 %, CAS: 67-64-1), Fisher Scientific GmbH, Schwerte, Germany
- AFM tips: FastScan-A, FastScan-C, FastScan-D, and MLCT, Bruker AFM Probes, Camarillo, CA, USA
- AFM tips: OMCL-AC160TS, Olympus Europa SE & Co. KG, Hamburg, Germany
- Citric acid (99 %, CAS: 77-92-9), Sigma-Aldrich Chemie GmbH (SKU: C0759), Munich, Germany
- Diamond solution: DiaPro DAC 3 μ m, Struers GmbH (SKU: 40600371), Willich, Germany

- Diamond solution: Liquid diamond MSY 0-0.03 GAF, Microdiamant AG, Lengwil, Switzerland
- Dimethyl sulfoxide ($\geq 99.9\%$, CAS: 67-68-5), Sigma-Aldrich Chemie GmbH (SKU: 472301), Munich, Germany
- Ethanol (99.9%, CAS: 64-17-5), VWR International GmbH, Darmstadt, Germany
- Ethanolamine hydrochloride ($\geq 99\%$, CAS: 2002-24-6), Sigma-Aldrich Chemie GmbH (SKU: E6133), Munich, Germany
- Grinding papers: Silicon carbide, 250 mm dia., FEPA-standard: P600, P1200, P2500, and P4000, ATM GmbH, Mammelzen, Germany
- Hydroxyapatite nanopowder ($\geq 97\%$, CAS: 12167-74-7), Sigma-Aldrich Chemie GmbH (SKU: 677418), Munich, Germany
- Molecular sieves, 4 Å (CAS: 70955-01-0), Sigma-Aldrich Chemie GmbH (SKU: 208604), Munich, Germany
- Polishing cloth: DP-Dac, 250 mm dia., Struers (SKU: 40500213), Willich, Germany
- Sodium cyanoborohydride (95%, CAS: 25895-60-7), Sigma-Aldrich Chemie GmbH (SKU: 156159), Munich, Germany
- Sodium hydroxide (99%, CAS: 1310-73-2), Grüssing GmbH, Filsum, Germany
- Sodium phosphate dibasic dihydrate ($\geq 99.5\%$, CAS: 10028-24-7), E. Merck, Darmstadt, Germany
- Sodium phosphate monobasic ($\geq 99\%$, CAS: 7558-80-7), Fluka Chemie AG, Buchs, Switzerland
- Sodium acetate trihydrate (CAS: 6131-90-4), Merck KGaA (SKU: 106271), Darmstadt, Germany
- Triethylamine ($\geq 99.5\%$, CAS: 121-44-8), Sigma-Aldrich Chemie GmbH (SKU: 471283), Munich, Germany

Instruments and measurement devices:

- AFM: FastScan Bio with controller NanoScope V, Bruker Nano Surfaces, Santa Barbara, CA, USA
- AFM: BioScope Catalyst with controller NanoScope V, Bruker Nano Surfaces, Santa Barbara, CA, USA
- Drying cabinet: FED 53, Binder GmbH, Tuttlingen, Germany
- EBSD detector: Digiview 3, EDAX Inc., Mahwah, NJ, USA

- pH meter: SevenExcellence with perfectION electrode for fluoride concentration measurement, Mettler Toledo, Gießen, Germany
- Photoelectron Spectrometer: ESCALAB Mk II, Vacuum Generators (today: VAC-GEN Ltd.), Hailsham, UK
- Polishing machine: SAPHIR 520 with dosing unit TOPAS 130, ATM GmbH, Mammelzen, Germany
- Press/compactor: MP5MD, Maassen GmbH, Reutlingen, Germany
- SEM: JSM-7000 F, JEOL Ltd., Tokyo, Japan
- Sintering furnace: LM-312.27, Linn High Therm GmbH, Eschenfelden, Germany
- TEM: JEM 2011, JEOL Ltd., Tokyo, Japan
- Water purifier: GenPure, Thermo Fisher Scientific Inc., Waltham, MA, USA
- XRD: X'Pert Pro diffractometer with PIXcel 1D detector, PANalytical, Almelo, Netherlands

5 Results and Discussion

The protective effect of fluoride treatment of tooth surfaces has been confirmed in numerous studies as discussed already in Section 3.5. The exact uptake mechanisms of fluoride into HAp are, however, still not completely understood and the values that have been found experimentally for the thickness of a fluoridated layer forming on HAp or enamel range from a few nm [35, 36, 37, 93, 103] to the μm range [100, 105]. While a thickness of a few nm has been confirmed by measurements in our group [35, 36, 37], the measurement of much larger values is most likely due to a higher porosity of the investigated solid, i.e., rather the diffusion of the agent into the HAp surface via micro cavities than the fluoridation of the HAp surface itself was probed (c.f. Section 3.6.2). Therefore, in order to find a reliable penetration depth of fluoride ions into HAp, dense and smooth surfaces with a porosity as low as possible are needed to represent a single enamel crystal on a macroscopic scale.

5.1 Synthesis and Characterization of Hydroxyapatite Substrates

Two feasible synthesis routes for such specimens are presented in the publication by **Zeitz et al. in *ACS Applied Materials & Interfaces* 2016** (Addendum I). The base material, i.e., the HAp powder, has been characterized by X-ray diffraction (XRD) which confirmed the HAp crystal structure and showed only minor structural impurities, probably caused by incorporated calcite (CaCO_3) or quicklime (CaO). Transmission electron microscopy (TEM) images of the powder have revealed the spherical geometry of the particles with a diameter of about 71 nm, which is in accordance with the value of 74 nm obtained from the analysis of XRD data. The chemical composition of the base material has been determined by XPS: A slight calcium deficiency has been detected as well as an excess in oxygen and carbon which can be explained by the presence of adsorbates that are readily detected by XPS due to the technique's high surface sensitivity.

Solid, compact HAp specimens have been produced by using the field assisted sintering technique (FAST) and pressureless sintering (PLS) after uniaxial compression. AFM and EBSD measurements have revealed mean grain sizes of about 0.6 μm in the FAST samples and 1.1 μm in the PLS samples. The EBSD experiments furthermore have shown that there is no preferred crystallite orientation. By matching an EBSD scan to a previously recorded AFM image of an etched HAp surface, the preferred etching of HAp along the crystal's c -axis, i.e., the (0001) direction, could be confirmed (see Fig. 5.1, and Fig. 6 in Addendum I). XPS measurements have revealed a decreased oxygen content in both FAST and PLS samples when compared to the stoichiometry of the base material which

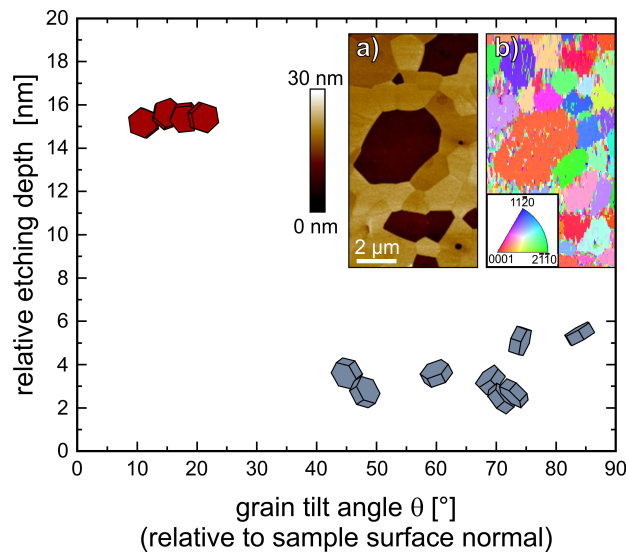


Figure 5.1: Relative etching depths in dependence of the crystal structure tilt angle with respect to the surface normal of the sample. The symbols in the graph depict the orientation of the HAp unit cell in the corresponding crystallite. Inset a) shows the AFM scan used to determine the height values. Inset b) shows an EBSD scan at the same position that was used to determine the tilt angles.

is in part due to a preferred release of OH^- ions during a wet chemical etching step performed in the course of the surface cleaning procedure. A second reason for the loss of oxygen is most likely the removal of intrinsic water during the sintering process. An XRD analysis of the FAST and PLS samples has shown that the material has not undergone any changes in terms of its crystal structure. In comparison with the data of the base material, strongly decreased peak widths have been observed in the XRD patterns of FAST and PLS samples which is due to the greatly increased grain size. Vickers hardness tests¹ have revealed no significant differences between FAST and PLS samples. However, when compared to natural tooth enamel, the synthetic HAp bodies are considerably harder than samples from human or bovine teeth because of their solid nature without the softer organic matrix found in enamel.

The comprehensive characterization of the HAp specimens presented in this study laid the foundation for the further use of these specimens in the work described in the following sections.

¹Hardness tests were performed in cooperation with C. Gachot, Department of Functional Materials, Saarland University.

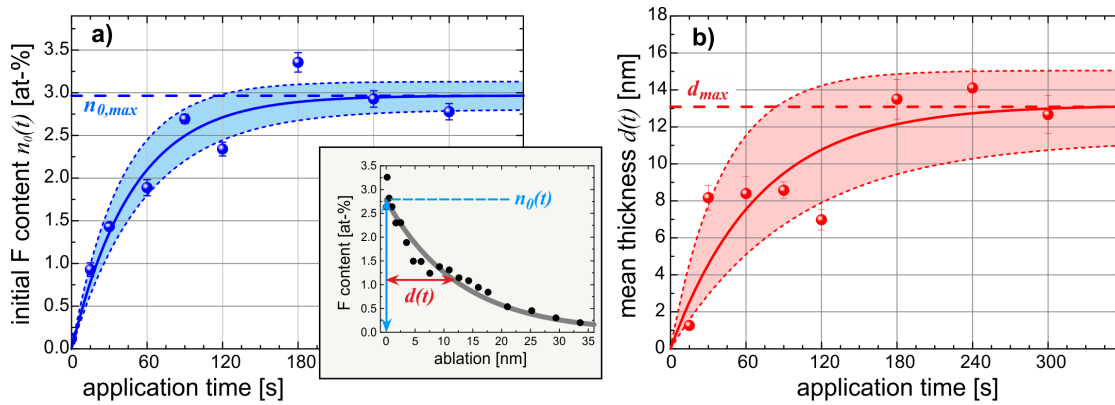


Figure 5.2: Temporal progress of fluoride uptake in HAp. a) Fluoride content at the HAp surface. b) Mean thickness of the fluoridated layer. The inset shows a typical fluoride depth profile after an application time of 5 min and illustrates the meaning of the parameters $n_0(t)$ (as used in a) and $d(t)$ (as used in b).

5.2 Fluoride Uptake in Hydroxyapatite from Aqueous Solution

Fluoridation experiments have been performed on PLS samples using a NaF-solution (500 ppm NaF, 37 °C, pH 5.5). With alternating XPS measurements and argon ion etching, element specific depth profiles have been recorded to determine the amount of fluoride taken up by the HAp surface in dependence on the depth below the initial surface and the application time of the fluoride agent. The results of these experiments are published in the article by **Faidt et al. in *ACS Biomaterials Science & Engineering* 2017** (Addendum II). It has been shown that, after the application of the NaF-solution, the fluoride concentration decreases exponentially from the surface into the bulk of the material (c.f. inset in Fig. 5.2). The application time of the fluoride agent has been varied between 0 s and 300 s in order to find whether there are any limits of the fluoride uptake and to determine the timescale on which the fluoride is incorporated. For application times between 0 s and 180 s both the amount of fluoride directly at the surface and the mean thickness of the fluoridated layer increases with increasing application time. As Figure 5.2 shows, both these parameters slowly change to saturation at about 180 s, indicating that no further fluoride is taken up by the surface or that the rates of fluoride uptake and fluoride release are equal.

The amount of fluoride at the surface, n_0 , and the thickness of the fluoridated layer, d , have been found to grow exponentially with the application time according to

$$n_0(t) = n_{0,\max} \cdot (1 - \exp(-t/\tau_n)), \quad (5.1)$$

$$d(t) = d_{\max} \cdot (1 - \exp(-t/\tau_d)), \quad (5.2)$$

respectively. There, $n_{0,\max}$ and d_{\max} are the maximum values that n_0 and d can reach, and τ_n and τ_d are the corresponding growth constants. With the fluoridation parameters

applied in this study (i.e., F^- concentration, temperature, and pH), the maximum amount of fluoride at the surface has been determined as $n_{0,\max} = 2.97 \pm 0.16$ at-%, which means that, in the case of a pure $OH^- - F^-$ substitution, 62% of the OH^- ions are substituted by F^- ions. Considering the possible formation of other phases such as CaF_2 due to the fluoridation in the acidic milieu, this result is in good accordance with molecular dynamics (MD) simulations by de Leeuw [97] who has reported a 50% HAp/50% FAp mixed phase to be energetically favorable.

The maximum mean thickness of the fluoridated layer in this study has been found to be $d_{\max} = 13.2 \pm 1.9$ nm, a value that clearly exceeds the sub-nm range predicted by the MD simulations of de Leeuw in Ref. [97]. However, considering the polycrystalline nature of the synthetic samples, deviations from the theoretically predicted value that was determined on a pure (0001) single crystal are not surprising.

As reported in Addendum III, presumably only a small fraction of the accepted fluoride is tightly bound, i.e., incorporated into the crystal lattice. The major part of the fluoridated layer seems to be only loosely bound and can be removed, e.g., by the application of ultrasound.

5.3 The Acid Resistance of Fluoridated Hydroxyapatite

Considering the low values of the amount of fluoride taken up by HAp and especially the thickness of the fluoridated layer that have been reported in Addendum II, the anti-erosive effect of such an ultra-thin protective layer needed to be tested. Therefore, etching experiments have been carried out, the results of which are reported in the article by **Faidt et al. in *Langmuir* 2018** (Addendum III).

As a reference, the etching rates of a pH 4.5 NaAc buffer on a non-fluoridated HAp surface have been determined via AFM measurements. The height distributions in the AFM micrographs after etching (see Figs. 5.3a and b) allow for the evaluation of two different etching rates, one for areas that are ablated quickly upon the acidic attack, $r_{\text{HAp,fast}} = 0.038 \pm 0.002 \text{ nm s}^{-1}$, and another for more slowly etched areas, $r_{\text{HAp,slow}} = 0.191 \pm 0.005 \text{ nm s}^{-1}$. The different rates are attributable to the anisotropic etching behavior of HAp crystals. Since the HAp surface consists of not only two, but many crystallites with different orientations, the two determined etching rates are mean values for the two predominant regimes, i.e., the quickly and the slowly etching regime.

After a fluoride treatment of the HAp sample (5 min in 500 ppm NaF at pH 6 and 37 °C) and subsequent cleaning in an ultrasonic bath in ultrapure water, the etching behavior of the surface was drastically changed: For at least 330 s the HAp surface was virtually inert to the NaAc buffer (c.f. Figs. 5.3c and d). Consequently, an etching rate of $r_{\text{fHAp,slow}} \approx 0 \text{ nm s}^{-1}$ has been found for the fluoridated HAp in the first 330 s of etching. After prolonged etching intervals, some areas of the fluoridated surface started to erode with an etching rate of $r_{\text{fHAp,fast}} = 0.204 \pm 0.006 \text{ nm s}^{-1}$ while the major part of the material was still apparently unaffected by the acidic environment. Interestingly, the ablation rate that has been found for the quickly etching parts of the fluoridated sample, $r_{\text{fHAp,fast}}$, is approximately the same as $r_{\text{HAp,fast}}$, the etching rate of the quickly ablated

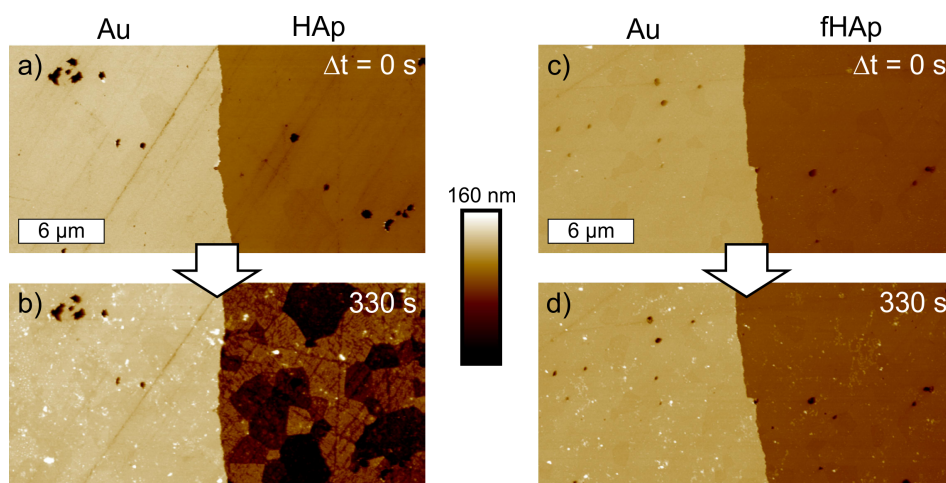


Figure 5.3: Representative AFM micrographs of partially gold-covered HAp surfaces. a) Pure HAp before etching and b) after 330 s in NaAc buffer at pH 4.5. The HAp surface is heavily corroded. c) Fluoridated HAp (fHAp) before etching and d) after 330 s in NaAc buffer at pH 4.5. Up until then, the fHAp surface withstood the acid attack unharmed.

parts of the untreated sample. This indicates that the protective effect observed earlier wears off depending on the crystallites' orientation and that during the acid treatment F^- ions are released preferentially from crystallites lying with their c -axis parallel to the surface normal.

Due to the application of ultrasound for cleaning after fluoride treatment, the fluoride levels at the surface have been significantly lower than in the fluoride uptake experiments described in Addendum II. XPS measurements directly after fluoridation revealed a fluoride content of only about 0.25 at-%. Hence, it is very striking how large the effect of a fluoridated layer of such low concentration can be.

5.4 Bacterial Adhesion to Hydroxyapatite Surfaces

Since many bacterial species can produce enamel-damaging acids over long periods of time, they are the main culprits when a caries lesion forms. Therefore, the adhesion of bacteria to PLS HAp samples has been investigated in greater detail. In the publication by Spengler et al. in *Journal of Molecular Recognition* 2017 (Addendum IV), the influence of saliva on the adhesion behavior of *Streptococcus mutans*, a species well known for its occurrence in the oral cavity and its role in the development of dental caries, and of *Staphylococcus carnosus*, which usually is not present in the human mouth, yet serves for comparison, has been examined.

It could be shown that the interaction between *S. mutans* and HAp is much stronger than that between *S. carnosus* and HAp: Both before and after treatment of the cells with saliva, the adhesion force, rupture length, and de-adhesion work all have shown

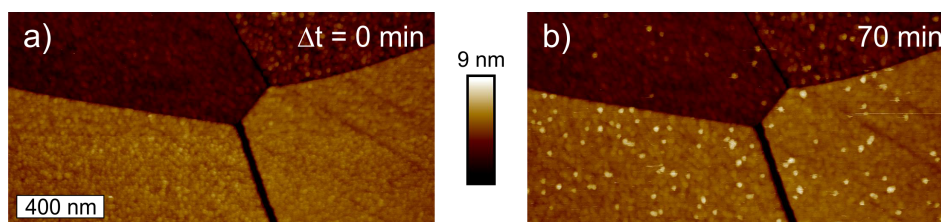


Figure 5.4: Micrographs of a HAp surface during a protein adsorption experiment with AFM in a fluid cell a) before and b) 70 min after the addition of proteins to the buffer solution flowing over the surface.

considerably higher values for *S. mutans* than for *S. carnosus*. After inoculation of the bacterial cells in human saliva, adhesion force, rupture length, and de-adhesion work of both species are significantly increased. However, in the case of *S. mutans*, this effect is much more pronounced than in the case of *S. carnosus*. As especially the rupture length and the de-adhesion work are affected by the salivary treatment, it has been concluded that mainly long macromolecules cause the changed adhesion behavior. These additional macromolecules may either be produced by the bacterial cell upon the contact to saliva, or they may be part of the saliva and attach to the cell wall during salivary treatment. The fact that *S. mutans* benefits much more from the inoculation in saliva shows how well adapted this bacterial species is to its natural habitat, the oral cavity.

5.5 Protein Adsorption and Single Molecule Force Spectroscopy

The acquired enamel pellicle (c.f. Section 3.4.2) is known to modulate the bacterial adhesion forces to tooth surfaces. Therefore, experiments have been designed that will enable a more comprehensive understanding of the interaction of proteins with HAp. In the article by **Zeitz et al. in *ACS Applied Materials & Interfaces* 2016** (Addendum I), *in situ* AFM flow chamber experiments have been presented. It has been shown that, thanks to the low roughness of the HAp surface, the adsorption of single bovine serum albumin (BSA) molecules can be observed (see Fig. 5.4, and Fig. 9 in Addendum I). Interestingly, different adsorption rates have been detected on neighboring crystallites which may be due to differences in roughness, crystal orientation, or chemical termination of the surface. However, as these parameters are coupled due to the design of the presented experiments, the real origin of the varying adsorption rates is yet to be explored.

Another approach to further understand the interaction between a protein and a surface is AFM based single molecule force spectroscopy. In this technique, a single protein is tethered to an AFM tip, which allows for a direct measurement of the molecule's adhesion force to a surface. In the publication by **Hauf et al. in *ChemBioChem* 2017** (Addendum V), the adhesion forces of modified mussel foot proteins to a mica surface have been measured before and after irradiation with UV light. The proteins have been

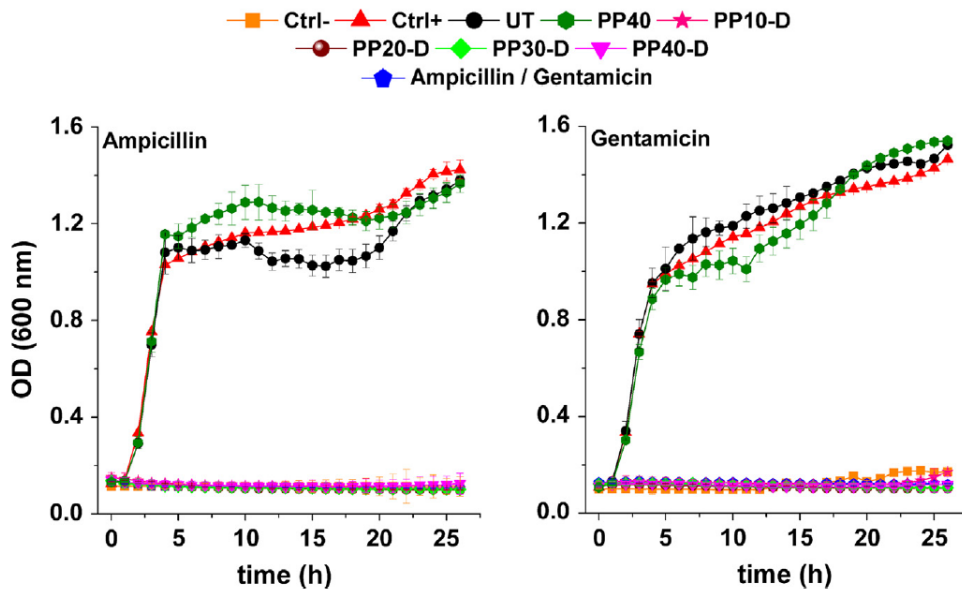


Figure 5.5: Optical density (OD) of *S. aureus* suspensions depending on their contact time with a substrate. While bacterial growth was detected on untreated (UT) and plasma polymerized (40 min, PP40) TCP, all drug-loaded plasma polymerized TCP substrates (PPXX-D) clearly show antibacterial properties. (Reprint from Ref. [3])

modified in such a way that the DOPA residues, which are believed to be primarily responsible for the strong adhesion of the mussel foot, were shielded by photocleavable side groups. Thus, a significant increase of the adhesion force could be observed after UV irradiation. In the context of this thesis, these experiments can be seen as a proof of concept and a first step in the field of single molecule force spectroscopy in our laboratory.

5.6 Plasma Polymerization of Bioceramics

Because of their biocompatibility, bioceramics like HAp or tricalcium phosphate (TCP, $\text{Ca}_3(\text{PO}_4)_2$) are often used in bone grafts or coatings for dental implants [125, 126]. While the coating of bioceramics is a good measure to control some of their properties such as, e.g., the release rate of a drug that may be incorporated into a bone graft to be delivered locally, such coatings can also have unforeseen effects on the material.

In the publication by **Khurana et al.** in *European Polymer Journal* 2018 [3], it has been reported that even though both the coated material, β -TCP, and the coating, a PEG-like coating via plasma polymerization, on their own are hydrophilic, the coated TCP shows macroscopic contact angles larger than 120° with strong pinning of droplets on the surface. This behavior has been attributed to the roughness of the surface and resulting wetting according to Wenzel's model [127].

The thickness of the coatings has been shown to increase with longer plasma polymerization treatment time (10 min, 20 min, 30 min, and 40 min were tested) and thicknesses between around 10 nm and around 38 nm have been measured. While the coatings, depending on their thickness, reduce the drug release of two tested antibiotics (ampicillin and gentamicin), the antibacterial properties of the drug-loaded TCP can still be preserved (c.f. Fig. 5.5) and the biocompatibility is not changed in terms of cell adhesion, proliferation, and morphology. These results can lay the foundation for the development of new designs for bone grafts or dental implants.

6 Summary and Outlook

6.1 Summary

In order to improve our understanding of how and why the fluoridation of tooth enamel poses an efficient strategy in caries prophylaxis, experiments concerning the uptake of fluoride and its impact on the acid resistance have been performed. Since natural tooth enamel is a highly complex material that shows variations in its chemical and structural composition, HAp model systems have been developed which are better suited for the presented experiments: They are easily reproducible without the compositional variations found in natural specimens, they are free from impurities (e.g., fluoride) that could affect sensitive chemical measurements and, if needed, their size can be optimized for a desired measurement technique or experimental design. These improvements in comparison with natural enamel were achieved while maintaining the general chemical structure and stoichiometry of enamel crystallites, but at the cost of the microscopic hierarchical structure and the organic matrix found in real teeth. Therefore, these model systems should be understood not as a model for a whole tooth or a large piece of enamel, but as a model for a single enamel crystallite scaled to a size that allows for the desired experiments to be performed.

Fluoridation experiments with these model systems have shown that the uptake of fluoride in HAp from aqueous solution is limited in terms of the overall amount of fluoride that gets taken up and in terms of the thickness of the fluoridated layer that forms. Furthermore, the presented results show that these limits are reached within a few minutes. While an exact transfer of the results to the complex biological system of a fluoridated tooth is difficult, these findings at least show that the typical time span of the application of dental healthcare products, e.g., toothbrushing for 2 min, is of the right order of magnitude to reach a considerable fluoridation of the tooth surface. The majority of the fluoride taken up is, however, only loosely bound to the surface and can therefore easily be removed.

Although the fluoridated layer thickness is only in the range of a few nm and the concentration of tightly bound fluoride is extremely low, etching experiments have revealed a strong impact of the fluoride treatment on the acid resistance of HAp. When exposed to an acidic solution, a non-fluoridated polycrystalline HAp surface is etched inhomogeneously with etching rates depending on the orientations of the crystallites. After fluoride treatment, irrespective of the crystal orientation, the etching rates have been observed to be decreased by 100% for a limited time of about 5 min. Prolonged etching removes this protection on some areas of the surface and leads to roughly the same etching rates as observed on a pristine HAp surface. However, this development also seems to be dependent on crystal

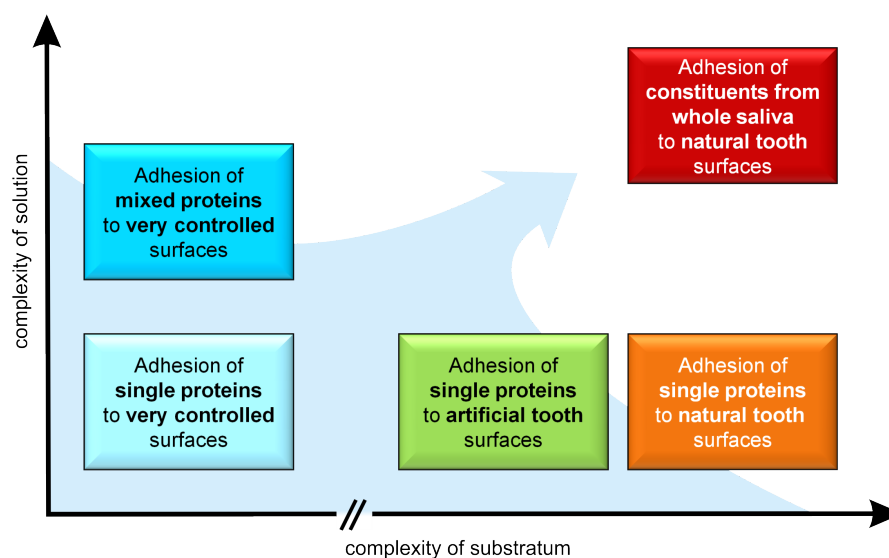


Figure 6.1: Our bottom-up approach includes the investigation of the adhesion of single proteins to very controlled surfaces (e.g., silicon or mica) [128], before more complex “artificial tooth” model surfaces (i.e., HAp) have been used. The final goal is to understand the adhesion of constituents adsorbing from whole saliva onto natural tooth surfaces.

orientations as the major part of the surface stays apparently inert to acidic attacks for more than 23 min.

As one of the main culprits in the development of caries lesions, *S. mutans* cells have been analyzed concerning their adhesion to HAp surfaces. It has been found that the contact to human saliva boosts the adhesion of these bacteria significantly. Another bacterial species, *S. carnosus*, that is usually not associated with the oral cavity has also shown this effect, but far less pronounced than *S. mutans*. Therefore, it can be concluded that *S. mutans* is well adapted to its natural habitat.

Protein adsorption has been investigated via *in situ* AFM experiments. Different adsorption rates have been observed on neighboring crystallites, raising the question whether these differences stem from differing crystal orientations, surface roughness, chemical surface termination or a combination of these parameters. As a complementary approach to a better understanding of protein adsorption, first experiments with AFM based single molecule force spectroscopy have been performed.

6.2 Outlook

Additional protein adsorption measurements can give new insights into the development of the acquired enamel pellicle. Saliva is a very complex fluid that contains over 1000 different proteins [45]. Following a bottom-up approach, our previous protein adsorption experiments were focused on only one protein. Thus, experiments with more complex

protein solutions containing constituents of saliva will bring our model system closer to the natural scenario (c.f. Fig. 6.1). Besides changing the composition of the protein solution, adsorption experiments on fluoridated HAp surfaces may be performed that can further elucidate how the fluoridation affects pellicle formation. Since these adsorption studies in a fluid cell do not yield information about the bond strengths of adsorbing particles, experiments utilizing single molecule force spectroscopy may be performed on HAp surfaces in order to complement the fluid cell results.

Further force spectroscopy measurements with single bacterial cells will be needed to understand the early stages in biofilm formation more comprehensively. In order to discern influences of different parameters, several series of experiments are conceivable, for example, measurements on fluoridated and pristine HAp, and experiments on HAp surfaces before and after treatment with saliva or less complex protein solutions.

A next step in our bottom-up approach of understanding the behavior of the tooth surface could be to develop improved HAp model systems which mimic dental enamel more closely. This could be achieved by incorporating additional elements found in the natural material like sodium, magnesium or chloride, or by modifying the microscopic structure of the HAp samples to better resemble the hierarchical layout of enamel. There, a possible approach would be to utilize ameloblasts, the enamel-forming cells, and to find a way for these cells to build enamel or enamel-like material *in vitro*. Experiments that do not implicitly need a very controlled chemical composition or an extremely low surface roughness may also be performed on natural enamel specimens.

All these possible future experiments may further improve our understanding of the formation of oral biofilms and the influence of incorporated fluoride on the behavior and the properties of the tooth surface.

References

- [1] GBD 2016 Disease and Injury Incidence and Prevalence Collaborators. “Global, regional, and national incidence, prevalence, and years lived with disability for 328 diseases and injuries for 195 countries, 1990–2016: a systematic analysis for the Global Burden of Disease Study 2016”. *Lancet* 390 (2017), pp. 1211–1259. DOI: 10.1016/s0140-6736(17)32154-2.
- [2] J. D. B. Featherstone. “The continuum of dental caries—evidence for a dynamic disease process”. *J. Dent. Res.* 83 (2004), pp. 39–42. DOI: 10.1177/154405910408301s08.
- [3] K. Khurana, F. Müller, K. Jacobs, T. Faidt, J. U. Neurohr, S. Grandthyll, F. Mücklich, C. Canal, and M. P. Ginebra. “Plasma polymerized bioceramics for drug delivery: Do surface changes alter biological behaviour?” *Eur. Polym. J.* 107 (2018), pp. 25–33. DOI: 10.1016/j.eurpolymj.2018.07.016.
- [4] P. A. Oesch, G. Brammer, P. G. van Dokkum, G. D. Illingworth, R. J. Bouwens, I. Labbé, M. Franx, I. Momcheva, M. L. N. Ashby, G. G. Fazio, V. Gonzalez, B. Holden, D. Magee, R. E. Skelton, R. Smit, L. R. Spitler, M. Trenti, and S. P. Willner. “A remarkably luminous galaxy at $Z = 11.1$ measured with Hubble space telescope Grism spectroscopy”. *Astrophys. J.* 819 (2016), p. 129. DOI: 10.3847/0004-637X/819/2/129.
- [5] J. N. Israelachvili. *Intermolecular and surface forces*. Amsterdam, The Netherlands: Academic Press, 2011.
- [6] K. Kopitzki and P. Herzog. *Einführung in die Festkörperphysik*. Wiesbaden, Germany: B.G. Teubner GmbH, 2007.
- [7] D. Leckband and J. Israelachvili. “Intermolecular forces in biology”. *Q. Rev. Biophys.* 34 (2001), pp. 105–267. DOI: 10.1017/S0033583501003687.
- [8] B. V. Derjaguin and L. Landau. “Theory of the stability of strongly charged lyophobic sols and of the adhesion of strongly charged particles in solutions of electrolytes”. *Acta Physicochim. U.R.S.S.* 14 (1941), pp. 633–662. DOI: 10.1016/0079-6816(93)90013-L.
- [9] E. J. W. Verwey and J. T. G. Overbeek. *Theory of the stability of lyophobic colloids*. Amsterdam, The Netherlands: Elsevier Publishing Company, Inc., 1948.
- [10] C. E. Mortimer and U. Müller (translation & editing). *Chemie: das Basiswissen der Chemie*. Stuttgart: Thieme, 2001.

- [11] R. Snyders, D. Music, D. Sigumonrong, B. Schelnberger, J. Jensen, and J. M. Schneider. “Experimental and *ab initio* study of the mechanical properties of hydroxyapatite”. *Appl. Phys. Lett.* 90 (2007), p. 193902. DOI: 10.1063/1.2738386.
- [12] M. I. Kay, R. A. Young, and A. S. Posner. “Crystal structure of hydroxyapatite”. *Nature* 204 (1964), pp. 1050–1052. DOI: 10.1038/2041050a0.
- [13] J. C. Elliot. *Structure and Chemistry of the Apatites and Other Calcium Orthophosphates*. Amsterdam, The Netherlands: Elsevier Science B. V., 1994.
- [14] M. Epple. *Biomaterialien und Biomineralisation*. Wiesbaden, Germany: B. G. Teubner Verlag, 2003.
- [15] M. Sydney-Zax, I. Mayer, and D. Deutsch. “Carbonate Content in Developing Human and Bovine Enamel”. *J. Dent. Res.* 70 (1991), pp. 913–916. DOI: 10.1177/00220345910700051001.
- [16] E. C. Moreno and T. Aoba. “Comparative solubility study of human dental enamel, dentin, and hydroxyapatite”. *Calcif. Tissue Int.* 49 (1991), pp. 6–13. DOI: 10.1007/BF02555895.
- [17] N. H. de Leeuw. “Computer simulations of structures and properties of the biomaterial hydroxyapatite”. *J. Mater. Chem.* 20 (2010), pp. 5376–5386. DOI: 10.1039/B921400C.
- [18] A. Kafilak-Hachulska, A. Samoson, and W. Kolodziejski. “ ^1H MAS and $^1\text{H} \rightarrow ^{31}\text{P}$ CP/MAS NMR study of human bone mineral”. *Calcif. Tissue Int.* 73 (2003), pp. 476–486. DOI: 10.1007/s00223-002-2111-5.
- [19] P. D. Moens, F. J. Callens, P. F. Matthys, and R. M. Verbeeck. “ ^{31}P and ^1H powder ENDOR and molecular orbital study of a CO_3^{3-} ion in X-irradiated carbonate containing hydroxyapatites”. *J. Chem. Soc., Faraday Trans.* 90 (1994), pp. 2653–2662. DOI: 10.1039/FT9949002653.
- [20] P. D. Frazier. “Adult Human Enamel: An Electron Microscopic Study of Crystallite Size and Morphology”. *J. Ultrstruct. Res.* 22 (1968), pp. 1–11. DOI: 10.1016/S0022-5320(68)90045-2.
- [21] G. Daculsi, J. Menanteau, L. M. Kerebel, and D. Mitre. “Length and Shape of Enamel Crystals”. *Calcif. Tissue Int.* 36 (1984), pp. 550–555. DOI: 10.1016/S0022-5320(68)90045-2.
- [22] M. C. Maas and E. R. Dumont. “Built to Last: The Structure, Function, and Evolution of Primate Dental Enamel”. *Evol. Anthropol.* 8 (1999), pp. 133–152. DOI: 10.1002/(SICI)1520-6505(1999)8:4<133::AID-EVAN4>3.0.CO;2-F.
- [23] C. Zeitz. “Analyse und Modifikation von Zahn- und Zahnersatzmaterialien: Struktur – Zusammensetzung – Fluorierung”. Diplomarbeit. Saarbrücken, Germany: Universität des Saarlandes, 2008.

-
- [24] A. C. Tas, F. Korkusuz, M. Timucin, and N. Akkas. “An investigation of the chemical synthesis and high-temperature sintering behaviour of calcium hydroxyapatite (HA) and tricalcium phosphate (TCP) bioceramics”. *J. Mater. Sci. Mater. Med.* 8 (1997), pp. 91–96. DOI: 10.1023/A:1018506800033.
- [25] S. Koutsopoulos. “Synthesis and characterization of hydroxyapatite crystals: a review study on the analytical methods”. *J. Biomed. Mater. Res.* 62 (2002), pp. 600–612. DOI: 10.1002/jbm.10280.
- [26] N. Y. Mostafa. “Characterization, thermal stability and sintering of hydroxyapatite powders prepared by different routes”. *Mater. Chem. Phys.* 94 (2005), pp. 333–341. DOI: 10.1016/j.matchemphys.2005.05.011.
- [27] E. M. Rivera, M. Araiza, W. Brostow, V. M. Castano, J. R. Diaz-Estrada, R. Hernandez, and J. R. Rodriguez. “Synthesis of hydroxyapatite from eggshells”. *Mater. Lett.* 41 (1999), pp. 128–134. DOI: 10.1016/S0167-577X(99)00118-4.
- [28] J. Arends, J. Schuthof, W. H. van der Lindwen, P. Bennema, and P. J. van der Berg. “Preparation of pure hydroxyapatite single crystals by hydrothermal recrystallization”. *J. Cryst. Growth* 46 (1979), pp. 213–220. DOI: 10.1016/0022-0248(79)90060-5.
- [29] F. Wakai, Y. Kodama, S. Sakaguchi, and T. Nonami. “Superplasticity of hot isostatically pressed hydroxyapatite”. *J. Am. Ceram. Soc.* 73 (1990), pp. 457–460. DOI: 10.1111/j.1151-2916.1990.tb06537.x.
- [30] Y. Fang, D. K. Agrawal, D. M. Roy, and R. Roy. “Microwave sintering of hydroxyapatite ceramics”. *J. Mater. Res.* 9 (1994), pp. 180–187. DOI: 10.1557/JMR.1994.0180.
- [31] S. Vijayan and H. Varma. “Microwave sintering of nanosized hydroxyapatite powder compacts”. *Mater. Lett.* 56 (2002), pp. 827–831. DOI: 10.1016/S0167-577X(02)00622-5.
- [32] Y. W. Gu, N. H. Loh, K. A. Khor, S. T. Tor, and P. Cheang. “Spark plasma sintering of hydroxyapatite powders”. *Biomaterials* 23 (2002), pp. 37–43. DOI: 10.1016/S0142-9612(01)00076-X.
- [33] O. Prokopiev, I. Sevostianov, J. Genin, S. M. McGee, and C. Woodward. “Microstructure and Elastic Properties of Sintered Hydroxyapatite”. *Int. J. Fract.* 130 (2004), pp. L183–L190. DOI: 10.1007/s10704-004-2589-0.
- [34] O. Prokopiev and I. Sevostianov. “Dependence of the Mechanical Properties of Sintered Hydroxyapatite on the Sintering Temperature”. *Mater. Sci. Eng. A* 431 (2006), pp. 218–227. DOI: 10.1016/j.msea.2006.05.158.
- [35] F. Müller, C. Zeitz, H. Mantz, K.-H. Ehses, F. Soldera, J. Schmauch, M. Hannig, S. Hüfner, and K. Jacobs. “Elemental depth profiling of fluoridated hydroxyapatite: saving your dentition by the skin of your teeth?” *Langmuir* 26 (2010), pp. 18750–18759. DOI: 10.1021/la102325e.

- [36] C. Zeitz. “Zahnhartgewebe im Fokus: *In vitro*-Untersuchungen zur Biokompatibilität von fluorierten und nicht-fluorierten Hydroxylapatit-Modelloberflächen”. Dissertation. Saarbrücken, Germany: Universität des Saarlandes, 2013. DOI: 10.22028/D291-22916.
- [37] P. Loskill, C. Zeitz, S. Grandthyll, N. Thewes, F. Müller, M. Bischoff, M. Herrmann, and K. Jacobs. “Reduced Adhesion of Oral Bacteria on Hydroxyapatite by Fluoride Treatment”. *Langmuir* 29 (2013), pp. 5528–5533. DOI: 10.1021/la4008558.
- [38] Q. Ruan and J. Moradian-Oldak. “Amelogenin and enamel biomimetics”. *J. Mater. Chem. B* 3 (2015), pp. 3112–3129. DOI: 10.1039/C5TB00163C.
- [39] M. Pandya and T. G. H. Diekwisch. “Enamel biomimetics—fiction or future of dentistry”. *Int. J. Oral Sci.* 11 (2019), p. 8. DOI: 10.1038/s41368-018-0038-6.
- [40] H. Chen, B. H. Clarkson, K. Sun, and J. F. Mansfield. “Self-assembly of synthetic hydroxyapatite nanorods into an enamel prism-like structure”. *J. Colloid Interface Sci.* 288 (2005), pp. 97–103. DOI: 10.1016/j.jcis.2005.02.064.
- [41] Y. Zhou, Y. Zhou, L. Gao, C. Wu, and J. Chang. “Synthesis of artificial dental enamel by an elastin-like polypeptide assisted biomimetic approach”. *J. Mater. Chem. B* 6 (2018), pp. 844–853. DOI: 10.1039/C7TB02576A.
- [42] H.-P. Yu, Y.-J. Zhu, and B.-Q. Lu. “Dental enamel-mimetic large-sized multi-scale ordered architecture built by a well controlled bottom-up strategy”. *Chem. Eng. J.* 360 (2019), pp. 1633–1645. DOI: 10.1016/j.cej.2018.11.025.
- [43] B. J. Paster, S. K. Boches, J. L. Galvin, R. E. Ericson, C. N. Lau, V. A. Levanos, A. Sahasrabudhe, and F. E. Dewhirst. “Bacterial diversity in human subgingival plaque”. *J. Bacteriol.* 183 (2001), pp. 3770–3783. DOI: 10.1128/JB.183.12.3770-3783.2001.
- [44] P. D. Marsh. “Dental biofilms in health and disease”. *Understanding Dental Caries: From Pathogenesis to Prevention and Therapy*. Ed. by M. Goldberg. Switzerland: Springer International Publishing, 2016, pp. 41–52.
- [45] S. Hu, J. A. Loo, and D. T. Wong. “Human saliva proteome analysis”. *Ann. N. Y. Acad. Sci.* 1098 (2007), pp. 323–329. DOI: 10.1196/annals.1384.015.
- [46] W. J. Loesche. “Role of *Streptococcus mutans* in human dental decay”. *Microbiol. Rev.* 50 (1986), pp. 353–380.
- [47] J. A. Aas, A. L. Griffen, S. R. Dardis, A. M. Lee, I. Olsen, F. E. Dewhirst, E. J. Leys, and B. J. Paster. “Bacteria in dental caries in primary and permanent teeth in children and young adults”. *J. Clin. Microbiol.* 46 (2008), pp. 1407–1417. DOI: 10.1128/JCM.01410-07.
- [48] P. D. Marsh. “Dental plaque as a microbial biofilm”. *Caries Res.* 38 (2004), pp. 204–211. DOI: 10.1159/000077756.
- [49] M. Hannig and A. Joiner. “The structure, function and properties of the acquired pellicle”. *Monogr. Oral Sci.* 19 (2006), pp. 29–64. DOI: 10.1159/000090585.

-
- [50] M. Hannig. “Ultrastructural investigation of pellicle morphogenesis at two different intraoral sites during a 24-h period”. *Clin. Oral Investig.* 3 (1999), pp. 88–95. DOI: 10.1007/s007840050084.
- [51] K. K. Skjörland, M. Rykke, and T. Sønju. “Rate of pellicle formation in vivo”. *Acta Odontol. Scand.* 53 (1995), pp. 358–362. DOI: 10.3109/00016359509006001.
- [52] B. T. Amaechi, S. M. Higham, W. M. Edgar, and A. Milosevic. “Thickness of acquired salivary pellicle as a determinant of the sites of dental erosion”. *J. Dent. Res.* 78 (1999), pp. 1821–1828. DOI: 10.1177/00220345990780120901.
- [53] Y. Yao, E. A. Berg, C. E. Costello, R. F. Troxler, and F. G. Oppenheim. “Identification of protein components in human acquired enamel pellicle and whole saliva using novel proteomics approaches”. *J. Biol. Chem.* 278 (2003), pp. 5300–5308. DOI: 10.1074/jbc.M206333200.
- [54] J. Delius, S. Trautmann, G. Médard, B. Kuster, M. Hannig, and T. Hofmann. “Label-free quantitative proteome analysis of the surface-bound salivary pellicle”. *Colloids Surf. B* 152 (2017), pp. 68–76. DOI: 10.1016/j.colsurfb.2017.01.005.
- [55] A. Aguirre, B. Mendoza, M. J. Levine, M. N. Hatton, and W. H. Douglas. “*In vitro* characterization of human salivary lubrication”. *Arch. Oral Biol.* 34 (1989), pp. 675–677. DOI: 10.1016/0003-9969(89)90024-1.
- [56] R. T. Zahradnik, E. C. Moreno, and E. J. Burke. “Effect of salivary pellicle on enamel subsurface demineralization in vitro”. *J. Dent. Res.* 55 (1976), pp. 664–670. DOI: 10.1177/00220345760550042101.
- [57] S. Joyston-Bechal, R. Duckworth, and M. Braden. “The effect of artificially produced pellicle and plaque on the uptake of ^{18}F by human enamel in vitro”. *Arch. Oral Biol.* 21 (1976), pp. 73–78. DOI: 10.1016/0003-9969(76)90074-1.
- [58] U. Lendenmann, J. Grogan, and F. G. Oppenheim. “Saliva and dental pellicle - a review”. *Adv. Dent. Res.* 14 (2000), pp. 22–28. DOI: 10.1177/08959374000140010301.
- [59] W. B. Clark, L. L. Bammann, and R. L. Gibbons. “Comparative estimates of bacterial affinities and adsorption sites on hydroxyapatite surfaces”. *Infect. Immun.* 19 (1978), pp. 846–853.
- [60] A. Carlén, K. Nikdel, A. Wennerberg, K. Holmberg, and J. Olsson. “Surface characteristics and in vitro biofilm formation on glass ionomer and composite resin”. *Biomaterials* 22 (2001), pp. 481–487. DOI: 10.1016/S0142-9612(00)00204-0.
- [61] W. L. Jongebloed, P. J. van den Berg, and J. Arends. “The dissolution of single crystals of hydroxyapatite in citric and lactic acids”. *Calcif. Tissue Res.* 15 (1974), pp. 1–9. DOI: 10.1007/BF02059038.
- [62] K.-Y. Kwon, E. Wang, A. Chung, N. Chang, E. Saiz, U.-J. Choe, M. Koobatian, and S.-W. Lee. “Defect induced asymmetric pit formation on hydroxyapatite”. *Langmuir* 24 (2008), pp. 11063–11066. DOI: 10.1021/la801735c.

- [63] M. T. Fulmer, I. C. Ison, C. R. Hankermayer, B. R. Constantz, and J. Ross. "Measurements of the solubilities and dissolution rates of several hydroxyapatites". *Biomaterials* 23 (2002), pp. 751–755. DOI: 10.1016/S0142-9612(01)00180-6.
- [64] D. G. A. Nelson. "The influence of carbonate on the atomic structure and reactivity of hydroxyapatite". *J. Dent. Res.* 60 (1981), pp. 1621–1629. DOI: 10.1177/0022034581060003S1201.
- [65] A. B. Barry, H. Zhuang, A. A. Baig, and W. I. Higuchi. "Effect of fluoride pretreatment on the solubility of synthetic carbonated apatite". *Calcif. Tissue Int.* 72 (2003), pp. 236–242. DOI: 10.1007/s00223-001-1069-z.
- [66] H. B. Pan and B. W. Darvell. "Solubility of calcium fluoride and fluorapatite by solid titration". *Arch. Oral Biol.* 52 (2007), pp. 861–868. DOI: 10.1016/j.archoralbio.2007.03.002.
- [67] K.-Y. Kwon, E. Wang, M. Nofal, and S.-W. Lee. "Microscopic study of hydroxyapatite dissolution as affected by fluoride ions". *Langmuir* 27 (2011), pp. 5335–5339. DOI: 10.1021/1a200325d.
- [68] J. D. B. Featherstone and J. M. ten Cate. "Physicochemical Aspects of Fluoride-Enamel-Interactions". *Fluoride in Dentistry*. Ed. by J. Ekstrand, O. Fejerskov, and L. M. Silverstone. Copenhagen, Denmark: Munksgaard International Publishers, 1988, pp. 125–149.
- [69] C. Dawes. "What Is the Critical pH and Why Does a Tooth Dissolve in Acid?" *J. Can. Dent. Assoc.* 69 (2003), pp. 722–724.
- [70] H. Margolis and E. Moreno. "Kinetics of hydroxyapatite dissolution in acetic, lactic, and phosphoric acid solutions". *Calcif. Tissue Int.* 50 (1992), pp. 137–143. DOI: 10.1007/BF00298791.
- [71] M. R. Christoffersen, J. Christoffersen, and J. Arends. "Kinetics of dissolution of calcium hydroxyapatite VII: The effect of fluoride ions". *J. Cryst. Growth* 67 (1984), pp. 107–114. DOI: 10.1016/0022-0248(84)90138-6.
- [72] A. A. Baig, R. V. Faller, J. Yan, N. Ji, M. Lawless, and S. L. Eversole. "Protective effects of SnF₂ – Part I. Mineral solubilisation studies on powdered apatite". *Int. Dent. J.* 64 (2014), pp. 4–10. DOI: 10.1111/idj.12096.
- [73] M. M. Manarelli, J. P. Pessan, A. C. B. Delbem, J. G. Amaral, M. F. Paiva, and M. E. Barbour. "Protective effect of phosphates and fluoride on the dissolution of hydroxyapatite and their interactions with saliva". *Caries Res.* 51 (2017), pp. 96–101. DOI: 10.1159/000452716.
- [74] S. Takagi, H. Liao, and L. C. Chow. "Effect of tooth-bound fluoride on enamel demineralization/ remineralization in vitro". *Caries Res.* 34 (2000), pp. 281–288. DOI: 10.1159/000016603.
- [75] C. Ganss, N. Schlueter, M. Hardt, P. Schattenberg, and J. Klimek. "Effect of fluoride compounds on enamel erosion in vitro: a comparison of amine, sodium and stannous fluoride". *Caries Res.* 42 (2008), pp. 2–7. DOI: 10.1159/000111743.

-
- [76] B.-S. Lee, P.-H. Chou, S.-Y. Chen, H.-Y. Liao, and C.-C. Chang. “Prevention of enamel demineralization with a novel fluoride strip: enamel surface composition and depth profile”. *Sci. Rep.* 5 (2015), p. 13352. DOI: 10.1038/srep13352.
- [77] J. Arends and J. Christoffersen. “Nature and role of loosely bound fluoride in dental caries”. *J. Dent. Res.* 69 (1990), pp. 601–605. DOI: 10.1177/00220345900690S118.
- [78] H. T. Dean, F. A. Arnold, and E. Elvove. “Domestic Water and Dental Caries”. *Public Health Rep.* 57 (1942), pp. 1155–1179. DOI: 10.2307/4584182.
- [79] J. E. Creeth, R. Karwal, A. T. Hara, and D. T. Zero. “A Randomized in situ Clinical Study of Fluoride Dentifrices on Enamel Remineralization and Resistance to Demineralization: Effects of Zinc”. *Caries Res.* 52 (2018), pp. 129–138. DOI: 10.1159/000479823.
- [80] R. F. Zanatta, D. M. S. Ávila, K. M. Miyamoto, C. R. G. Torres, and A. B. Borges. “Influence of Surfactants and Fluoride against Enamel Erosion”. *Caries Res.* 53 (2019), pp. 1–9. DOI: 10.1159/000488207.
- [81] J. M. ten Cate and J. D. B. Featherstone. “Mechanistic aspects of the interactions between fluoride and dental enamel”. *Crit. Rev. Oral Biol. Med.* 2 (1991), pp. 283–296. DOI: 10.1177/10454411910020030101.
- [82] J. M. ten Cate. “Current concepts on the theories of the mechanism of action of fluoride”. *Acta Odontol. Scand.* 57 (1999), pp. 325–329. DOI: 10.1080/000163599428562.
- [83] J. Qin, G. Chai, J. M. Brewer, L. L. Lovelace, and L. Lebioda. “Fluoride Inhibition of Enolase: Crystal Structure and Thermodynamics”. *Biochemistry* 45 (2006), pp. 793–800. DOI: 10.1021/bi051558s.
- [84] P. Denbesten, R. Faller, and Y. Nakano. “Fluoride”. *Understanding Dental Caries: From Pathogenesis to Prevention and Therapy*. Ed. by M. Goldberg. Switzerland: Springer International Publishing, 2016, pp. 173–184.
- [85] K. P. K. Olympio, P. A. P. Bardal, V. E. S. Cardoso, R. C. Oliveira, J. R. M. Bastos, and M. A. R. Buzalaf. “Low-fluoride dentifrices with reduced pH: Fluoride concentration in whole saliva and bioavailability”. *Caries Res.* 41 (2007), pp. 365–370. DOI: 10.1159/000104794.
- [86] J. Ennever, J. K. Peterson, W. R. Hester, V. A. Segreto, and A. W. Radike. “Influence of alkaline pH on the effectiveness of sodium fluoride dentifrices”. *J. Dent. Res.* 59 (1980), pp. 658–661. DOI: 10.1177/00220345800590040101.
- [87] J. Mullen. “History of water fluoridation”. *Br. Dent. J.* 199 (2005), pp. 1–4. DOI: 10.1038/sj.bdj.4812863.
- [88] G. Pizzo, M. R. Piscopo, I. Pizzo, and G. Giuliana. “Community water fluoridation and caries prevention: a critical review”. *Clin. Oral Investig.* 11 (2007), pp. 189–193. DOI: 10.1007/s00784-007-0111-6.

- [89] M. R. Sowers, K. M. Clerk, M. L. Jannausch, and R. B. Wallace. “A prospective study of bone mineral content and fracture in communities with differential fluoride exposure”. *Am. J. Epidemiol.* 133 (1991), pp. 649–660. DOI: 10.1093/oxfordjournals.aje.a115940.
- [90] P. J. Mullenix, P. K. Denbesten, A. Schunior, and W. J. Kernan. “Neurotoxicity of sodium fluoride in rats”. *Neurotoxicol. Teratol.* 17 (1995), pp. 169–177. DOI: 10.1016/0892-0362(94)00070-T.
- [91] A. L. Choi, G. Sun, Y. Zhang, and P. Grandjean. “Developmental fluoride neurotoxicity: a systematic review and meta-analysis”. *Environ. Health Perspect.* 120 (2012), pp. 1362–1368. DOI: 10.1289/ehp.1104912.
- [92] Bundesinstitut für Risikobewertung. “Für gesunde Zähne: Fluorid-Vorbeugung bei Säuglingen und Kleinkindern”. *MyCoRe Community* Stellungnahme 015/2018 (2018). DOI: 10.17590/20180531-085715-0.
- [93] V. Sternitzke, R. Kaegi, J. N. Audinot, E. Lewin, J. G. Hering, and C. A. Johnson. “Uptake of fluoride from aqueous solution on nano-sized hydroxyapatite: examination of a fluoridated surface layer”. *Environ. Sci. Technol.* 46 (2012), pp. 802–809. DOI: 10.1021/es202750t.
- [94] Å. Bengtsson, A. Shchukarev, P. Persson, and S. Sjöberg. “Phase transformations, ion-exchange, adsorption, and dissolution processes in aquatic fluorapatite systems”. *Langmuir* 25 (2009), pp. 2355–2362. DOI: 10.1021/la803137u.
- [95] H. G. McCann. “Reaction of fluoride ion with hydroxyapatite”. *J. Biol. Chem.* 201 (1953), pp. 247–259.
- [96] N. H. de Leeuw. “Resisting the onset of hydroxyapatite dissolution through the incorporation of fluoride”. *J. Phys. Chem. B* 108 (2004), pp. 1809–1811. DOI: 10.1021/jp036784v.
- [97] N. H. de Leeuw. “A computer modelling study of the uptake and segregation of fluoride ions at the hydrated hydroxyapatite (0001) surface: introducing a $\text{Ca}_{10}(\text{PO}_4)_6(\text{OH})_2$ potential model”. *Phys. Chem. Chem. Phys.* 6 (2004), pp. 1860–1866. DOI: 10.1039/B313242K.
- [98] A. C. Ramsey, E. J. Duff, L. Paterson, and J. L. Stuart. “The uptake of F^{--} by hydroxyapatite at varying pH”. *Caries Res.* 7 (1973), pp. 231–244. DOI: 10.1159/000259846.
- [99] Y. Tanizawa, H. Tsuchikane, K. Sawamura, and T. Suzuki. “Reaction characteristics of hydroxyapatite with F^- and PO_3F^{2-} ions. Chemical states of fluorine in hydroxyapatite”. *J. Chem. Soc., Faraday Trans.* 87 (1991), pp. 2235–2240. DOI: 10.1039/ft9918702235.
- [100] H. U. V. Gerth, T. Dammaschke, E. Schäfer, and H. Züchner. “A three layer structure model of fluoridated enamel containing CaF_2 , $\text{Ca}(\text{OH})_2$ and FAp”. *Dent. Mater.* 23 (2007), pp. 1521–1528. DOI: 10.1016/j.dental.2006.12.007.

-
- [101] M. Petzold. “The influence of different fluoride compounds and treatment conditions on dental enamel: a descriptive in vitro study of the CaF₂ precipitation and microstructure”. *Caries Res.* 35 (2001), pp. 45–51. DOI: 10.1159/000049110.
- [102] M. Jiménez-Reyes and M. Solache-Ríos. “Sorption behavior of fluoride ions from aqueous solutions by hydroxyapatite”. *J. Hazard. Mater.* 180 (2010), pp. 297–302. DOI: 10.1016/j.jhazmat.2010.04.030.
- [103] J. Lin, S. Raghavan, and D. W. Fuerstenau. “The adsorption of fluoride ions by hydroxyapatite from aqueous solution”. *Colloid. Surface* 3 (1981), pp. 357–370. DOI: 10.1016/0166-6622(81)80062-5.
- [104] H. Uchtmann and H. Duschner. “Electron spectroscopic studies of interactions between superficially-applied fluorides and surface enamel”. *J. Dent. Res.* 61 (1982), pp. 423–428. DOI: 10.1177/00220345820610021201.
- [105] H. Duschner and H. Uchtmann. “Effect of sodium fluoride, stannous fluoride, amine hydrofluoride and sodium monofluorophosphate on the formation of precipitates adhering to bovine enamel”. *Caries Res.* 22 (1988), pp. 65–71. DOI: 10.1159/000261087.
- [106] H. Salmang and H. Scholze. *Keramik*. Ed. by R. Telle. Berlin, Germany: Springer-Verlag, 2007.
- [107] S.-J. L. Kang. *Sintering: Densification, Grain Growth and Microstructure*. Amsterdam, The Netherlands: Butterworth-Heinemann, 2005.
- [108] O. Guillon, J. Gonzalez-Julian, B. Dargatz, T. Kessel, G. Schierning, J. Räthel, and M. Herrmann. “Field Assisted Sintering Technology/Spark Plasma Sintering: Mechanisms, Materials, and Technology Developments”. *Adv. Eng. Mater.* 16 (2014), pp. 830–849. DOI: 10.1002/adem.201300409.
- [109] H. Hertz. “Ueber den Einfluss des ultravioletten Lichtes auf die elektrische Entladung”. *Ann. Phys.* 267 (1887), pp. 983–1000. DOI: 10.1002/andp.18872670827.
- [110] W. Hallwachs. “Ueber den Einfluss des Lichtes auf electrostatisch geladene Körper”. *Ann. Phys.* 269 (1888), pp. 301–312. DOI: 10.1002/andp.18882690206.
- [111] A. Einstein. “Über einen die Erzeugung und Verwandlung des Lichtes betreffenden heuristischen Gesichtspunkt”. *Ann. Phys.* 322 (1905), pp. 132–148. DOI: 10.1002/andp.19053220607.
- [112] M. P. Seah and W. A. Dench. “Quantitative Electron Spectroscopy of Surfaces: A Standard Data Base for Electron Inelastic Mean Free Paths in Solids”. *Surf. Interface Anal.* 1 (1979), pp. 2–11. DOI: 10.1002/sia.740010103.
- [113] S. Hüfner. *Photoelectron Spectroscopy: Principles and Applications*. Berlin, Germany: Springer-Verlag, 1995.
- [114] G. Binnig, C. F. Quate, and Ch. Gerber. “Atomic force microscope”. *Phys. Rev. Lett.* 56 (1986), pp. 930–933. DOI: 10.1103/PhysRevLett.56.930.

- [115] B. Bhushan, ed. *Springer Handbook of Nanotechnology*. Berlin, Germany: Springer Science+Business Media, Inc., 2004.
- [116] P. Eaton and P. West. *Atomic Force Microscopy*. New York City, NY: Oxford University Press Inc., 2010.
- [117] K. D. Sattler, ed. *Handbook of Nanophysics. Principles and Methods*. Boca Raton, FL: CRC Press, Taylor and Francis Group, LLC, 2011.
- [118] B. Voigtländer. *Scanning Probe Microscopy: Atomic Force Microscopy and Scanning Tunneling Microscopy*. Berlin, Germany: Springer-Verlag, 2015.
- [119] G. Binnig, Ch. Gerber, E. Stoll, and T. R. Albrecht. “Atomic resolution with atomic force microscope”. *Europhys. Lett.* 3 (1987), pp. 1281–1286. DOI: 10.1209/0295-5075/3/12/006.
- [120] A. Ebner, L. Wildling, A. Kamruzzahan, C. Rankl, J. Wruss, C. D. Hahn, M. Hölzl, R. Zhu, F. Kienberger, D. Blaas, P. Hinterdorfer, and H. J. Gruber. “A New, Simple Method for Linking of Antibodies to Atomic Force Microscopy Tips”. *Bioconjugate Chem.* 18 (2007), pp. 1176–1184. DOI: 10.1021/bc070030s.
- [121] L. Wildling, B. Unterauer, R. Zhu, A. Rupprecht, T. Haselgrübler, C. Rankl, A. Ebner, D. Vater, P. Pollheimer, E. E. Pohl, P. Hinterdorfer, and H. J. Gruber. “Linking of Sensor Molecules with Amino Groups to Amino-Functionalized AFM Tips”. *Bioconjugate Chem.* 22 (2011), pp. 1239–1248. DOI: 10.1021/bc200099t.
- [122] S. Kang and M. Elimelech. “Bioinspired Single Bacterial Cell Force Spectroscopy”. *Langmuir* 25 (2009), pp. 9656–9659. DOI: 10.1021/la902247w.
- [123] N. Thewes, P. Loskill, P. Jung, H. Peisker, M. Bischoff, M. Herrmann, and K. Jacobs. “Hydrophobic Interaction Governs Unspecific Adhesion of Staphylococci: a Single Cell Force Spectroscopy Study”. *Beilstein J. Nanotechnol.* 5 (2014), pp. 1501–1512. DOI: 10.3762/bjnano.5.163.
- [124] N. Thewes, P. Loskill, C. Spengler, S. Hümbert, M. Bischoff, and K. Jacobs. “A Detailed Guideline for the Fabrication of Single Bacterial Probes Used for Atomic Force Spectroscopy”. *Eur. Phys. J. E* 38 (2015), p. 140. DOI: 10.1140/epje/i2015-15140-2.
- [125] M. H. Zablotsky. “Hydroxyapatite Coatings in Implant Dentistry”. *Implant Dent.* 1 (1992), pp. 253–257. DOI: 10.1097/00008505-199200140-00004.
- [126] B. Liu and D.-X. Lun. “Current Application of β -Tricalcium Phosphate Composites in Orthopaedics”. *Orthop. Surg.* 4 (2012), pp. 139–144. DOI: 10.1111/j.1757-7861.2012.00189.x.
- [127] R. N. Wenzel. “Resistance of Solid Surfaces to Wetting by Water”. *Ind. Eng. Chem.* 28 (1936), pp. 988–994. DOI: 10.1021/ie50320a024.
- [128] H. Hähl, F. Evers, S. Grandthyll, M. Paulus, C. Sternemann, P. Loskill, M. Lessel, A. K. Hüsecken, T. Brenner, M. Tolan, and K. Jacobs. “Subsurface influence on the structure of protein adsorbates as revealed by *in situ* X-ray reflectivity”. *Langmuir* 28 (2012), pp. 7747–7756. DOI: 10.1021/la300850g.

Addenda

Publications

I: Synthesis of Hydroxyapatite Substrates: Bridging the Gap between Model Surfaces and Enamel

Authors: C. Zeitz,¹ T. Faidt,¹ S. Grandthyll,¹ H. Hähl,¹ N. Thewes,¹ C. Spengler,¹ J. Schmauch,¹ M. J. Deckarm,¹ C. Gachot,² H. Natter,³ M. Hannig,⁴ F. Müller,¹ and K. Jacobs¹

¹Experimental Physics, Saarland University, 66123 Saarbrücken, Germany.

²Department of Materials Science, Saarland University, 66123 Saarbrücken, Germany.

³Department of Physical Chemistry, Saarland University, 66123 Saarbrücken, Germany.

⁴Clinic of Operative Dentistry, Periodontology and Preventive Dentistry, Saarland University, 66421 Homburg, Germany.

Reprinted with permission from *ACS Appl. Mater. Interfaces* 8 (2016), pp. 25848–25855.

Copyright 2016 American Chemical Society.

<https://doi.org/10.1021/acsami.6b10089>

Author contributions:

C. Zeitz and T. Faidt produced and characterized hydroxyapatite samples, performed AFM measurements, analyzed measurement data and wrote the manuscript. S. Grandthyll performed XPS measurements and analyzed XPS data. H. Hähl, N. Thewes and C. Spengler assisted in designing figures and in writing the manuscript. J. Schmauch performed TEM, SEM and EBSD measurements. M. J. Deckarm performed XRD measurements. C. Gachot performed micro indentation hardness tests. H. Natter analyzed XRD measurement data. M. Hannig assisted in writing the manuscript. F. Müller directed experimental work, performed XPS measurements, analyzed XPS data and wrote the manuscript. K. Jacobs directed experimental work and wrote the manuscript.

C. Zeitz and T. Faidt contributed equally to this work.

Abstract – Hydroxyapatite substrates are common biomaterials, yet samples of natural teeth or bones do not meet the demands for well-defined, highly reproducible properties. Pellets of hydroxyapatite were produced via the Field Assisted Sintering Technology (FAST) as well as via pressureless sintering (PLS). The applied synthesis routes provide samples of very high density (95 % – 99 % of the crystallographic density) and of very low surface roughness (lower than 1 nm when averaged per 1 μm^2). The chemical composition of the raw material (commercial HAP powder) as well as the crystalline structure is maintained by the sintering processes. These specimens can therefore be considered as promising model surfaces for studies on the interactions of biomaterial with surfaces of biological relevance, as demonstrated for the adsorption of BSA proteins.

Synthesis of Hydroxyapatite Substrates: Bridging the Gap between Model Surfaces and Enamel

Christian Zeitz,[†] Thomas Faidt,[†] Samuel Grandthyll,[†] Hendrik Hähl,[†] Nicolas Thewes,[†] Christian Spengler,[†] Jörg Schmauch,[†] Michael Johannes Deckarm,[†] Carsten Gachot,[‡] Harald Natter,[§] Matthias Hannig,^{||} Frank Müller,^{*,†} and Karin Jacobs^{*,†}

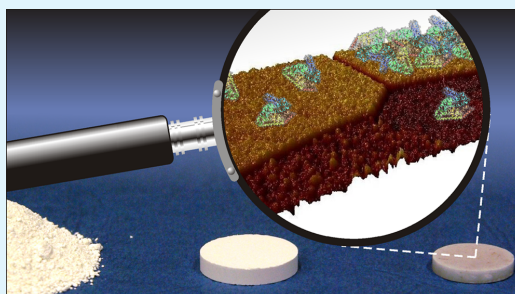
[†]Experimental Physics, [‡]Department of Materials Science, and [§]Physical Chemistry, Saarland University, 66123 Saarbrücken, Germany

^{||}Clinic of Operative Dentistry, Periodontology and Preventive Dentistry, Saarland University, 66421 Homburg, Germany

Supporting Information

ABSTRACT: Hydroxyapatite substrates are common biomaterials, yet samples of natural teeth do not meet the demands for well-defined, highly reproducible properties. Pellets of hydroxyapatite were produced via the field assisted sintering technology (FAST) as well as via pressureless sintering (PLS). The applied synthesis routes provide samples of very high density (95%–99% of the crystallographic density) and of very low surface roughness (lower than 1 nm when averaged per 1 μm^2). The chemical composition of the raw material (commercial HAP powder) as well as the crystalline structure is maintained by the sintering processes. These specimens can therefore be considered as promising model surfaces for studies on the interactions of biomaterial with surfaces of biological relevance, as demonstrated for the adsorption of BSA proteins.

KEYWORDS: atomic force microscopy (AFM), electron backscattering diffraction (EBSD), hydroxyapatite (HAP), field assisted sintering technology (FAST), pressureless sintering (PLS), transmission/scanning electron microscopy (TEM, SEM), protein adsorption, X-ray diffraction (XRD), X-ray photoelectron spectroscopy (XPS)



1. INTRODUCTION

During the past decade, interfaces between soft and hard matter became a dynamic topic in the life sciences.^{1–3} Many physiological processes are influenced by the properties of interfaces, e.g., the growth of biofilms or the adsorption of proteins or bacteria.^{4–9} The specific interaction between an adhering particle and a surface causes a particular behavior of adhering objects on different surfaces.^{10,11} This interaction highly depends on the physicochemical properties of both, particle and surface. Therefore, if a quantitative description of the interaction is intended, the exact chemical composition and the precise structure of the surface and the bulk of the interacting objects have to be considered.^{4–7,12,13} In the case of biomaterials, such as teeth, bones, or any other kind of tissue, the demand for “precise knowledge” typically asks, however, for the impossible, since structure and chemical composition of individual specimens are often subject to large variations. For example, the fluoride content of human teeth—as a parameter that strongly affects the adhesion force between bacteria and enamel⁷—differs for each individual. Therefore, probing the interaction of biomacromolecules, cells, proteins, or bacteria to biomaterials is often restricted to well-defined model surfaces, such as silicon wafers or glass slides. At first sight, investigations

using such substrates resemble pure academic playgrounds under no realistic conditions. Yet, even from these simple model systems, valuable information concerning the impact of surface and subsurface properties on adsorption properties was obtained.⁶ In a second step, it is of course of high interest to consider substrates that combine both the significance of a real-life material and the warranty of well-defined material properties, like surface topography and chemical composition.

Human enamel is a hierarchically organized bioceramic consisting mainly of calcium-deficient hydroxyapatite (HAP: $\text{Ca}_{10}(\text{PO}_4)_6(\text{OH})_2$).^{14,15} On the nanoscale, enamel is composed of apatite crystallites measuring 40–60 nm in diameter and 100–1000 nm in length.¹⁵ On the microscale, the crystallites are arranged in prisms that have a diameter of several micrometers and a length of millimeters.¹⁵ Besides the dominant inorganic components (97%), enamel also contains matrix proteins (1 wt %). The variation of the chemical composition¹⁶ and the structure can be influenced by extrinsic factors, e.g., by physiological processes in the mouth, by the

Received: August 12, 2016

Accepted: September 6, 2016

Published: September 6, 2016

application of fluoride-containing agents, or simply by genetics. Thus, variations in structure and composition of enamel are not unusual, and a quantitative description therefore requires a characterization of each individual specimen.

In terms of the need of standardized tooth-like model surfaces, the present study describes the synthesis and properties of sintered hydroxyapatite samples as approximately representing a single crystallite of enamel.¹⁴ In contrast to previous studies where nano-HAP samples were prepared rather in the light of their application as a biomaterial,^{17,18} the aim of the present study was the synthesis of HAP samples with well-defined, highly reproducible properties to get new enamel-like model samples of biorelevance.

These samples were prepared by the field assisted sintering technology (FAST) of HAP powder and by pressureless sintering (PLS) of precompact HAP powder. In contrast to previous studies where the preparation of sintered HAP samples also included the synthesis of the HAP powder itself,^{19,20} commercial HAP powder (with follow-up treatment) was used in the present case to make the overall synthesis route as simple as possible.

The application of both sintering techniques aims at potential differences in sample properties such as density, grain size, hardness, chemical composition, or crystal structure. The utility of these types of samples has already been proven in previous works concerning depth distribution of fluoridation on HAP¹² and fluoride-induced bacterial adhesion on HAP surfaces.⁷

2. MATERIALS AND METHODS

2.1. Materials. Nanoscaled HAP powder (Sigma-Aldrich Chemie GmbH, Munich, Germany) was used as a raw material for the synthesis of HAP pellets. Before sintering, 10 g of the powder was dispersed and rinsed three times in 1 L of freshly demineralized water (Thermo Fisher, resistivity ~ 18.2 M Ω -cm) in order to remove any water-soluble impurities, as e.g., byproducts from the HAP synthesis such as Na⁺ or Cl⁻.¹² After filtration, the powder was dried in a drying cabinet at 110 °C for at least 15 h, followed by mincing of the clotted powder in a mortar for further preparation or analysis.

2.2. Synthesis of FAST Samples. For the FAST method, 3 g of HAP powder was filled into a carbon compression mold (diameter 22 mm) which was mounted into a FAST furnace (HP D 25 by FCT Systems). After evacuation of the setup below 1 mbar, the mold has been heated electrically by a pulsed current (pulse duration 10 ms). Up to a temperature of 700 °C, the heating was carried out with a temperature ramping of 150 °C/min. At 700 °C the mold was instantly loaded with a uniaxial force of 19 kN (resulting in a pressure of 50 MPa), and the heating rate was reduced to 10 °C/min. At the maximum temperature of 1000 °C the pressure was kept constant for 5 min, and afterward, the force was released instantly and the heating power was switched off. Down to 500 °C, the cooling rate was approximately -50 °C/min. At 500 °C, the setup was flooded with N₂. Reaching room temperature, the sample was removed from the mold. It finally featured a cylindrical shape of 22 mm in diameter and about 5 mm in height. The mass-to-volume ratio revealed a density of ~ 3.00 g/cm³, which is larger than 95% of the crystallographic density of ~ 3.156 g/cm³.¹⁹

2.3. Synthesis of PLS Samples. In the case of the PLS method, 1 g of HAP powder was filled into a 15 ton compression tool of stainless steel (MsScientific, Berlin, Germany) with a diameter of 16 mm. For compacting the powder, a compressing force of 20 kN was applied uniaxially (resulting in a pressure of ~ 100 MPa). The green body with a density of 66% of the crystallographic density was placed into a high temperature sinter furnace on a corundum ceramic disk and was sintered according to the temperature profile in Figure 1a with a heating rate of 1 °C/min, as proposed in ref 19. To reduce strain and

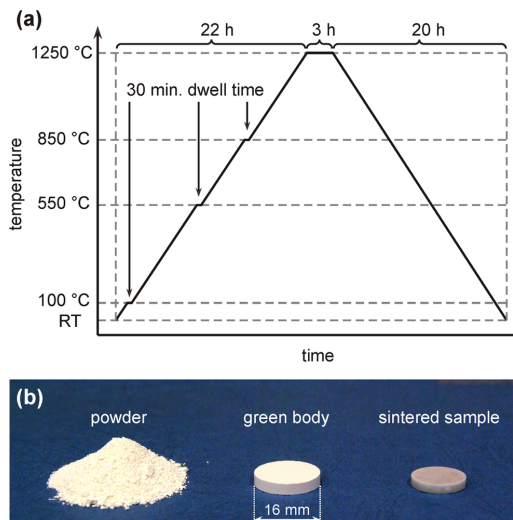


Figure 1. (a) Temperature profile used for the pressureless sintered (PLS) samples. (b) 1 g of HAP in different stages of sample preparation: powder, green body after compression, and sintered sample.

to degas the samples, heating was paused at 100 °C, 550 °C, and 850 °C for 30 min.¹⁹ The final temperature of 1250 °C was held for 3 h. Cooling was performed with -1 °C/min. The samples finally featured a density (as determined by an Archimedes balance) between 97% and 99% of the crystallographic density.¹⁹ The thickness of the disc-shaped samples was in the range of 2.0–2.5 mm (cf. Figure 1b).

After sintering, both types of samples were treated with abrasive paper (SiC, Struers, Willich, Germany) and polishing suspensions (MDAC, Struers, Willich, Germany; 1 μ m diamond polishing suspension; MSY 0-0.03, Microdiamant, Lengwil, Switzerland; 30 nm diamond polishing suspension). Since the application of the diamond suspension results in a dilute distribution of some nanodiamonds on the surface (cf. Figure S1b), a final etching step was applied by exposing the surface to a 0.01 mol/L acetate buffer solution of pH 4.5 for 10 s in order to remove the residues of the polishing suspension.

2.4. Methods. X-ray photoelectron spectroscopy (XPS) was performed with an ESCA MKII spectrometer by Vacuum Generators (base pressure $\sim 10^{-10}$ mbar) using nonmonochromatized Al K α excitation ($h\nu = 1486.6$ eV). For quantitative analysis of the stoichiometry, spectra of Ca-2p, Ca-2s, P-2p, P-2s, O-1s, and C-1s were taken at a pass energy of 20 eV in normal emission mode (i.e., emission angle = 0° with respect to the surface normal). To get the relative amount of each element, the intensities (i.e., peak areas) of the particular core levels were scaled with the photoemission cross sections by Yeh and Lindau²¹ after Shirley background subtraction.²² For Ca and P, the elemental contributions were averaged using the 2p and 2s peaks.

For atomic force microscopy (AFM) a Bruker Bioscope Catalyst (Santa Barbara, CA) was used with Olympus OMCL-AC160TS tips (Tokyo, Japan) in tapping mode. The AFM probed root-mean-square (RMS) roughness of a surface is given by

$$\sigma_{\text{RMS}} = \sqrt{\frac{\sum (z_i - \bar{z})^2}{n}}$$

with z_i , \bar{z} , and n describing the height coordinates of a particular pixel, the mean height, and the number of pixels, respectively.

Prior to the calculation of the RMS roughness, plane fit and flattening procedures were applied to the AFM images. In case of the

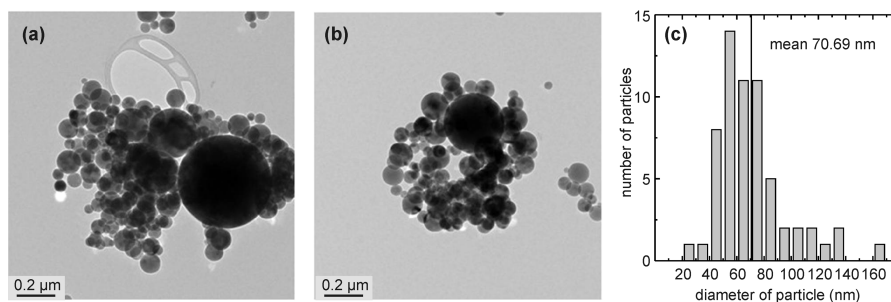


Figure 2. (a, b) TEM micrographs of washed HAP powder dispersed in propanol. (c) Distribution of particle diameters as extracted from TEM data (as based on the analysis of 61 particles).

plane fit, a first-order polynomial equation was used to fit the scanned surface and remove tilt in both x and y directions:

$$z_{\text{fit}} = a + bx + cy$$

Flattening (zeroth order) was used to center data along each line and thereby remove offsets between scan lines.

Scanning electron microscopy (SEM) was performed with a JSM-7000 F by JEOL Ltd., Tokyo, Japan, using 20 keV electrons. For electron backscattering diffraction (EBSD), the same setup was operated with an electron acceleration voltage of 15 kV and a Digiview 3 detector by EDAX Inc., Mahwah, NJ. The identification of different grains was achieved by comparing the diffraction patterns with the Kikuchi patterns²³ from the database provided by the manufacturer. For transmission electron microscopy, a JEM 2011 by JEOL Ltd., Tokyo, Japan, working with 200 keV electrons was used.

X-ray diffraction (XRD) was carried out using an X'Pert Pro diffractometer with PIXcel 1D detector by PANalytical, Almelo, Netherlands, with $\text{Cu } K\alpha_{1/2}$ radiation ($\lambda = 0.154 \text{ nm}$).

Microindentation tests were done by a Struers DuraScan facility according to HV0.1 with a 60× objective. Nine indents were performed for each sample and finally averaged.

3. RESULTS AND DISCUSSION

3.1. Powder Characterization. To probe the particle size distribution, HAP powder was dispersed in propanol and placed on a TEM grid. After evaporation of the solvent, the grid was mounted into a TEM. Figure 2 displays the typical size distribution of HAP particles after dispersion in propanol with the size of the clusters ranging from some hundreds of nanometers to about 1 μm. The diameters of the particles range from some tens to some hundreds of nanometers with a mean value of about 70 nm.

To reveal the chemical composition, small amounts of the powder were pressed to a pellet and probed by XPS.

Table 1 compares the stoichiometry of HAP (i.e., $\text{Ca}_{10}(\text{PO}_4)_6(\text{OH})_2 \rightarrow \text{Ca:P:O} = 5:3:13$) with the composition of washed HAP powder. The deviation between the nominal HAP composition and the XPS derived HAP stoichiometry is similar to that observed in other studies.^{24–26} The observation

Table 1. Relative Amount of Elements for Washed HAP Powder^a

	Ca	P	O	C	Ca:P	Ca:O
washed HAP	4.6	3	14.0	3.2	1.52	0.33
nominal formula unit	5	3	13	0	1.67	0.38

^aFor better comparison values are scaled to the nominal phosphorus content in the HAP sum formula.

of carbon (as a ubiquitous impurity for *ex situ* prepared samples) as well as the excess of oxygen can be simply related to the presence of adsorbates. Such impurities have a strong impact on the measurement due to the surface sensitivity of XPS and the nanoscale (i.e., surface dominated) structure of the powder.

Concerning the crystal structure of the powder, the XRD data in Figure 3 are in good agreement with the diffraction

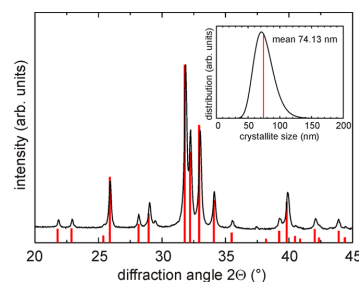


Figure 3. XRD pattern of washed HAP powder. The red bars denote the pattern of the $P6_3/m$ space group for stoichiometric HAP according to the PDF card 98-004-7182. The additional peaks at diffraction angles of $\sim 29^\circ$ and $\sim 37^\circ$ probably result from small amounts of impurities such as CaCO_3 and CaO . The inset shows the crystallite size distribution obtained from a Warren–Averbach analysis resulting in a mean value of 74.13 nm.

pattern of the $P6_3/m$ space group²⁷ for stoichiometric HAP (PDF card 98-004-7182). Additional peaks at diffraction angles of about 29° and 37° can be assigned to small amounts of impurities such as calcite, CaCO_3 , or quicklime, CaO . Together, chemical composition and structural data imply that the HAP powder represents a nearly phase-pure raw material. The crystallite size distribution was determined by a Warren–Averbach analysis. Using a self-developed software package,^{28,29} the measured data were corrected for instrumental resolution. The correction was done by deconvolution in Fourier space. Assuming a log-normal distribution^{30,31} the Fourier coefficients were used for the calculation of the corresponding parameters μ and σ , representing the mean value and the asymmetry, respectively. The resulting crystallite size distribution (Figure 2c, inset) with a μ value of 74.13 nm and a σ value of 1.23 is in accordance with the values obtained from the TEM data in Figure 2c (for details, see Table S1 in the Supporting Information).

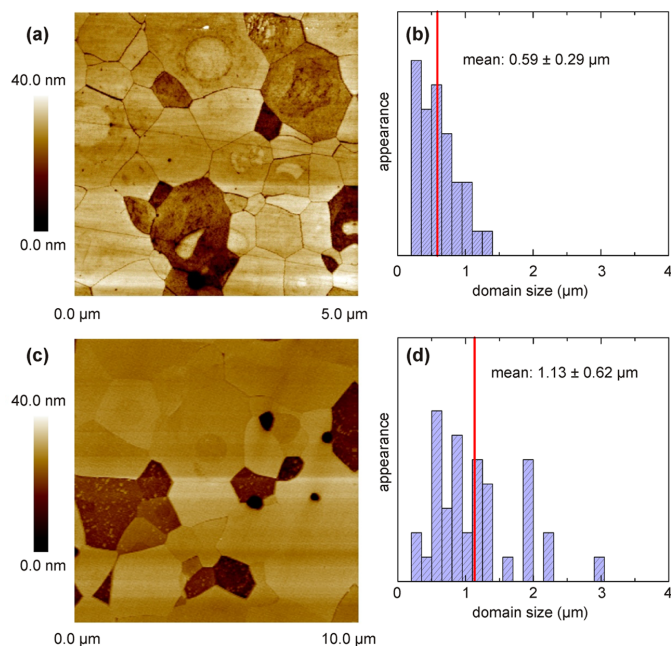


Figure 4. Atomic force microscopy on HAP pellets after polishing and final etching. (a) Topography of a $5 \times 5 \mu\text{m}^2$ surface area of a FAST sample. (b) Distribution of domain sizes for FAST sample, as based on the analysis of 36 domains from (a). (c) Topography of a $10 \times 10 \mu\text{m}^2$ surface area of a PLS sample. (d) Distribution of domain sizes for PLS sample as based on the analysis of 39 domains from (c). For analysis of domain sizes, domain perimeters were marked by closed polygons, and the areas were related to the area of the whole AFM image.

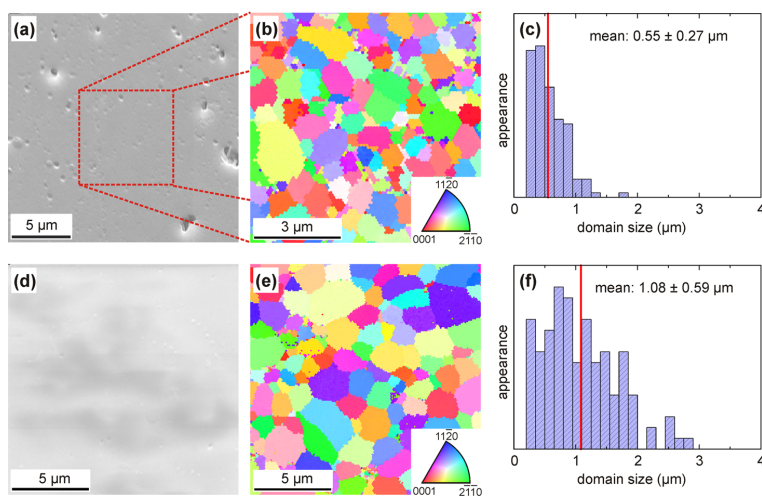


Figure 5. (a) SEM micrograph of a FAST sintered sample after the final polishing step using 30 nm diamond suspension followed by etching. (b) EBSD map taken from the marked area (red box) with colors representing crystallographic orientations (cf. inset). (c) Distribution of domain sizes taken from the EBSD map (as based on ~ 130 grains with size larger than 200 nm to exclude single pixels). (d–f) Same experiments on the surface of a pressureless sintered sample. For Image-Quality maps of the EBSD data, cf. Figure S2.

3.2. Characterization of Sintered Samples. Figure 4 compares the AFM-probed surface topography of a FAST sample and a PLS sample after polishing and final etching. In both cases, distinct domains exhibiting different heights could be identified. This kind of topography results from the final

etching of the polished samples since domains of very different heights are not observed before the etching procedure (see Figure S1 in the Supporting Information). When restricting the RMS-probing area to $\sim 1 \times 1 \mu\text{m}^2$, the roughness strongly depends on the particular domains. For deep grains (dark areas

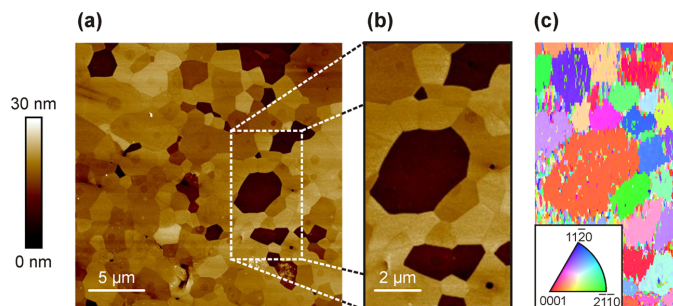


Figure 6. (a) AFM picture of a PLS sintered sample with domain distribution similar to Figure 4. (b) Selected area for EBSD mapping. (c) EBSD map of selected area. Because of a drift of the sample during the EBSD scan, the EBSD map had to be slightly stretched to fit the selected AFM area.

in Figure 4) typical RMS values range around 1 nm, whereas for high grains (i.e., bright areas in Figure 4) the RMS values clearly drop to the angstrom range. For both samples, only a small amount of pores is visible in accordance with the high density of both samples. The most prominent difference between the FAST and PLS prepared samples concerns the size distribution of the domains. For the FAST sintered sample, the average domain size is $0.59 \pm 0.29 \mu\text{m}$ while it is nearly twice as large for the PLS sintered sample, i.e., $1.13 \pm 0.62 \mu\text{m}$ (these values represent the square roots of the average domain areas to have characteristic lengths for comparison with the average particle diameter of the powder).

In Figure 5, SEM micrographs, EBSD maps, and the distribution of grain sizes are compared for FAST and PLS prepared samples. Apart from pores also seen in AFM, a homogeneous surface is found in SEM images (Figures 5a and 5d). Only with the help of EBSD, the domains found in AFM (Figure 4) can be revealed. The EBSD technique allows, however, to identify these domains as individual single-crystalline grains that are terminated by different crystal planes.

In terms of crystallographic orientation, no texture (i.e., preferred orientation) can be observed in the EBSD maps (Figures 5b and 5e). The orientation of the grains is distributed nearly randomly; i.e., there is no distinct impact of mechanical anisotropy due to the uniaxial compression. With respect to the grain size, the FAST sample provides the most homogeneous distribution with an average grain size of $0.55 \pm 0.27 \mu\text{m}$ (cf. AFM data $0.59 \pm 0.29 \mu\text{m}$). For the PLS sample, the average grain size amounts to $1.08 \pm 0.59 \mu\text{m}$ (cf. AFM data $1.13 \pm 0.62 \mu\text{m}$); i.e., the average grain area of the PLS sample is nearly 4 times as large as in the case of the FAST sample (at least for the preparation parameters used here).

Although the AFM data in Figure 4 and the EBSD data in Figure 5 were taken from different samples, the distributions of AFM-probed domain sizes (Figures 4b and 4d) compare well with the distributions of the EBSD-probed domain sizes (Figures 5c and 5f). Therefore, domains of constant height seem to represent single-crystalline grains. To prove this assumption unambiguously, AFM data are compared with EBSD data for the very same surface area, as depicted in Figure 6. The direct comparison of the topography in Figure 6b with the scattering distribution in Figure 6c gives evidence that the height distribution in AFM strongly matches with the crystallographic orientation in EBSD. Since the etching rate for a crystallite is affected by the crystallographic orientation of its surface,³² the height of each domain is a direct measure for

the etching rate of different crystallite's facets (note that the topographic characteristics in Figures 4 and 6 are not observed for samples without the final etching procedure; cf. Figure S1). The domains with strongest etching (dark areas in Figure 6b) correspond to the facets close to the (0001) basal plane (reddish coloring in Figure 6c; cf. also inset).

The chemical compositions of the samples as probed by XPS are compared in Table 2. At first sight, the composition of the

Table 2. Relative Amounts of Elements in Sintered HAP Samples, As Probed on the Initial Surface and after Ablation of Several nanometers by Ar Ion Etching^a

		Ca	P	O	C	Ca:P	Ca:O
PLS sample	as sintered	4.0	3	12.8	2.0	1.33	0.31
	after Ar ion etching	4.6	3	11.4	0.8	1.70	0.44
FAST sample	as sintered	4.1	3	13.2	9.2	1.36	0.31
	after Ar ion etching	4.5	3	12.1	2.1	1.50	0.37
formula unit		5	3	13	0	1.67	0.38

^aFor better comparison values are scaled to the nominal phosphorus content in the HAP sum formula.

samples seems to deviate from the nominal composition of the HAP sum formula. Especially in the case of the as-sintered samples, there is a strong depletion of Ca resulting in a Ca:P ratio that meets only 82% of the nominal value. This is probably caused by element-specific preferred wet chemical etching in acetate buffer solution performed in the last preparation step of the samples. However, after ablation of several nanometers by Ar ion etching, the Ca:P ratio approaches the nominal value (at least in the range of 10% error which is not unusual in XPS).

According to the increase in average particle size upon sintering as observed by the TEM data in Figure 2 (average particle size ~ 70 nm) and by the EBSD data in Figure 5 (average domain size ~ 550 – 1100 nm), the XRD data in Figure 7 display a strong decrease in peak widths. More importantly, no contributions from crystalline material other than HAP and the initial impurities (e.g., CaCO_3 and CaO) can be observed, indicating that there is no distinct transformation of material during the sintering processes. In contrast to the XRD data analysis of the HAP raw powder by a Warren–Averbach evaluation, a corresponding analysis of the sintered HAP samples was not possible because of a too small difference in

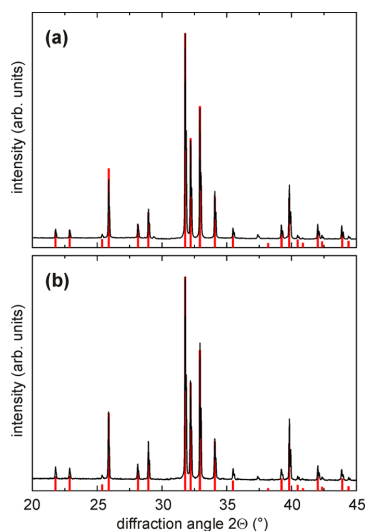


Figure 7. Typical XRD patterns of (a) a FAST prepared HAP sample and (b) of a PLS prepared HAP sample. The red bars denote the pattern of the $P6_3/m$ space group for stoichiometric HAP according to the PDF card 98-004-7182.

peak width between the measured data and the resolution of the instrument (0.04°). For this reason, only the crystallite size and the microstrain content were determined by nonprofile evaluating methods, i.e., Scherrer³³ and Williamson Hall analysis.³⁴ The results confirm the observations from the AFM and EBSD data, namely, a larger mean crystallite size for the PLS prepared sample (for details, see Table S1).

Microindentation experiments reveal also no distinct differences for pellets from the different synthesis routes, as displayed in Figure 8. The Vickers hardness of the FAST samples is about 660 HV0.1, and the values for the PLS samples are nearly the same, i.e., 670–680 HV0.1. These values are, however, nearly twice as large as the values obtained for

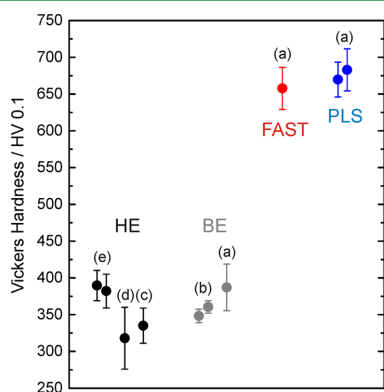


Figure 8. Comparison of Vickers hardness of FAST and PLS prepared HAP samples with hardness of bovine enamel (BE) and human enamel (HE): (a) this study, (b) ref 35, (c) ref 36, (d) ref 37, and (e) ref 38.

samples from bovine and human enamel. The reason is the very high density of the sintered HAP samples which contain no organic matrix between the grains.

3.3. Outlook. To illustrate the potential for the utility of such HAP samples, the adsorption of bovine serum albumin (BSA) proteins is demonstrated on the surface of a PLS prepared HAP sample in Figure 9. Despite the small size of the

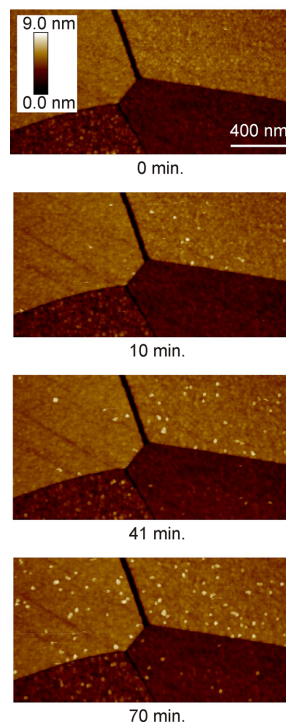


Figure 9. Different states of BSA protein adsorption on the surface of a PLS prepared HAP sample.

proteins in the range of 200–300 nm³, individual specimens (white spots) can be detected due to the low surface roughness of the particular HAP grains. It is also obvious that the time dependence of protein adsorption is different on each grain giving evidence that the adsorption rate probably depends either on the texture of an individual grain or on its roughness. Since crystallographic orientation and residual roughness are, however, correlated according to the AFM data in Figure 4, it is not possible at this state to reveal the real origin of varying protein adsorption rates. Such issues will be discussed in detail in our future works. Furthermore, we will adopt the hydroxyapatite samples to investigate salivary protein adsorption under *in vivo* conditions in the oral cavity, thereby focusing on the effect of pure hydroxyapatite and excluding any influence of the individual enamel's properties on the adsorption process.

4. CONCLUSIONS

We presented two types of sintering techniques for the synthesis of HAP samples. Both procedures provide HAP samples with very similar properties in terms of surface

roughness, chemical composition, crystal structure, density, and microhardness. The most prominent difference (at least for the preparation parameters used here) concerns the average grain size. The FAST synthesis provides samples with the smallest average grain size and the smallest distribution in grain size; i.e., it results in the most homogeneous samples. For the PLS technique, the average grain area is nearly 4 times larger. At first sight, the less complex PLS technique seems therefore the preferred method. However, PLS samples are more brittle. This issue was not studied quantitatively, but our experience shows that this drawback holds only in case that large shear forces are applied, as e.g. during machine polishing. In usual sample handling, such as sample transfer or sample mounting, it plays a minor role.

On a macroscopic scale, i.e., for areas extending several tens or hundreds of μm^2 , the surface roughness of both kinds of sintered HAP samples cannot compete with the roughness of current model systems such as silicon wafers. When restricting the areas to the range of a few μm^2 , however, the roughness of individual grains is in the sub-nanometer range. Therefore, on this μm^2 scale, the sintered HAP samples can take the role of a new real-life model system, especially in such cases where the interaction between solids and very small bioparticles, such as proteins, are of particular interest.

■ ASSOCIATED CONTENT

Supporting Information

The Supporting Information is available free of charge on the ACS Publications website at DOI: 10.1021/acsami.6b10089.

Figures S1 and S2; Table S1 (PDF)

■ AUTHOR INFORMATION

Corresponding Authors

*E-mail: f.mueller@mx.uni-saarland.de (F.M.).

*E-mail: k.jacobs@physik.uni-saarland.de (K.J.).

Author Contributions

C.Z. and T.F. contributed equally to this work.

Notes

The authors declare no competing financial interest.

■ ACKNOWLEDGMENTS

T.F., H.H., N.T., C.S., M.H., F.M., and K.J. acknowledge support from the German Research Foundation (DFG) in the framework of the Collaborative Research Centre SFB 1027 "Physical modeling of nonequilibrium processes in biological systems". C.Z. and S.G. were supported by the DFG within the graduate school GRK 1276 and Saarland University and Saarland Ministry of Economy. The authors thank Manuel Grewer, Experimental Physics, Saarland University, for additional XRD measurements and Simon Staudacher, Department of Materials Science, Saarland University, for assistance in microindentation experiments. Stefan Fünfschilling and Deniz Kahraman, Institute of Applied Materials, Ceramics in Mechanical Engineering, Karlsruhe Institute of Technology, are acknowledged for support in preparation of the FAST samples.

■ REFERENCES

- (1) Kasemo, B. Biological surface science. *Surf. Sci.* **2002**, *500*, 656–677.
- (2) Dufrene, Y. F. Using nanotechniques to explore microbial surfaces. *Nat. Rev. Microbiol.* **2004**, *2*, 451–460.

- (3) Wilson, C. J.; Clegg, R. E.; Leavesley, D. I.; Percy, M. J. Mediation of biomaterial-cell interactions by adsorbed proteins: A review. *Tissue Eng.* **2005**, *11*, 1–18.

- (4) Norde, W. Adsorption of proteins from solution at the solid-liquid interface. *Adv. Colloid Interface Sci.* **1986**, *25*, 267–340.

- (5) Schmitt, Y.; Hähl, H.; Gilow, C.; Mantz, H.; Jacobs, K.; Leidinger, O.; Bellion, M.; Santen, L. Structural evolution of protein-biofilms: Simulations and experiments. *Biomicrofluidics* **2010**, *4*, 032201.

- (6) Loskill, P.; Hähl, H.; Thewes, N.; Kreis, C. T.; Bischoff, M.; Herrmann, M.; Jacobs, K. Influence of the subsurface composition of a material on the adhesion of staphylococci. *Langmuir* **2012**, *28*, 7242–7248.

- (7) Loskill, P.; Zeitz, C.; Grandthyll, S.; Thewes, N.; Müller, F.; Bischoff, M.; Herrmann, M.; Jacobs, K. Reduced adhesion of oral bacteria on hydroxyapatite by fluoride treatment. *Langmuir* **2013**, *29*, 5528–5533.

- (8) Beaussart, A.; El-Kirat-Chatel, S.; Herman, P.; Alsteens, D.; Mahillon, J.; Hols, P.; Dufrene, Y. F. Single-Cell Force Spectroscopy of Probiotic Bacteria. *Biophys. J.* **2013**, *104*, 1886–1892.

- (9) Van der Mei, H. C.; Rustema-Abbing, M.; de Vries, J.; Busscher, H. J. Bond Strengthening in Oral Bacterial Adhesion to Salivary Conditioning Films. *Appl. Environ. Microbiol.* **2008**, *74*, 5511–5515.

- (10) Rabe, M.; Verdes, D.; Seeger, S. Understanding protein adsorption phenomena at solid surfaces. *Adv. Colloid Interface Sci.* **2011**, *162*, 87–106.

- (11) Hähl, H.; Evers, F.; Grandthyll, S.; Paulus, M.; Sternemann, C.; Loskill, P.; Lessel, M.; Hueseken, A.; Brenner, T.; Tolan, M.; Jacobs, K. Subsurface Influence on the Structure of Protein Adsorbates as Revealed by in Situ X-ray Reflectivity. *Langmuir* **2012**, *28*, 7747–7756.

- (12) Müller, F.; Zeitz, C.; Mantz, H.; Ehses, K.-H.; Soldera, F.; Schmauch, J.; Hannig, M.; Hüfner, S.; Jacobs, K. Elemental Depth Profiling of Fluoridated Hydroxyapatite: Saving Your Dentition by the Skin of Your Teeth? *Langmuir* **2010**, *26*, 18750–18759.

- (13) Lee, H.; Scherer, N. F.; Messersmith, P. B. Single-molecule Mechanics of Mussel Adhesion. *Proc. Natl. Acad. Sci. U. S. A.* **2006**, *103*, 12999–13003.

- (14) Schroeder, H. E. *Orale Strukturbiologie: Entwicklungsgeschichte, Struktur und Funktion normaler Hart- und Weichgewebe der Mundhöhle und des Kiefergelenks*, 5th ed.; Thieme Georg Verlag: Stuttgart, 2000.

- (15) Hannig, M.; Hannig, C. Nanomaterials in preventive dentistry. *Nat. Nanotechnol.* **2010**, *5*, 565–568.

- (16) Weatherell, J.; Robinson, C.; Hallsworth, A. Variations in the Chemical Composition of Human Enamel. *J. Dent. Res.* **1974**, *53*, 180–192.

- (17) Barros, J.; Grenho, L.; Manuel, C. M.; Ferreira, C.; Melo, L.; Nunes, O. C.; Monteiro, F. J.; Ferraz, M. P. Influence of Nanohydroxyapatite surface properties on *Staphylococcus Epidermidis* Biofilm Formation. *J. Biomater. Appl.* **2014**, *28*, 1325–1335.

- (18) Barros, J.; Grenho, L.; Fernandes, M. H.; Manuel, C. M.; Melo, L. F.; Nunes, O. C.; Monteiro, F. J.; Ferraz, M. P. Anti-sessile Bacterial and Cytocompatibility Properties of CHX-loaded Nanohydroxyapatite. *Colloids Surf., B* **2015**, *130*, 305–314.

- (19) Prokopiev, O.; Sevostianov, I.; Genin, J.; McGee, S. M.; Woodward, C. Microstructure and elastic properties of sintered hydroxyapatite. *Int. J. Fract.* **2004**, *130*, L183–L190.

- (20) Ramesh, S.; Aw, K. L.; Tolouei, R.; Amiriyani, M.; Tan, C. Y.; Hamdi, M.; Purbolaksono, J.; Hassan, M. A.; Teng, W. D. Sintering properties of hydroxyapatite powders prepared using different methods. *Ceram. Int.* **2013**, *39*, 111–119.

- (21) Yeh, J. J.; Lindau, I. Atomic subshell photoionization cross sections and asymmetry parameters: $1 \leq Z \leq 103$. *At. Data Nucl. Data Tables* **1985**, *32*, 1–155.

- (22) Shirley, D. High-Resolution X-Ray Photoemission Spectrum of the Valence Bands of Gold. *Phys. Rev. B* **1972**, *5*, 4709–4714.

- (23) Nishikawa, S.; Kikuchi, S. Diffraction of Cathode Rays by Mica. *Nature* **1928**, *121*, 1019–1020.

- (24) Sternitzke, V.; Kaegi, R.; Audinot, J.-N.; Lewin, E.; Hering, J. G.; Johnson, C. A. Uptake of Fluoride from Aqueous Solution on Nano-

Sized Hydroxyapatite: Examination of a Fluoridated Surface Layer. *Environ. Sci. Technol.* **2012**, *46*, 802–809.

(25) Sternitzke, V.; Janousch, M.; Heeb, M. B.; Hering, J. G.; Johnson, C. A. Strontium hydroxyapatite and strontium carbonate as templates for the precipitation of calcium-phosphates in the absence and presence of fluoride. *J. Cryst. Growth* **2014**, *396*, 71–78.

(26) Gerth, H. U. V.; Dammaschke, T.; Schäfer, E.; Züchner, H. A three layer structure model of fluoridated enamel containing CaF₂, Ca(OH)₂ and FAp. *Dent. Mater.* **2008**, *23*, 1521–1528.

(27) Reyes-Gasga, J.; Martínez-Pinero, E. L.; Brès, É.F. Crystallographic structure of human tooth enamel by electron microscopy and X-ray diffraction: hexagonal or monoclinic. *J. Microsc.* **2012**, *248*, 102–109.

(28) Natter, H.; Schmelzer, M.; Löffler, M.-S.; Krill, C. E.; Fitch, A.; Hempelmann, R. Grain-Growth Kinetics of Nanocrystalline Iron Studied in Situ by Synchrotron Real-Time X-ray Diffraction. *J. Phys. Chem. B* **2000**, *104*, 2467–2476.

(29) Natter, H.; Hempelmann, R. Nanocrystalline copper by pulsed electrodeposition: The effects of organic additives, bath temperature, and pH. *J. Phys. Chem.* **1996**, *100*, 19525–19532.

(30) Krill, C. E.; Helfen, L.; Michels, D.; Natter, H.; Fitch, A.; Masson, O.; Birringer, R. Size-dependent grain-growth kinetics observed in nanocrystalline Fe. *Phys. Rev. Lett.* **2001**, *86*, 842–845.

(31) Krill, C. E.; Birringer, R. Estimating grain-size distributions in nanocrystalline materials from X-ray diffraction profile analysis. *Philos. Mag. A* **1998**, *77*, 621–640.

(32) Sato, K.; Shikida, M.; Yamashiro, T.; Tsunekawa, M.; Ito, S. Roughening of Single-Crystal Silicon Surface Etched by KOH Water Solution. *Sens. Actuators, A* **1999**, *73*, 122–130.

(33) Scherrer, P. Bestimmung der Größe und der inneren Struktur von Kolloidteilchen mittels Röntgenstrahlung. *Göttinger Nachrichten* **1918**, *2*, 98–100.

(34) Williamson, G. K.; Hall, W. H. X-Ray Line Broadening from Filed Aluminium and Wolfram. *Acta Metall.* **1953**, *1*, 22–31.

(35) Mundra, S.; Mohan, V.; Gwyer, J.; Young, N.; Franklin, S. E.; Gerhardt, L.-C. Hardness, friction and wear studies on hydrogen peroxide treated bovine teeth. *Tribol. Int.* **2015**, *89*, 109–118.

(36) Aydin, B.; Pamir, T.; Baltacı, A.; Orman, M. N.; Turk, T. Effect of storage solutions on microhardness of crown enamel and dentin. *Eur. J. Dent.* **2015**, *9*, 262–266.

(37) Chuenarrom, C.; Benjakul, P.; Daosodsai, P. Effect of indentation load and time on Knoop and Vickers microhardness tests for enamel and dentin. *Mater. Res.* **2009**, *12*, 473–476.

(38) Akal, N.; Over, H.; Olmez, A.; Bodur, H. Effects of carbamide peroxide containing bleaching agents on the morphology and subsurface hardness of enamel. *J. Clin. Pediatr. Dent.* **2001**, *25*, 293–296.

SUPPORTING INFORMATION

for

Synthesis of hydroxyapatite substrates: Bridging the gap between model surfaces and enamel

Christian Zeitz,¹ Thomas Faidt,¹ Samuel Grandthyll,¹ Hendrik Hähl,¹ Nicolas Thewes,¹ Christian Spengler,¹ Jörg Schmauch,¹ Michael Johannes Deckarm,¹ Carsten Gachot,² Harald Natter,³ Matthias Hannig,⁴ Frank Müller,^{*1} Karin Jacobs^{*1}

¹ Experimental Physics, Saarland University, 66123 Saarbrücken, Germany,

² Department of Materials Science, Saarland University, 66123 Saarbrücken, Germany,

³ Physical Chemistry, Saarland University, 66123 Saarbrücken, Germany,

⁴ Clinic of Operative Dentistry, Periodontology and Preventive Dentistry, Saarland University, 66421 Homburg, Germany

* Corresponding authors. *Email addresses:* f.mueller@mx.uni-saarland.de (F. Müller), k.jacobs@physik.uni-saarland.de (K. Jacobs)

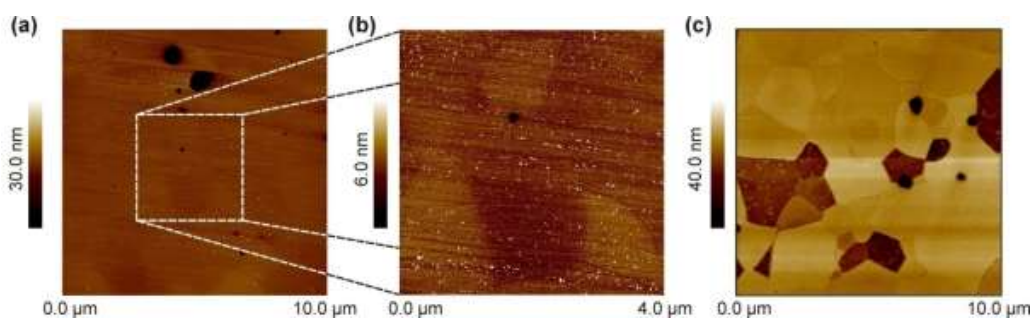


Figure S1: AFM data on PLS prepared samples (a) after final polishing with 30 nm diamond suspension and subsequent ultrasonic bathing in water for 5 minutes. (b) Enlarged image of the same area with white dots representing residues from the diamond suspension. The size of the white dots ranges from 25 nm to 50 nm in accordance with the nominal size of 30 nm for the nano-diamonds. (c) Similar data from another sample after additional etching in a sodium acetate/acetic acid buffer at pH 4.5 for 10 s. Compared to the not etched samples, the difference in domain heights (i.e. without pores and polishing residues) has increased by more than one order of magnitude.

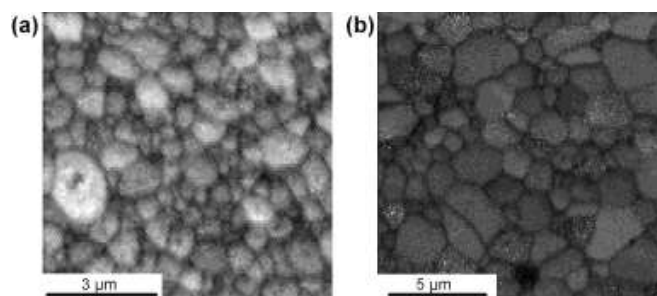


Figure S2: Grey scale image quality maps of the EBSD data (a) from the FAST sample in Figure 5b and (b) from the PLS sample in Figure 5e. Irrespective of an absolute quality scaling, diffraction appears homogeneous throughout the individual domains.

	HAP powder	FAST sample	PLS sample
$D_{\text{volume}}^{(a)}$	61 nm (002) 56 nm (004)	232 nm (002) 222 nm (004)	670 nm (002) 598 nm (004)
$D_{\text{volume}}^{(b)}$	79 nm	256 nm	477 nm
$D_{\text{volume}}^{(c)}$	86 nm	–	–
$\langle \epsilon^2 \rangle^{(b)}$	0.22 %	0.009 %	0.012 %
$\langle \epsilon^2 \rangle^{(c)}$	0.30 %	n.a.	n.a.
$\mu^{(c)}$	74.13 nm	n.a.	n.a.
$\sigma^{(c)}$	1.23	n.a.	n.a.

Table T1: Volume-weighted average crystallite size D_{volume} , strain $\langle \epsilon^2 \rangle$, mean crystallite size μ and asymmetry parameter σ as obtained from analysis of the XRD data in Fig. 3 and Fig. 7 using (a) the Scherrer method, (b) the Williamson-Hall method and (c) a modified Warren-Averbach method. The values in parentheses in the first row denote the reflections used for analysis.

II: Time Dependence of Fluoride Uptake in Hydroxyapatite

Authors: **T. Faidt**,¹ C. Zeitz,¹ S. Grandthyll,¹ M. Hans,² M. Hannig,³ K. Jacobs,¹ and F. Müller¹

¹ Experimental Physics, Saarland University, 66123 Saarbrücken, Germany.

² Functional Materials, Saarland University, 66123 Saarbrücken, Germany.

³ Clinic of Operative Dentistry, Periodontology and Preventive Dentistry, Saarland University, 66421 Homburg, Germany.

Reprinted with permission from *ACS Biomater. Sci. Eng.* 3 (2017), pp. 1822–1826.

Copyright 2017 American Chemical Society.

<https://doi.org/10.1021/acsbomaterials.6b00782>

Author contributions:

T. Faidt produced hydroxyapatite samples, performed fluoridation experiments and XPS measurements, analyzed XPS data and wrote the manuscript. **C. Zeitz** assisted in analyzing measurement data and wrote the manuscript. **S. Grandthyll** performed XPS measurements and analyzed XPS data. **M. Hans** performed white light interferometry measurements. **M. Hannig** assisted in writing the manuscript. **K. Jacobs** directed experimental work and wrote the manuscript. **F. Müller** directed experimental work, performed XPS measurements, analyzed XPS data and wrote the manuscript.

Abstract – Fluoridation of enamel is believed to provide an effective tool to protect teeth from caries, but there is still little information on the time scale of fluoride uptake. In this study, highly compressed pellets of hydroxyapatite are used as first-order model systems to approximate the mineral component of natural enamel for investigations on the time-dependence of fluoride uptake. We found that both the overall amount of fluoride as well as the mean thickness of the fluoridated surface layer cannot be extended to any values just by increasing the application time of a fluoride containing agent. Instead, both parameters start to become constant on a time scale of about 3 min. The present results as obtained on a synthetic model “tooth” show that the time scale to provide the maximum amount of fluoride possible is of the same order of magnitude as that in usual daily practice in dental care when applying toothpastes or mouth rinses.

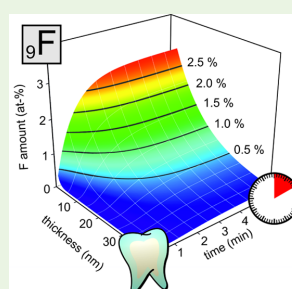
Time Dependence of Fluoride Uptake in Hydroxyapatite

Thomas Faidt,[†] Christian Zeitz,[†] Samuel Grandthyll,[†] Michael Hans,[‡] Matthias Hannig,[§] Karin Jacobs,[†] and Frank Müller^{*,†}[†]Experimental Physics, Faculty of Natural Sciences and Technology, Saarland University, 66123 Saarbrücken, Germany[‡]Functional Materials, Faculty of Natural Sciences and Technology, Saarland University, 66123 Saarbrücken, Germany[§]Clinic of Operative Dentistry, Periodontology and Preventive Dentistry, Faculty of Medicine-Clinical Medicine, Saarland University Hospital, 66421 Homburg, Germany

Supporting Information

ABSTRACT: Fluoridation of enamel is believed to provide an effective tool to protect teeth from caries, but there is still little information on the time scale of fluoride uptake. In this study, highly compressed pellets of hydroxyapatite are used as first-order model systems to approximate the mineral component of natural enamel for investigations on the time-dependence of fluoride uptake. We found that both the overall amount of fluoride as well as the mean thickness of the fluoridated surface layer cannot be extended to any values just by increasing the application time of a fluoride containing agent. Instead, both parameters start to become constant on a time scale of about 3 min. The present results as obtained on a synthetic model “tooth” show that the time scale to provide the maximum amount of fluoride possible is of the same order of magnitude as that in usual daily practice in dental care when applying toothpastes or mouth rinses.

KEYWORDS: fluoridation, hydroxyapatite, elemental depth profiling, X-ray photoelectron spectroscopy (XPS)



INTRODUCTION

In the pre World War II era, i.e., at the dawn of our modern life when cars, airplanes, television, and even computers were either established or at least emerging technologies, dental caries was still “the most widespread disease of civilized communities, affecting well over 90% of their population”.¹ Up to the 1930s, the impact of fluoride on oral health was investigated mainly with respect to fluorosis, a dental disease that is manifested by mottled and pitted teeth, as caused by an overdosage of fluoride during tooth development. Within the framework of such investigations, Black and McKay reported in 1916 on first indications that, with respect to the abundance of caries, mottled teeth “compare favorably with those of other communities where endemic mottled enamel is unknown”.² This observation also reflects the empirical finding by Masaki and Mumura who concluded in 1931 from their study on mottled teeth in the southwest of Japan that “the percentage of dental caries is comparatively small among those who suffer this abnormality”.³ Initially charged with investigating the relationship between the concentration of fluoride in the drinking water and the appearance of fluorosis, H. T. Dean considered these previous studies with regard to the multiple aspects of fluoride concentration, appearance of fluorosis, and caries prevalence.⁴ In 1942, he and his co-workers finally concluded that there is “a general inverse correlation between the fluoride concentrations of the public water supplies ... and the amount of dental caries”.⁵ Soon afterward, these findings found their way into public health care when some countries decided to provide fluoride via the fluoridation of drinking water. In other

countries, emphasis was put on the drawbacks of this policy, such as legal or bioethical issues in terms of compulsory mass medication⁶ or the medical issue of neurotoxicity and of skeletal fluorosis.⁷ However, in today’s every-day life, Dean’s findings can be applied by each individual via the use of fluoride-containing oral care products such as mouth rinses or tooth pastes, a strategy where fluoride is provided directly to the tooth’s surface.

Concerning the mechanisms of fluoride-induced caries prevention, conventional theories are based on the phenomenon of increased acid resistance as caused by a chemical modification of the tooth.⁸ Enamel is based on a calcium phosphate compound, namely, hydroxyapatite (HAp), i.e., $\text{Ca}_{10}(\text{PO}_4)_6(\text{OH})_2$, with the PO_4^{3-} and OH^- partially substituted by carbonate, CO_3^{2-} , in the so-called bio apatite.⁹ Upon fluoridation in the nearly pH-neutral range, (bio-)HAp is covered by a film of the isostructural fluoroapatite (FAP), i.e., $\text{Ca}_{10}(\text{PO}_4)_6\text{F}_2$, with increased resistance to acids. For HAp, demineralization starts at about pH 5.5, while for FAP, the pH value drops to about 4.6.¹⁰ However, the pH values for demineralization must not be regarded as constant values. According to a study by C. Dawes, the pH range for dissolving enamel strongly depends on, e.g., the concentration of calcium and phosphate in the oral environment.¹¹

Received: December 14, 2016

Accepted: June 2, 2017

Published: June 2, 2017

On the basis of photoemission studies on bovine or human enamel, it was hitherto believed that fluoridation affects the enamel up to microscopic depths, i.e., depending on parameters such as application time, pH value, temperature, and F^- concentration, the thickness of FAp layers ranges from several tens of nanometers to several microns.^{12–15} However, in 2010, experiments on synthetic HAp samples, as representing a macroscopic counterpart of a single grain from enamel, revealed that the thickness of the FAp layer is just in the range of about 10 nm.¹⁶ This experimental finding is supported by former molecular dynamic simulations predicting that “the fluoride is not expected to penetrate deeply into the apatite material”.¹⁷ In any case, FAp layers in the range of only a few nanometers may question the idea of caries prophylaxis just by building an ultrathin acid-resistant firewall.

In 2013, the results of new studies concerning the changes of adhesion forces between oral bacteria and HAp surfaces put the mechanism of caries prophylaxis in a new light. Loskill et al. compared the snap-off forces of AFM cantilevers covered by bacteria before and after fluoridation of HAp.¹⁸ It was found that after fluoridation the adhesion force is reduced by a factor of 2, independent of the bacterial species (i.e., *Streptococcus mutans*, *Streptococcus oralis*, and *Staphylococcus carnosus*). The authors concluded with the hypothesis that decreasing bacterial adhesion forces may be another reason for caries prevention by fluoride,¹⁸ meaning that a “bacteria-mediated acid attack”¹⁹ can hardly be mediated when less bacteria adhere on the enamel’s surface. These *in vitro* findings are in good accordance with an *in situ* study indicating that a 1 min rinsing with a solution containing 250 ppm fluoride significantly decreases the number of adhering bacteria under oral conditions.²⁰ However, irrespective of the real mechanism of the fluoride-induced caries prophylaxis, one of the open questions is whether the fluoride content can be increased to any values or whether there is an upper limit of the amount of fluoride that can be provided to the enamel’s core component, namely HAp.

In this study, the time scale of fluoride uptake was investigated by X-ray photoelectron spectroscopy (XPS)-based elemental depth profiling on fluoridated HAp samples, as representing a first order approximant of the enamel’s mineral phase. Of course, the present results cannot be directly transferred from synthetic HAp to natural enamel, but they can give at least an idea of the time scale of fluoride uptake.

EXPERIMENTAL SECTION

HAp samples were prepared using commercially available HAp powder (Sigma-Aldrich Chemie GmbH, Munich, Germany) with a mean particle size of ~ 70 nm.²¹ After a washing procedure,²¹ 1 g of the powder was placed in a stainless steel mold with a diameter of 16 mm (MsScientific, Berlin, Germany) and compacted with a uniaxial load of 20 kN resulting in a pressure of ~ 100 MPa. After extraction from the mold, the green bodies were sintered for 3 h at 1250 °C based on a temperature profile proposed by Prokopiev et al.²² The samples then featured a density of 97–99% of the crystallographic density of HAp, $\rho_{\text{HAp}} = 3.156$ g/cm³,²³ as measured via Archimedes’ principle. After sintering and before each fluoridation step, the sample was ground with SiC abrasive paper (Struers, Willich, Germany) of grit sizes P1200, P2000, and P4000 to obtain a new, nonfluoridated HAp surface. A detailed characterization of the samples concerning their material properties is described in ref 24.

For fluoridation, the sample was immersed in a buffer solution containing sodium acetate ($C_2H_3NaO_2$), acetic acid ($C_2H_4O_2$), and 500 ppm sodium fluoride (NaF) at $T = 37$ °C. The pH value of the buffer solution was nominally set to 5.5 (when monitored by an old-fashioned pH-meter the reading was pH 5–6). The fluoride

concentration of 500 ppm was chosen according to the suggestion by the German Federal Institute for Risk Assessment for over-the-counter drugs.²⁵ The application times were 0 s, 15 s, 30 s, 60 s, 90 s, 120 s, 180 s, 240 s, and 300 s. To avoid any influence of an accumulation of fluoride from one or several previous fluoridation experiments, the different time steps were recorded in arbitrary instead of in chronological order. After fluoridation, the sample was rinsed with ultrapure water to remove residues of the solvent and blown dry with nitrogen.

XPS was used to determine the chemical composition of the sample. The measurements were performed with an ESCA Lab Mk II spectrometer (Vacuum Generators, Hastings, England) in UHV ($\sim 10^{-10}$ mbar), using nonmonochromatized Al-K α radiation ($h\nu = 1486.6$ eV). Detail spectra of the Ca-2p, Ca-2s, P-2p, P-2s, O-1s, C-1s, Na-1s, and F-1s signals were recorded in normal emission geometry with a step width of 0.2 eV at a pass energy of 50 eV. For quantitative analysis, a Shirley background correction²⁶ was applied, and the peak areas were weighted with the corresponding photoemission cross-sections to get the concentration of an element in terms of atomic percent (at-%).²⁷ The Ca- and P-intensities were acquired by averaging the respective 2s and 2p peak areas. Because of charging of the samples, binding energies were calibrated by setting the P-2p signal at 133.7 eV, i.e., at the mean value for P bonded in HAp (133.6 eV) and in FAp (133.8 eV), according to ref 28.

For depth profiling of the fluoride content in the sample’s subsurface range, XPS was combined with Ar⁺ ion etching using an IQ-100 ion source (Vacuum Science Instruments, Bad Schwalbach, Germany). Ion energy and emission current were set to 4 kV and 10 mA, respectively, resulting in an ablation of ~ 0.3 Å per minute. The calibration of the ablation rate was performed according to the procedure described in ref 16.

RESULTS AND DISCUSSION

The HAp samples used for the fluoridation experiments have been described in a previous study in terms of material properties, such as crystal structure, chemical composition, surface roughness, domain size distribution, and microhardness.²⁴ XRD data concerning the crystal structure of the powder as well as of the sintered samples and XPS data concerning the stoichiometry of both types of samples can be found in the Supporting Information.

Figure 1 shows typical distributions of the relative amount of fluoride and sodium as a function of ablation z . The concentration of both elements was obtained from XPS data via the cross-section normalized F-1s and Na-1s peak intensities when compared to the Ca-2p, Ca-2s, P-2p, P-2s, and O-1s intensities. The presence of Na may result from residues from the NaF agent that is (despite rinsing) still adsorbed on the surface or trapped in pores or grain boundaries. In order to exclude fluoride contributions from the agent, the experimental F distribution (hollow dots in Figure 1) was normalized to zero Na content simply by subtracting the Na distribution. This normalized F distribution (full dots in Figure 1) then represents in a first order approximation the fluoridated surface layer and can be described by an exponential decrease via

$$n(t, z) = n_0(t) \cdot \exp(-z/d(t)) \quad (1)$$

with $n_0(t)$ describing the initial fluoride concentration at the surface (in at-%) and $d(t)$ describing the attenuation length (i.e., the mean thickness of the F^- ions containing surface layer) for a particular application time t . Data shown in Figure 1 were achieved by the application of a 500 ppm NaF buffer solution for 5 min, resulting in $n_0(300 \text{ s}) = 2.8 \pm 0.1$ at-% and $d(300 \text{ s}) = 12.7 \pm 1.0$ nm. These values are in the same order of magnitude as those reported for fluoridation of HAp samples in a 246 ppm of NaF solution under similar conditions.¹⁶

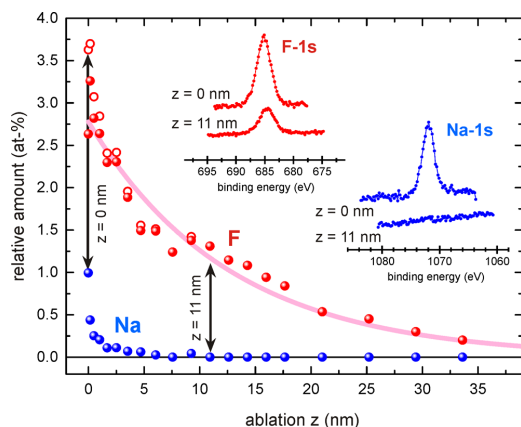
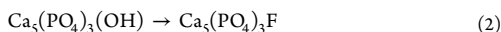


Figure 1. Elemental depth profiles of the F (red) and Na content (blue) of a HAp sample after application of a 500 ppm NaF solution at 37 °C and pH ~5.5 for 5 min. The insets show typical XPS data of F-1s and Na-1s taken at the surface ($z = 0$ nm) and after ablation of 11 nm by Ar^+ ion etching. In the F profile, the hollow dots refer to the raw data, while the full dots represent the F profile when normalized to zero Na content (for details, see the text).

The formation of a fluoride containing surface layer, as displayed by Figure 1, can take place via several mechanisms: (i) the partial transformation of (bio-)HAp into FAP in the nearly neutral pH range,¹⁶ i.e.,



Here, HAp dissolves in the solution by releasing Ca- and P-ions which interact with the F-ions of the agent to form a less-soluble FAP layer on the remaining HAp surface. (ii) The formation of a surface layer formed by CaF_2 globules, which is expected especially in the lower pH range (i.e., pH 4.5), as demonstrated by AFM experiments in ref 29; and (iii) via the embedding of the NaF containing agent into microcavities (e.g., pores and cracks). While i represents a mechanism to form tightly bound fluoride, ii and iii provide rather loosely bound fluoride.³⁰

However, a distinct impact of the latter mechanism (i.e., F contributions from the agent itself) may be excluded in the present case since the Na content in Figure 1 drops to zero after a few nanometers, i.e., Na is only present as residues from the NaF agent at the surface (e.g., in grain boundaries), but it is not distributed in the bulk of the sample. The high density of the sintered HAp samples probably results in only a small volume fraction of noninterconnected pores which prohibits further diffusion of the agent.

Since the F^- depth distribution in Figure 1 almost exclusively displays the uptake of fluoride either via the HAp–FAP transformation (i) and/or via the formation of, e.g., an additional CaF_2 layer (ii), we can now turn to the initial question whether there are any limits for the relative amount of fluoride that can be provided to a HAp surface upon fluoridation.

Figure 2 shows the depth profiles of the F content similar to Figure 1 for varying the application time of the NaF agent between 0 and 300 s. With increasing application time, the initial F^- content as well as the penetration depth increase, but

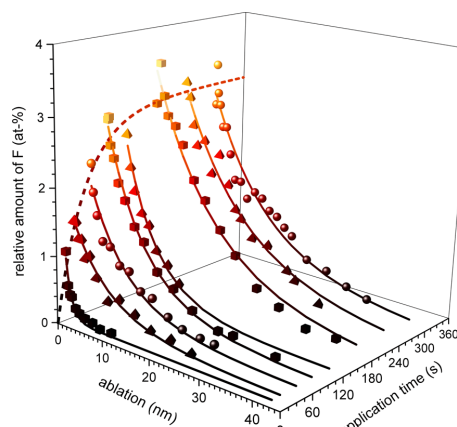


Figure 2. Depth profiles of the amount of fluoride (in at-%) dependent on the application time of the 500 ppm NaF solution at 37 °C and at pH ~5.5.

both parameters start to become constant after an application time in the range of about 3 min.

For a quantitative analysis, the experimental depth profiles in Figure 2 are fitted according to eq 1, and the corresponding parameters $n_0(t)$ and $d(t)$ are plotted versus application time in Figure 3.

In Figure 3a, $n_0(t)$ can be approximated as

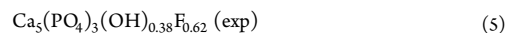
$$n_0(t) = n_{0,\text{max}} \cdot (1 - \exp(-t/\tau_n)) \quad (3)$$

and similarly, $d(t)$ can be approximated in Figure 3b as

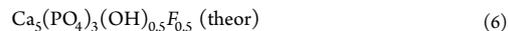
$$d(t) = d_{\text{max}} \cdot (1 - \exp(-t/\tau_d)) \quad (4)$$

with $n_{0,\text{max}}$ and d_{max} describing the maximum amount and maximum mean thickness of the fluoridated layer and τ_n and τ_d describing the corresponding growth constants.

In Figure 3a, the maximum of the fluoride content (i.e., for long-term application) at the surface is $n_{0,\text{max}} = 2.97 \pm 0.16$ at-% which corresponds to a HAp-FAP distribution of



with 62% of the $(\text{OH})^-$ groups substituted by F^- ions. These findings reflect the results of molecular dynamic (MD) simulations regarding the fluoride uptake at a HAp (0001) surface since in ref 31, de Leeuw reports that a 50%:50% mixed crystal, i.e., a solid solution, of HAp and FAP is energetically favored:



With respect to the penetration depth, the same calculations predict that the F ions do not penetrate into the HAp crystal more than 10 Å. The results from Figure 3b reveal, however, that the maximum mean thickness of the fluoridated layer exceeds the calculated value by 1 order of magnitude, i.e., $d_{\text{max}} = 13.2 \pm 1.9$ nm. The deviations between the experimental values and the theoretical results may be explained as follows:

Figure 4a shows an electron backscatter diffraction (EBSD) map of a HAp surface as it was used in this study. The different colors, as representing different orientations of crystallites relative to the sample surface, show that the surface consists of numerous grains of different crystal orientations and sizes in the

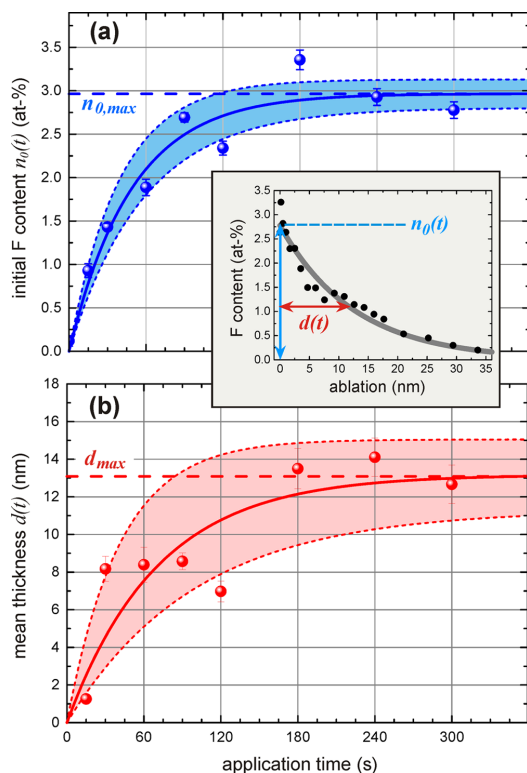


Figure 3. (a) Initial fluoride content $n_0(t)$ at the surface of the HAp sample after fluoridation of HAp with a 500 ppm NaF solution at 37 °C and pH \sim 5.5. (b) Mean penetration depth $d(t)$ of F^- ions. The inset to both diagrams illustrates the meaning of the parameters $n_0(t)$ and $d(t)$.

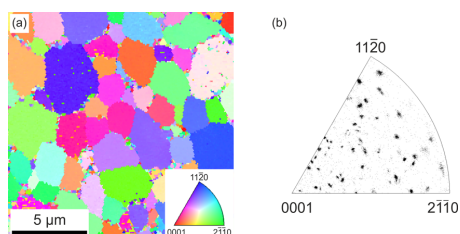


Figure 4. (a) EBSD map of a synthetic HAp surface. (b) Inverse pole figure corresponding to the scanned area shown in a.

(sub-) micron range. As shown in the inverse pole figure (Figure 4b), no preferred crystallite orientation (texture) could be observed (for further details about the crystallinity of the HAp samples, see ref 24). According to the nonuniform sample surface in terms of crystal orientation, it is not surprising that the experimental results from Figure 3 do not exactly match the theoretical values reported in ref 31.

Since XPS probes a surface area of several mm^2 , the values for $n_{0,max}$ and d_{max} are mean values obtained by averaging over $\sim 10^8$ crystallites (grains) of different sizes and orientations. The dissolution rates of HAp are strongly dependent on the

orientation of the crystallites.^{24,32} Therefore, we expect that both parameters, i.e., the amount of fluoride at the surface as well as the mean thickness of the fluoride layer, depend on the crystal orientation of each individual grain. This could explain the differences between the experimental values and the theoretical predictions since the MD simulations in ref 31 are based on a surface of uniform crystal orientation, namely, the (0001) basal plane exclusively.

From the data in Figure 3a, one gets a time constant of $\tau_n = 48.9 \pm 9.5$ s for reaching a constant value of the initial fluoride content, i.e., $n_0(t) = n_{0,max}$ at the surface. Similarly, the data in Figure 3b provide a time constant of $\tau_d = 70.7 \pm 29.4$ s for obtaining a constant value of the mean thickness of the fluoride layer, i.e., $d(t) = d_{max}$. In terms of both parameters, the time scale for the uptake of fluoride is (irrespective of the large error bars) at the level of typical periods of, e.g., tooth brushing. After about 3 min, both the amplitude $n_0(t)$ as well as the mean thickness $d(t)$ in Figure 3 reach their maximum values.

CONCLUSIONS

It can be concluded from our experiments on synthetic HAp samples that the uptake of fluoride benefits only in a limited period from the application time of dentifrices (as represented by a NaF solution in this study). We observed that the formation of a fluoride layer on the HAp surface stops when an $\sim 40:60$ HAp-FAp mixture is obtained. This finding meets roughly the theoretical prediction of a 50:50 HAp-FAp mixed phase as the most stable solid solution.³¹ The mean thickness of the observed mixed layer is about 13 nm, which is about 25% of the average crystallite's diameter in enamel.

At this point, we have to emphasize that the results obtained on synthetic HAp samples (as an artificial model "tooth") cannot be directly related to natural tooth enamel (i.e., bio-HAp) in terms of clinical relevance and dental care, especially since enamel differs from HAp in many ways: First of all, HAp represents the fundamental building block of enamel, which is built by a hierarchical structure of crystallites formed by bio-HAp that are embedded in an organic collagen matrix. This matrix may cause a shielding of the HAp crystallites from the fluoride containing agent, and it may also affect the material properties, such as, e.g., different mechanical hardness (see Figure S5 in Supporting Information). In addition, the enamel forming bio-HAp is a substituted variant of stoichiometric HAp containing ~ 3 wt-% carbonate (CO_3)²⁻ in the outer layers (as well as traces of other atomic species such as Na or Mg).³² All these modifications may result in different solubilities of bio-HAp compared to that of the synthetic apatite used in this study.^{32,33} Thus, the experiments performed in this study are expected to represent a first order approximation of the fluoride layer formation on the natural material.

ASSOCIATED CONTENT

Supporting Information

The Supporting Information is available free of charge on the ACS Publications website at DOI: 10.1021/acsbomaterials.6b00782.

XPS data of sintered HAp samples; particle size distribution of HAp powder; chemical composition of HAp powder and sintered sample; XRD analysis of HAp powder and sintered sample; and microhardness of HAp pellets compared to enamel (PDF)

AUTHOR INFORMATION

Corresponding Author

*E-mail: f.mueller@mx.uni-saarland.de.

ORCID

Thomas Faidt: 0000-0003-2035-786X

Notes

The authors declare no competing financial interest.

ACKNOWLEDGMENTS

We acknowledge support from the German Research Foundation (DFG) in the framework of the Collaborative Research Centre SFB 1027 "Physical modelling of non-equilibrium processes in biological systems". We thank M. J. Deckarm and J. Schmauch, Experimental Physics, Saarland University, for experimental support on the structural characterization of the HAp samples. We, moreover, want to thank an anonymous reviewer for her/his valuable comments and her/his elaborate report on the manuscript.

REFERENCES

- Blackberg, S. N.; Berke, J. D. Dental Caries Experimentally Produced in the Rat. *J. Dent. Res.* **1932**, *12*, 609–617.
- Black, G. V.; McKay, F. S. Mottled Teeth: An Endemic Developmental Imperfection of the Enamel of the Teeth Heretofore Unknown in the Literature of Dentistry. *Dent. Cosmos* **1916**, *58*, 129–156.
- Masaki, T.; Mumura, K. Geographical Distribution of the Mottled Teeth in Japan. *Shikwa Gakuho* **1931**, *36*, 875–893.
- Dean, H. T. Endemic Fluorosis and its Relation to Dental Caries. *Public Health Rep.* **1938**, *53*, 1443–1452.
- Dean, H. T.; Arnold, F. A., Jr.; Elvove, E. Domestic Water and Dental Caries. *Public Health Rep.* **1942**, *57*, 1155–1194.
- Cohen, H.; Locker, D. The Science and Ethics of Water Fluoridation. *J. Can. Dent. Assoc.* **2001**, *67*, 578–580.
- Sowers, M. R.; Clark, M. K.; Jannausch, M. L.; Wallace, R. B. A Prospective Study of Bone Mineral Content and Fracture in Communities with Differential Fluoride Exposure. *Am. J. Epidemiol.* **1991**, *133*, 649–660.
- Lee, B. S.; Chou, P. H.; Chen, S. Y.; Liao, H. Y.; Chang, C. C. Prevention of Enamel Demineralization with a Novel Fluoride Strip: Enamel Surface Composition and Depth Profile. *Sci. Rep.* **2015**, *5*, 13352.1–10.
- Pasteris, J. D.; Wopenka, B.; Freeman, J. J.; Rogers, K.; Valsami-Jones, E.; van der Houwen, J. A. M.; Silva, M. J. Lack of OH in Nanocrystalline Apatite as a Function of Degree of Atomic Order: Implications for Bone and Biomaterials. *Biomaterials* **2004**, *25*, 229–238.
- Featherstone, J. D. B.; ten Cate, J. M. Physicochemical Aspects of Fluoride-Enamel-Interactions. In *Fluoride in Dentistry*; Ekstrand, J., Fejerskov, O., Silverstone, L. M., Eds.; Munksgaard International Publishers: Copenhagen, 1988; pp 125–149.
- Dawes, C. What is the Critical pH and Why Does a Tooth Dissolve in Acid? *J. Canadian Dent. Assoc.* **2003**, *69*, 722–724.
- Gerth, H. U. V.; Dammaschke, T.; Schäfer, E.; Züchner, H. A Three Layer Structure Model of Fluoridated Enamel Containing CaF₂, Ca(OH)₂, and FAp. *Dent. Mater.* **2007**, *23*, 1521–1528.
- Uchtmann, H.; Duschner, H. Basic Biological Sciences: Electron Spectroscopic Studies of Interactions between Superficially-applied Fluorides and Surface Enamel. *J. Dent. Res.* **1982**, *61*, 423–428.
- Duschner, H.; Uchtmann, H. Effect of Sodium Fluoride, Stannous Fluoride, Amine Hydrofluoride and Sodium Monofluorophosphate on the Formation of Precipitates Adhering to Bovine Enamel. *Caries Res.* **1988**, *22*, 65–71.
- Caslavska, V.; Duschner, H. Effect of a Surface-Active Cation on Fluoride/Enamel Interactions in vitro. *Caries Res.* **1991**, *25*, 27–33.
- Müller, F.; Zeitz, C.; Mantz, H.; Ehses, K.-H.; Soldera, F.; Schmauch, J.; Hannig, M.; Hüfner, S.; Jacobs, K. Elemental Depth Profiling of Fluoridated Hydroxyapatite: Saving Your Dentition by the Skin of Your Teeth? *Langmuir* **2010**, *26*, 18750–18759.
- de Leeuw, N. H. Resisting the Onset of Hydroxyapatite Dissolution through the Incorporation of Fluoride. *J. Phys. Chem. B* **2004**, *108*, 1809–1811.
- Loskill, P.; Zeitz, C.; Grandthyll, S.; Thewes, N.; Müller, F.; Bischoff, M.; Hermann, M.; Jacobs, K. Reduced Adhesion of Oral Bacteria on Hydroxyapatite by Fluoride Treatment. *Langmuir* **2013**, *29*, 5528–5533.
- ten Cate, J. M. Contemporary Perspective on the Use of Fluoride Products in Caries Prevention. *Br. Dent. J.* **2013**, *214*, 161–167.
- Hannig, C.; Gaeding, A.; Basche, S.; Richter, G.; Helbig, R.; Hannig, M. Effect of Conventional Mouthrinses on Initial Bioadhesion to Enamel and Dentin in situ. *Caries Res.* **2013**, *47*, 150–161.
- Zeitz, C. Zahnhartgewebe im Fokus: In vitro-Untersuchungen zur Biokompatibilität von fluorierten und nichtfluorierten Hydroxyapatit-Modelloberflächen. Ph.D. Thesis, Saarland University, 2013.
- Prokopiev, O.; Sevostianov, I.; Genin, J.; McGee, S. M.; Woodward, C. Microstructure and Elastic Properties of Sintered Hydroxyapatite. *Int. J. Fract.* **2004**, *130*, L183–L190.
- De With, G.; Van Dijk, H. J. A.; Hattu, N.; Prijs, K. Preparation, Microstructure and Mechanical Properties of Dense Polycrystalline Hydroxy Apatite. *J. Mater. Sci.* **1981**, *16*, 1592–1598.
- Zeitz, C.; Faidt, T.; Grandthyll, S.; Hähl, H.; Thewes, N.; Spengler, C.; Schmauch, J.; Deckarm, M. J.; Gachot, C.; Natter, H.; Hannig, M.; Müller, F.; Jacobs, K. Synthesis of Hydroxyapatite Substrates: Bridging the Gap between Model Surfaces and Enamel. *ACS Appl. Mater. Interfaces* **2016**, *8*, 25848–25855.
- Federal Institute for Risk Assessment (Bundesinstitut für Risikobewertung). *Stellungnahmen: Fluoridhaltige Mundwässer und Alkoholgehalt in Mund- und Zahnpflegemitteln*. German Federal Ministry of Food and Agriculture: Berlin, Germany, 2003.
- Shirley, D. A. High-Resolution X-Ray Photoemission Spectrum of the Valence Bands of Gold. *Phys. Rev. B* **1972**, *5*, 4709–4714.
- Yeh, J. J.; Lindau, I. Atomic Subshell Photoionization Cross Sections and Asymmetry Parameters: $1 \leq Z \leq 103$. *At. Data Nucl. Data Tables* **1985**, *32*, 1–155.
- Landis, W. J.; Martin, J. R. X-Ray Photoelectron Spectroscopy Applied to Gold-Decorated Mineral Standards of Biological Interest. *J. Vac. Sci. Technol., A* **1984**, *2*, 1108–1111.
- Petzold, M. The Influence of Different Fluoride Compounds and Treatment Conditions on Dental Enamel: A Descriptive in vitro Study of the CaF₂ Precipitation and Microstructure. *Caries Res.* **2001**, *35*, 45–51.
- Takagi, S.; Liao, H.; Chow, L. C. Effect of Tooth-Bound Fluoride on Enamel Demineralization/Remineralization in vitro. *Caries Res.* **2000**, *34*, 281–288.
- de Leeuw, N. H. A Computer Modelling Study of the Uptake and Segregation of Fluoride Ions at the Hydrated Hydroxyapatite (0001) Surface: Introducing a Ca₁₀(PO₄)₆(OH)₂ Potential Model. *Phys. Chem. Chem. Phys.* **2004**, *6*, 1860–1866.
- Legfros, R. Z.; Sakae, T.; Bautista, C.; Retino, M.; LeGeros, J. P. Magnesium and Carbonate in Enamel and Synthetic Apatites. *Adv. Dent. Res.* **1996**, *10*, 225–231.
- Kwon, K.; Wang, E.; Chung, A.; Chang, N.; Saiz, E.; Choe, U.; Koobatian, M.; Lee, S. Defect Induced Asymmetric Pit Formation on Hydroxyapatite. *Langmuir* **2008**, *24*, 11063–11066.

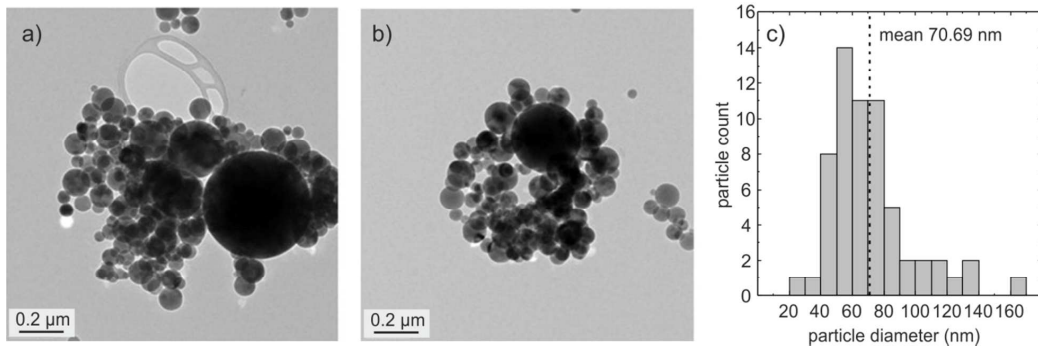


Figure S2: a), b) TEM micrographs of washed HAp powder. c) Analysis of the particle diameter distribution based on 61 particles from TEM micrographs.¹

Table T1: Stoichiometry of HAp powder and sintered samples, measured with XPS. For better comparison, values were normalized to the nominal P content in stoichiometric HAp. The calcium deficiency in the sintered sample before Ar ion ablation might be due to preferred wet chemical etching during the preparation process. For further details see ref. 1.

		Ca	P	O	C	Ca:P	Ca:O
HAp powder	as received	4.9	3	17.2	4.1	1.63	0.28
	washed in water	4.6	3	14.0	3.2	1.53	0.33
sintered sample	as sintered	4.0	3	12.8	2.0	1.33	0.31
	after Ar ion etching	4.6	3	11.4	0.8	1.53	0.40
formula unit		5	3	13	0	1.67	0.38

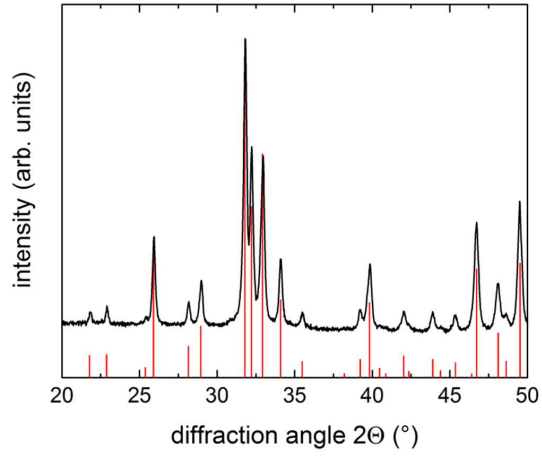


Figure S3: XRD pattern of the HAp powder. The red bars show the XRD pattern of stoichiometric HAp according to PDF reference 98-004-7182.¹

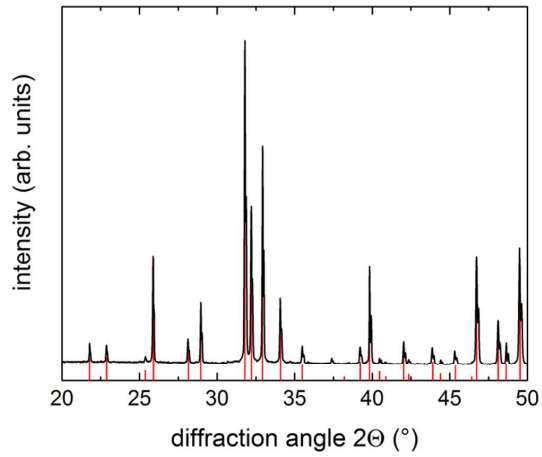


Figure S4: XRD pattern of the sintered HAp sample and PDF reference 98-004-7182.¹

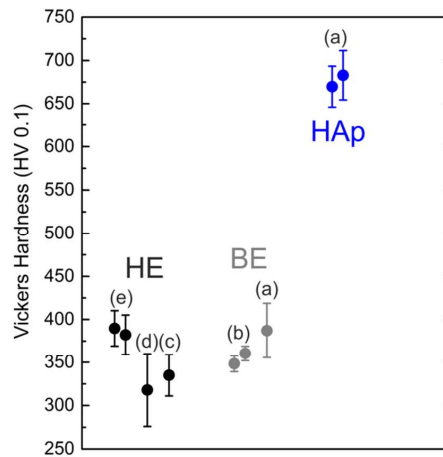


Figure S5: Microhardness of enamel and HAp samples, tested via Vickers hardness tests. Our sintered HAp samples feature a hardness of 676 ± 26 HV0.1 which is almost twice as large as the values for bovine (BE) and human enamel (HE) according to references 1 (a), 2 (b), 3 (c), 4 (d) and 5 (e).

- (1) Zeitz, C.; Faidt, T.; Grandthyll, S.; Hähl, H.; Thewes, N.; Spengler, C.; Schmauch, J.; Deckarm, M.J.; Gachot, C.; Natter, H.; Hannig, M.; Müller, F.; Jacobs, K. Synthesis of Hydroxyapatite Substrates: Bridging the Gap between Model Surfaces and Enamel. *Appl. Mat. Interf.* **2016**, *8*, 25848–25855, DOI: 10.1021/acsami.6b10089.
- (2) Mundra, S.; Mohan, V.; Gwyer, J.; Young, N.; Franklin, S.E.; Gerhardt, L.-C. Hardness, friction and wear studies on hydrogen peroxide treated bovine teeth. *Tribol. Int.* **2015**, *89*, 109–118.
- (3) Aydin, B.; Pamir, T.; Baltaci, A.; Orman, M.N.; Turk, T. Effect of storage solutions on microhardness of crown enamel and dentin. *Eur. J. Dent.* **2015**, *9*, 262–266.
- (4) Chuenarrom, C.; Benjakul, P.; Daosodsai, P. Effect of indentation load and time on Knoop and Vickers microhardness tests for enamel and dentin. *Mat. Res.* **2009**, *12*, 473–476.
- (5) Akal, N.; Over, H.; Olmez, A.; Bodur, H. Effects of carbamide peroxide containing bleaching agents on the morphology and subsurface hardness of enamel. *J. Clin. Pediatr. Dent.* **2001**, *25*, 293–296.

III: Effect of Fluoride Treatment on the Acid Resistance of Hydroxyapatite

Authors: **T. Faidt**, A. Friedrichs, S. Grandthyll, C. Spengler, K. Jacobs, and F. Müller

Experimental Physics, Saarland University, 66123 Saarbrücken, Germany.

Reprinted with permission from *Langmuir* 34 (2018), pp. 15253–15258.

Copyright 2018 American Chemical Society.

<https://doi.org/10.1021/acsbiomaterials.6b00782>

Author contributions:

T. Faidt produced hydroxyapatite samples, supervised AFM experiments, performed XPS measurements, analyzed XPS data and wrote the manuscript. A. Friedrichs performed AFM measurements and assisted in writing the manuscript. S. Grandthyll performed XPS measurements and analyzed XPS data. C. Spengler analyzed AFM data and assisted in writing the manuscript. K. Jacobs directed experimental work and wrote the manuscript. F. Müller directed experimental work, performed XPS measurements, analyzed XPS data and wrote the manuscript.

Abstract – The etching behavior of polycrystalline synthetic hydroxyapatite samples has been evaluated to explore the protective impact of fluoride on a tooth-like model system. Etching rates before and after fluoridation with a NaF solution at pH 6 were determined by atomic force microscopy. Despite a very low F concentration of ca. 0.2 atom % in the hydroxyapatite surface, a very strong effect on the acid resistance can be observed. Depending on the crystal orientation, etching in a NaAc buffer at pH 4.5 was completely inhibited for at least 5 min. The major part of the surface withstood etching even for more than 23 min. These results give new insights into how the amount of incorporated fluoride in hydroxyapatite correlates with its protective impact.

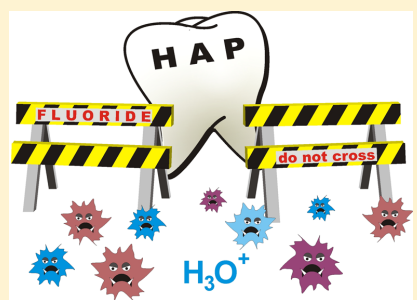
Effect of Fluoride Treatment on the Acid Resistance of Hydroxyapatite

Thomas Faidt,[✉] Andreas Friedrichs, Samuel Grandthyll, Christian Spengler, Karin Jacobs, and Frank Müller^{*}

Experimental Physics, Saarland University, Campus E2 9, 66123 Saarbrücken, Germany

Supporting Information

ABSTRACT: The etching behavior of polycrystalline synthetic hydroxyapatite samples has been evaluated to explore the protective impact of fluoride on a tooth-like model system. Etching rates before and after fluoridation with a NaF solution at pH 6 were determined by atomic force microscopy. Despite a very low F concentration of ca. 0.2 atom % in the hydroxyapatite surface, a very strong effect on the acid resistance can be observed. Depending on the crystal orientation, etching in a NaAc buffer at pH 4.5 was completely inhibited for at least 5 min. The major part of the surface withstood etching even for more than 23 min. These results give new insights into how the amount of incorporated fluoride in hydroxyapatite correlates with its protective impact.



INTRODUCTION

Dental caries is one of the most widespread diseases of the world. In 2012, the World Health Organization reported that 60–90% of school children and nearly every adult were affected by caries.¹ In the same report, it was stated that “dental cavities can be prevented by maintaining a constant low level of fluoride in the oral cavity”.¹

Dental caries is caused by acidic metabolic products of bacteria in the plaque, e.g., lactic acids. These lead locally to a reduced pH. When the pH falls below a critical value, demineralization sets in and the enamel starts to dissolve. This critical pH is often reported to be around 5.5;^{2–4} however, it is not a constant and depends on the concentrations of calcium and phosphate in the enamel's surrounding.⁵ The pH of carious dentin was found to be in the range of 4.4–6.9, with active caries lesions typically lying between pH 4.5 and 4.9.⁶

A correlation between fluoride intake and dental caries was found already around 1940 when Dean et al. reported on the reduced caries occurrence among school children living in areas with higher fluoride content in the public water supply.^{7,8} More recent studies confirm the anterosive and caries-prophylactic effects of fluoride treatment.^{9–11} One of the most common approaches to explain the mechanism of a fluoride-induced protection against caries is that a partial transformation of the mineral phase of the enamel from hydroxyapatite (HAp, i.e., $\text{Ca}_5(\text{PO}_4)_3\text{OH}$) to fluoroapatite (FAP, i.e., $\text{Ca}_5(\text{PO}_4)_3\text{F}$) leads to a decreased threshold of the pH value below which demineralization starts. This threshold is at pH 5.5 for HAp, whereas it is decreased to pH 4.6 for FAP.¹²

Many experimental studies focus on the quantification of dissolution rates of natural enamel¹³ or synthetic HAp^{14,15} or

concentrate on the characterization of the topography of enamel^{16–18} or synthetic HAp¹⁹ after fluoride treatment and subsequent exposure to an etching agent. Although it is difficult to work with real enamel because of statistical differences in chemical composition between individual teeth, most of these studies do not describe the exact composition of the used material before and after fluoride treatment. In some studies (e.g., ref 20), the variation in calcium/phosphate ion content of the enamel surface with erosion time is characterized by energy dispersive X-ray; but, there is no information of the fluoride content. Therefore, it is difficult to correlate the protective effects of fluoridation with the amount of fluoride incorporated into the surface. However, in theoretical studies (using molecular dynamics simulations^{21,22} or density functional theory^{22,23}), the chemical composition is exactly defined. Here, the protective effect of fluoride can be understood in terms of different surface potentials.²¹ At the same time, the authors of these theoretical studies express the urgent need to collect more accurate experimental data for HAp/FAP surface composition to allow for a quantitative comparison between the experiment and the theory. The aim of this study is therefore (i) to provide the experimental data with a quality corresponding to the theoretical descriptions of the system and (ii) to quantify the protective effect of fluoridation against acid attacks.

In a former study, we revealed that the thickness of the HAp layer that can be loaded with fluoride is in the range of only a few nanometers,^{24,25} even if loaded under optimal conditions.²⁵ Thus, the question arose whether such a thin

Received: October 10, 2018

Published: November 13, 2018

layer would actually be capable of protecting the surface against acid attacks. In this study, we therefore determine by atomic force microscopy (AFM) the etching rates of nonfluoridated and fluoridated synthetic HAp surfaces at pH 4.5.

EXPERIMENTAL SECTION

HAp pellet samples were prepared by compacting and sintering commercially available HAp nanopowder (Sigma-Aldrich Chemie GmbH, Munich, Germany). The synthesis and characterization of these samples have been discussed in detail in a former study.²⁶ After the sintering process, the samples were ground using a polishing machine ("Saphir 520", ATM GmbH, Mammelzen, Germany) and SiC abrasive papers of decreasing grain sizes P1200, P2000, and P4000 (Struers GmbH, Willich, Germany). Subsequently, the pellets were machine-polished with a water-based suspension containing 3 μm sized diamonds ("DiaPro", Struers GmbH, Willich, Germany) and manually polished with a water-based suspension of 18 nm sized diamonds ("Liquid Diamond MSY 0-0.03 GAF", Microdiamant AG, Lengwil, Switzerland). Finally, the surfaces were etched for 8 s in a sodium acetate (NaAc) buffer solution (pH 4.5) and cleaned for 5 min in an ultrasonic bath in ultrapure water to remove residues of the polishing suspension.

To get a well-defined height reference, which is inert to the buffer solution used in the etching experiments, a gold film was evaporated onto the HAp surface. To obtain a sharp transition between this reference surface and the HAp surface, the gold film was then partially removed by pulling it off with an adhesive tape (tesa SE, Norderstedt, Germany), yielding a sample schematically shown in Figure 1a. The thickness of the gold film, i.e., the step height between gold and HAp, was around 40 nm, as determined by AFM.

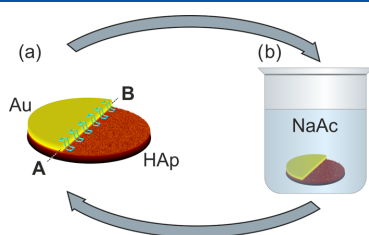


Figure 1. Sketch of the experimental procedure: (a) AFM micrographs were recorded in air at multiple positions (blue markings) along the line (A–B) with fast scanning direction perpendicular to (A–B). (b) The sample was etched in NaAc buffer for different application times. The steps (a) and (b) were repeated alternately.

For the experiments with fluoridated HAp, the sample was submerged for 5 min in a NaAc buffer (pH 6.0) containing 500 ppm NaF at a temperature of 37 °C. Immediately after fluoride treatment, the sample was rinsed with ultrapure water, followed by cleaning in an ultrasonic bath in ultrapure water for 5 min. Fluoridation was carried out before the deposition of the gold film.

X-ray photoelectron spectroscopy (XPS) measurements were performed with an ESCALab Mk II spectrometer (Vacuum Generators, Hastings, England). Detail spectra of the Ca 2s, Ca 2p, P 2s, P 2p, O 1s, C 1s, and F 1s electrons were recorded using non-monochromatized Al K α radiation ($h\nu = 1486.6$ eV). All the spectra were recorded in normal emission geometry with a pass energy of 50 eV and a step size of 0.2 eV. A Shirley background correction²⁷ was applied to the data and the peak areas were weighted with their corresponding photoemission cross sections.²⁸ For Ca and P, the intensities of the 2s and 2p signals were averaged to get their respective concentrations.

All the AFM measurements were carried out in dynamic mode in air on a Dimension Icon AFM with FastScan-C tips and a Nanoscope V Controller (Bruker Nano, Santa Barbara, CA). All the micrographs were recorded with dimensions of 30 $\mu\text{m} \times 15 \mu\text{m}$ (512 \times 256 pixels) and with the Au–HAp transition passing from top to bottom approximately through the center of the image.

To determine the etching rates, the samples were etched in a pH 4.5 NaAc buffer at room temperature, subsequently rinsed with ultrapure water, blow dried with nitrogen, and then measured by AFM. To resolve the time dependence of the etching behavior, these steps were carried out several times. The nonfluoridated sample was etched in 30 s intervals up to a total etching time of 330 s. After fluoridation, the sample was etched several times for increasing intervals of 10, 20, 30, 180, and 360 s up to a total etching time of 1770 s.

AFM images were flattened (zeroth order) and plane fitted (first order, at gold surface) using the software Nanoscope Analysis 1.5 (Bruker Nano, Santa Barbara, CA). Gaussian fits to the height distributions (i.e., the relative occurrence of the z -values when using all the pixels of an AFM image) were calculated with the software Origin Pro 2017 (OriginLab Corporation, Northampton, MA) using a linear combination of Gaussian functions

$$p(z) = p_0 + \sum_{n=0}^b a_n \exp\left(-\frac{(z - z_n)^2}{2\sigma_n^2}\right) \quad (1)$$

where a_n , z_n , and σ_n are parameters for the amplitude (in terms of occurrence), position (in terms of a particular height value), and the standard deviation of peak n and b is the total number of Gaussians used.

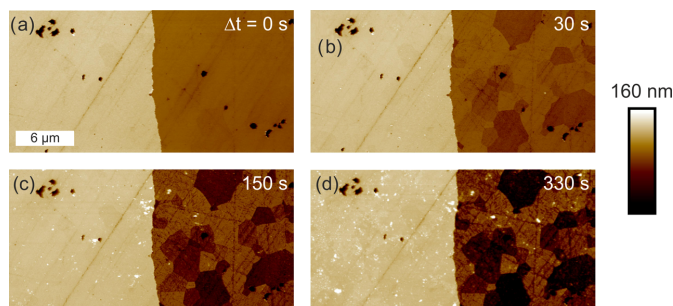


Figure 2. Exemplary AFM height images of a partially gold-covered HAp surface (Au left, HAp right). The micrographs show the topographical changes of the HAp after (a) 0 s, (b) 30 s, (c) 150 s, and (d) 330 s of etching with NaAc buffer at pH 4.5.

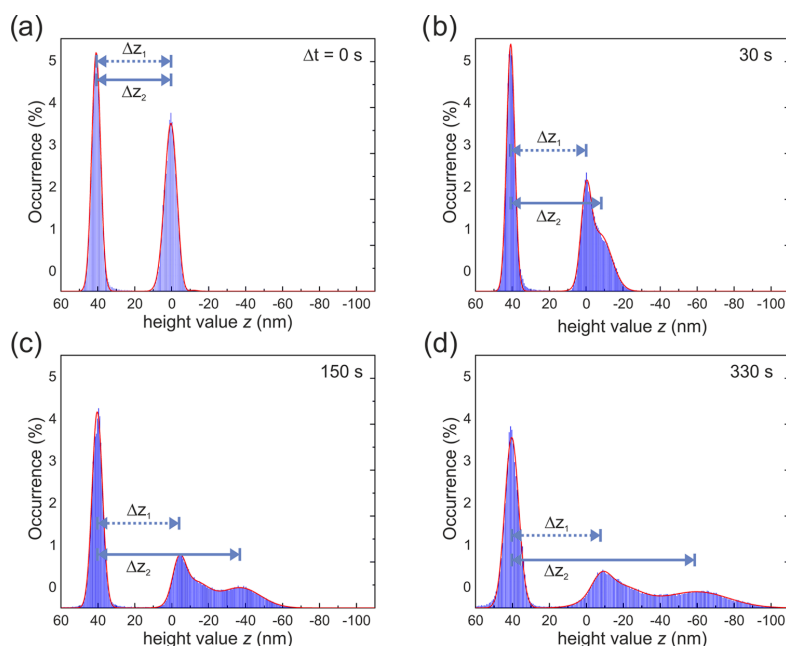


Figure 3. Height distributions as extracted from the micrographs in Figure 2 after (a) 0 s, (b) 30 s, (c) 150 s, and (d) 330 s of etching. Peaks at $z \approx 40$ nm represent the gold surface, peaks at lower z -values belong to the slowly (Δz_1) and quickly (Δz_2) etching areas of the HAp surface.

RESULTS AND DISCUSSION

A nonfluoridated HAp sample was etched in 30 s intervals up to an overall etching time of 330 s. After every etching step, the surface was scanned at 12 different positions (along the (A–B) direction in Figure 1a) with the fast scanning direction perpendicular to the Au–HAp step, yielding images as shown in Figure 2.

With increasing etching time, the step height between the gold reference and the HAp surface increases, indicating a loss of HAp substance. Even after a short etching time of 30 s, areas of different heights become visible at the HAp surface. These differences are due to the polycrystallinity of the material: depending on their orientation, some crystallites are etched stronger than others.²⁶

To evaluate the step height at the Au–HAp transition, we used the height distributions of pixels in the images. In Figure 3, the height distributions (as extracted from the images of Figure 2) display 2 or 3 prominent peaks.

The maximum at $z \approx 40$ nm can be assigned to the gold reference surface. The peaks at lower z -values correspond to the HAp surface. Because of the different etching rates of the crystallites, the HAp peak splits up and the resulting peaks diverge from each other with increasing etching time t . The distances Δz_1 and Δz_2 between the gold maximum and the HAp maxima are the step heights for the slow- and fast-etching HAp crystallites, respectively.

The ablation of the surface was determined by comparing the corresponding step heights in images at the same position before and after the preceding etching step. This was done for all 12 positions separately before averaging the ablation of the 12 positions to get the mean ablation for fast- and slow-etching areas. The total ablation a at a particular etching time can then

be calculated by summing up the mean ablations of the single etching intervals. Figure 4 shows the ablation a of the HAp surface depending on the etching time t .

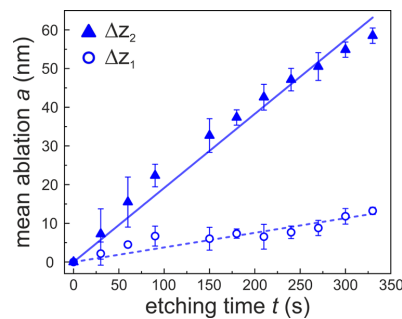


Figure 4. Ablation of the HAp surface during etching for quickly etching areas (triangles) and for slowly etching areas (circles). Error bars show the standard deviation of the mean values.

By fitting lines through the origin to the data, we determined the etching rates for areas that are etched slowly, $r_{\text{HAP,slow}} = 0.038(2)$ nm/s, and for areas that are etched quickly, $r_{\text{HAP,fast}} = 0.191(5)$ nm/s. These data confirm the well-known phenomenon that the dissolution of HAp in acids is highly dependent on crystal orientations, as first reported by Jongebloed et al. in 1974.²⁹

After the etching experiments on the nonfluoridated substrate, the same sample was ground and polished to restore a smooth surface as described in the Experimental Section. Before evaporating the gold layer onto the surface, the sample

was fluoridated as described in the [Experimental Section](#). The XPS measurements revealed the elemental composition of the HAp surface directly after fluoridation (and partial covering with gold), after 330 s, and after 1770 s of etching at pH 4.5 ([Table 1](#)).

Table 1. Elemental Composition (in Terms of Atoms Per Formula Unit) of the Fluoridated HAp Surface as Measured by XPS^a

	Ca	P	O	F	C
after preparation	3.84	3.00	10.06	0.043	4.22
330 s etched	3.07	3.00	10.78	0.045	21.56
1770 s etched	3.02	3.00	11.49	0.026	27.99

^aAll values are normalized to 3 P atoms in the formula unit.

The F content was considerably lower than that reported in one of our previous studies concerning the fluoride uptake in HAp.²⁵ These differences can be explained by the application of ultrasound to clean the sample. Whereas in [ref 25](#), the surface was only rinsed with ultrapure water after the fluoridation, in this study, the sample was additionally cleaned in a sonicator before the XPS measurements. Thereby, loosely bound fluoride is released from the surface and only the tightly bound fluoride remains in the sample. The data in [Table 1](#) shows a slight decrease in the Ca-concentration after etching, which is most likely due to a preferred release of Ca²⁺ ions in an acidic environment. In contrast to Ca, the C content was increased significantly during etching, which can be explained with a deposition of C-containing compounds from the buffer. The F concentration did not change in the first 330 s of etching but was reduced to ca. 50% after a total time of 1770 s in the etching solution, indicating that long-term etching removes at least part of the fluoridated surface layer.

Because of the low F content, we initially chose shorter etching intervals of 10 s to investigate the etching rate on the fluoridated HAp surface. However, according to [Figure 5](#), there was no influence of the etching solution on the HAp surface until a cumulative etching time of 330 s ([Figure 5a,b](#)). This shows that even very low concentrations of fluoride can have a significant impact on the etching behavior of HAp. This result is in good accordance with the molecular dynamics simulations by de Leeuw, who reported that incorporated fluoride can make HAp more resistant to dissolution “through the fluoride

ions’ resistance toward dissolution into the solvent, but also through their anchoring of the surface calcium ions”.²¹

After an etching time of 510 s, first changes in the HAp surface can be observed ([Figure 5c](#)). The etching then takes place in a very inhomogeneous way even on single grains, in contrast to the rather homogeneous etching of single grains in the nonfluoridated sample in [Figure 2](#).

As the surface was not modified during the first 330 s of etching, there was only one etching rate to be evaluated for this period of time. [Figure 6](#) shows the ablation of both

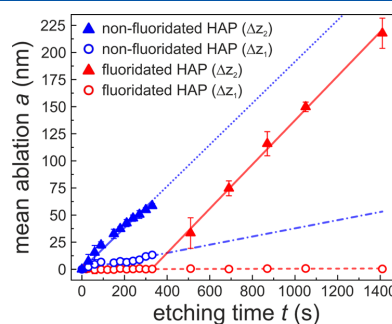


Figure 6. Ablation versus time of a fluoridated HAp surface (red) by etching at pH 4.5; data for nonfluoridated HAp (blue) are shown for comparison. The blue linear fits are extended for better comparison with the data of fluoridated HAp. Fluoridation completely inhibits the etching process until a cumulative etching time of at least 330 s.

nonfluoridated and fluoridated samples depending on the etching time. The etching rate for the virtually nonetching part of the fluoridated sample was determined to be $r_{\text{HAP,slow}} = 0.0005(2) \approx 0$ nm/s.

Because of the small surface fraction that was etched after 330 s, it was not possible to assess the etching rate of these quickly etching spots by evaluating the whole image. Therefore, we chose 3 single spots in the images that were evaluated separately (e.g., green box in [Figures 5d](#) and [S2](#) in the Supporting Information). That way, the etching rate for the selected spots could be determined as $r_{\text{HAP,fast}} = 0.204(6)$ nm/s. Interestingly, this value is very close to the etching rate of the quickly etched areas in the nonfluoridated sample, $r_{\text{HAP,fast}}$ i.e.,

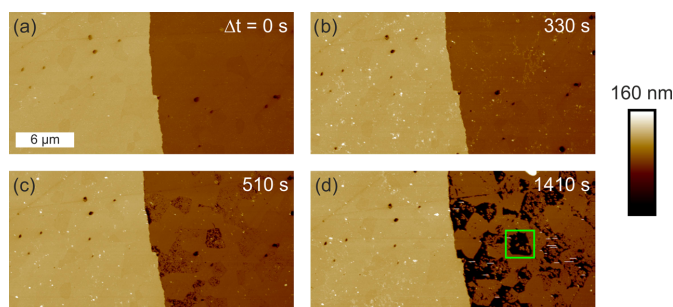


Figure 5. AFM micrographs of the fluoridated HAp surface after (a) 0 s, (b) 330 s, (c) 510 s, and (d) 1410 s of etching in NaAc buffer at pH 4.5. In contrast to the nonfluoridated HAp surface, the surface did not show topographical changes before a cumulative etching time of 330 s. For the corresponding height distributions, see [Figure S1](#) in the Supporting Information.

the protective fluoridated surface layer at these areas seems to be removed upon etching.

A possible explanation for the etching behavior of the HAp surface after fluoride treatment is that a thin layer of fluoridated HAp forms directly at the surface. In a previous study, we could show that the thickness of such a layer will not exceed ca. 13 nm.²⁵ As mentioned earlier in the article, the dissolution rate of HAp is higher along the *c*-axis than along other crystal directions.^{26,29} We therefore suggest that during the immersion in the etching solution, F⁻ ions will be released preferentially from crystallites with the *c*-axis perpendicular to the sample surface. After ca. 330 s of etching, the F concentration in these grains might be partially depleted, which would lead to a loss of the protective effect observed earlier.

In terms of fluoride-induced caries prophylaxis, we have to emphasize that our HAp samples represent a very simplified model system of the tooth surface. Whereas the natural enamel consists of carbonated HAp (bio-HAp) with varying solubilities^{30,31} and is built from needle-like grains embedded in an organic matrix, our synthetic samples are of pure HAp (with small C contaminations) and do not feature a preferred crystal orientation.²⁶

However, the increased acid resistance of fluoridated HAp (or enamel) seems to be only one mechanism among others. In addition to the above-described “classical” approach of an increased demineralization threshold, the protective nature of fluoridation may also have another impact: In a former study, we found that adhesion forces of bacteria are significantly lower on fluoridated HAp surfaces.³² Determining the adhesion forces, of bacteria-coated AFM cantilevers to HAp surfaces before and after fluoride treatment, we recorded, independently of the bacterial species (*Streptococcus mutans*, *Streptococcus oralis*, and *Staphylococcus carnosus*), 50% lower adhesion forces on fluoridated HAp.

CONCLUSIONS

We have tested synthetic HAp samples before and after fluoride treatment concerning their ability to withstand acid attacks in a sodium-acetate buffer (pH 4.5), using XPS to quantify the fluoride content in the samples’ surface and AFM to measure the absolute ablation due to etching.

We determined a very low total concentration of F in the sample after fluoride treatment; nevertheless, there is a very strong influence on the acid resistance of HAp. After fluoridation, the etching was completely inhibited until a cumulative etching time of 330 s. Upon further etching, some areas started to dissolve with roughly the same etching rate as in the case of a nonfluoridated sample. However, the largest part of the fluoridated HAp surface was still apparently inert to the etching solution even after a cumulative etching time of more than 23 min. Owing to the exact knowledge of the samples’ chemical compositions at the surface, the results can also be meaningfully compared with molecular dynamics simulations,²¹ which agree excellently.

The results of one of our former studies on the reduced adhesion forces of bacteria on fluoridated HAp³² and the findings of the present study lead to the conclusion that the caries-preventive effect of fluoride is an interplay of at least two mechanisms: a reduction in the solubility and a reduction in the bacterial adhesion force. Furthermore, the results of this study can be seen as evidence that already thin and low-

concentration fluoridated layers have a large effect on the acid resistance of HAp.

ASSOCIATED CONTENT

Supporting Information

The Supporting Information is available free of charge on the ACS Publications website at DOI: 10.1021/acs.langmuir.8b03412.

Height distributions of fluoridated HAp (Figure S1), AFM micrographs and height distributions of selected areas of fluoridated HAp (Figure S2) (PDF)

AUTHOR INFORMATION

Corresponding Author

*E-mail: f.mueller@mx.uni-saarland.de.

ORCID

Thomas Faidt: 0000-0003-2035-786X

Notes

The authors declare no competing financial interest.

ACKNOWLEDGMENTS

We acknowledge the support from the German Research Foundation (DFG) in the framework of the Collaborative Research Centre, SFB 1027, “Physical modeling of non-equilibrium processes in biological systems”.

REFERENCES

- WHO Oral Health Fact Sheet. Oral Health Database. <https://www.mah.se/CAPP/Oral-Health-Promotion/WHO-Oral-Health-Fact-Sheet1/> (accessed June 15, 2018).
- Fosdick, L. S.; Stark, A. C. Solubility of tooth enamel in saliva at various pH levels. *J. Dent. Res.* **1939**, *18*, 417–430.
- Larsen, M. J.; Pearce, E. I. F. A computer program for correlating dental plaque pH values, cH⁺, plaque titration, critical pH, resting pH and the solubility of enamel apatite. *Arch. Oral Biol.* **1997**, *42*, 475–480.
- Larsen, M. J.; Nyvad, B. Enamel erosion by some soft drinks and orange juices relative to their pH, buffering effect and contents of calcium phosphate. *Caries Res.* **1999**, *33*, 81–87.
- Dawes, C. What is the critical pH and why does a tooth dissolve in acid? *J. Can. Dent. Assoc.* **2003**, *69*, 722–724.
- Hojo, S.; Komatsu, M.; Okuda, R.; Takahashi, N.; Yamada, T. Acid profiles and pH of carious dentin in active and arrested lesions. *J. Dent. Res.* **1994**, *73*, 1853–1857.
- Dean, H. T. Endemic Fluorosis and its Relation to Dental Caries. *Public Health Rep.* **1938**, *53*, 1443–1452.
- Dean, H. T.; Arnold, F. A.; Elvove, E. Domestic Water and Dental Caries. *Public Health Rep.* **1942**, *57*, 1155–1194.
- Schlueter, N.; Klimek, J.; Ganss, C. In vitro Efficacy of Experimental Tin- and Fluoride-Containing Mouth Rinses as Anti-Erosive Agents in Enamel. *J. Dent.* **2009**, *37*, 944–948.
- Ganss, C.; Neutard, L.; von Hinckeldej, J.; Klimek, J.; Schlueter, N. Efficacy of a Tin/Fluoride Rinse: A Randomized in situ Trial on Erosion. *J. Dent. Res.* **2010**, *89*, 1214–1218.
- Marinho, V. C. C.; Chong, L. Y.; Worthington, H. V.; Walsh, T. Fluoride Mouthrinses for Preventing Dental Caries in Children and Adolescents. *Cochrane Database Syst. Rev.* **2016**, No. CD002284.
- Featherstone, J. D. B.; ten Cate, J. M. Physicochemical Aspects of Fluoride-Enamel-Interactions. In *Fluoride in Dentistry*; Ekstrand, J., Fejerskov, O., Silverstone, L. M., Eds.; Munksgaard International Publishers: Copenhagen, 1988; pp 125–149.
- Lee, B.-S.; Chou, P.-H.; Chen, S.-Y.; Liao, H.-Y.; Chang, C.-C. Prevention of enamel demineralization with a novel fluoride strip: enamel surface composition and depth profile. *Sci. Rep.* **2015**, *5*, No. 13352.

- (14) Baig, A. A.; Faller, R. V.; Yan, J.; Ji, N.; Lawless, M.; Eversole, S. L. Protective effects of SnF₂—Part I. Mineral solubilisation studies on powdered apatite. *Int. Dent. J.* **2014**, *64*, 4–10.
- (15) Jones, S. B.; Rees, G. D.; Shellis, R. P.; Barbour, M. E. The Effect of Monoalkyl Phosphates and Fluoride on Dissolution of Hydroxyapatite, and Interactions with Saliva. *Caries Res.* **2013**, *47*, 355–363.
- (16) Choi, S.; Rhee, Y.; Park, J.-H.; Lee, G.-J.; Kim, K.-S.; Park, J.-H.; Park, Y.-G.; Park, H.-K. Effects of fluoride treatment on phosphoric acid-etching in primary teeth: An AFM observation. *Micron* **2010**, *41*, 498–506.
- (17) Kawasaki, A.; Suge, T.; Ishikawa, K.; Ozaki, K.; Matsuo, T.; Ebisu, S. Ammonium hexafluorosilicate increased acid resistance of bovine enamel and dentine. *J. Mater. Sci. Mater. Med.* **2005**, *16*, 461–466.
- (18) Parkinson, C. R.; Shahzad, A.; Rees, G. D. Initial stages of enamel erosion: An in situ atomic force microscopy study. *J. Struct. Biol.* **2010**, *171*, 198–302.
- (19) Kwon, K.-Y.; Wang, E.; Nofal, M.; Lee, S.-W. Microscopic Study of Hydroxyapatite Dissolution As Affected by Fluoride Ions. *Langmuir* **2011**, *27*, 5335–5339.
- (20) Zheng, J.; Xiao, F.; Qian, L. M.; Zhou, Z. R. Erosion behavior of human tooth enamel in citric acid solution. *Tribol. Int.* **2009**, *42*, 1558–1564.
- (21) de Leeuw, N. H. Resisting the Onset of Hydroxyapatite Dissolution through the Incorporation of Fluoride. *J. Phys. Chem. B* **2004**, *108*, 1809–1811.
- (22) de Leeuw, N. H. Computer simulations of structures and properties of the biomaterial hydroxyapatite. *J. Mater. Chem.* **2010**, *20*, 5376–5389.
- (23) Slepko, A.; Demkov, A. A. First principles study of hydroxyapatite surface. *J. Chem. Phys.* **2013**, *139*, No. 044714.
- (24) Müller, F.; Zeitz, C.; Mantz, H.; Ehses, K.-H.; Soldera, F.; Schmauch, J.; Hannig, M.; Hüfner, S.; Jacobs, K. Elemental depth profiling of fluoridated hydroxyapatite: Saving your dentition by the skin of your teeth? *Langmuir* **2010**, *26*, 18750–18759.
- (25) Faidt, T.; Zeitz, C.; Grandthyll, S.; Hans, M.; Hannig, M.; Jacobs, K.; Müller, F. Time Dependence of Fluoride Uptake in Hydroxyapatite. *ACS Biomater. Sci. Eng.* **2017**, *3*, 1822–1826.
- (26) Zeitz, C.; Faidt, T.; Grandthyll, S.; Hähl, H.; Thewes, N.; Spengler, C.; Schmauch, J.; Deckarm, M. J.; Gachot, C.; Natter, H.; Hannig, M.; Müller, F.; Jacobs, K. Synthesis of Hydroxyapatite Substrates: Bridging the Gap between Model Surfaces and Enamel. *ACS Appl. Mater. Interfaces* **2016**, *8*, 25848–25855.
- (27) Shirley, D. A. High-Resolution X-Ray Photoemission Spectrum of the Valence Bands of Gold. *Phys. Rev. B* **1972**, *5*, 4709–4714.
- (28) Yeh, J. J.; Lindau, I. Atomic Subshell Photoionization Cross Sections and Asymmetry Parameters: $1 \leq Z \leq 103$. *At. Data Nucl. Data Tables* **1985**, *32*, 1–155.
- (29) Jongebloed, W. L.; van den Berg, P. J.; Arends, J. The Dissolution of Single Crystals of Hydroxyapatite in Citric and Lactic Acids. *Calcif. Tissue Res.* **1974**, *15*, 1–9.
- (30) Moreno, E. C.; Aoba, T. Comparative Solubility Study of Human Dental Enamel, Dentin, and Hydroxyapatite. *Calcif. Tissue Int.* **1991**, *49*, 6–13.
- (31) Cutress, T. W. The inorganic composition and solubility of dental enamel from several specified population groups. *Arch. Oral Biol.* **1972**, *17*, 93–109.
- (32) Loskill, P.; Zeitz, C.; Grandthyll, S.; Thewes, N.; Müller, F.; Bischoff, M.; Herrmann, M.; Jacobs, K. Reduced Adhesion of Oral Bacteria on Hydroxyapatite by Fluoride Treatment. *Langmuir* **2013**, *29*, 5528–5533.

SUPPORTING INFORMATION

for

Effect of fluoride treatment on the acid-resistance of hydroxyapatite

Thomas Faidt, Andreas Friedrichs, Samuel Grandthyll, Christian Spengler, Karin Jacobs, Frank Müller*

Experimental Physics, Saarland University, 66123 Saarbrücken, Germany,

*Corresponding author. *Email address:* f.mueller@mx.uni-saarland.de (F. Müller)

Pages: S1–S3

Figures: S1: Height distributions of fluoridated HAp

S2: AFM micrographs and height distributions of areas of interest

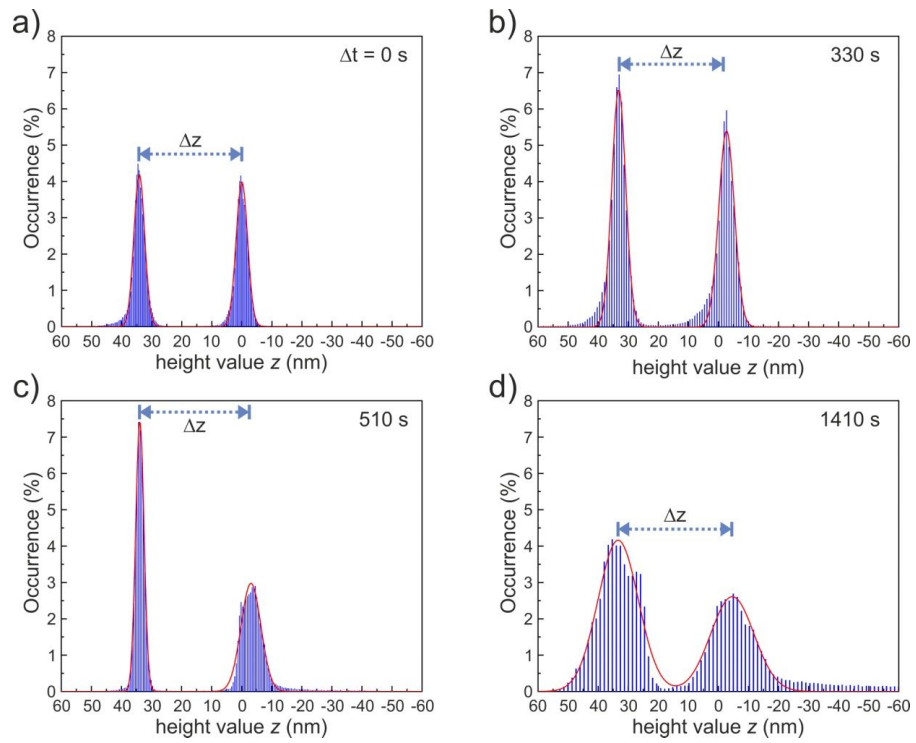


Figure S1: Typical height distributions of fluoridated HAp as extracted from the micrographs in Fig. 5 after a) 0 s, b) 330 s, c) 510 s and d) 1410 s of etching. Peaks at $z = 35$ nm represent the gold surface, peaks at lower z -values belong to the HAp surface.

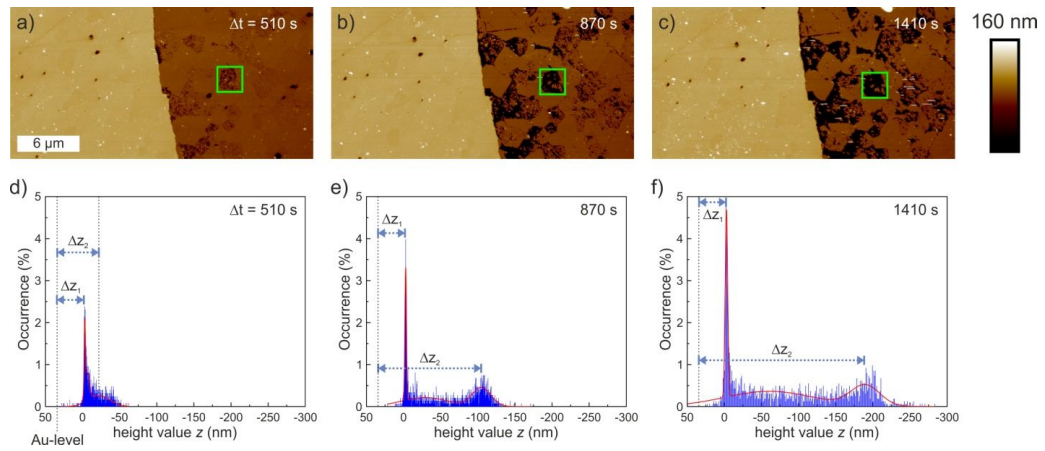


Figure S2: AFM micrographs (a – c) and height distributions (d – f) of the marked areas after 510 s (a + d), 870 s (b + e) and 1410 s (c + f) of etching to evaluate the ablation rate of quickly etching sites. The gold peak is not visible in the histograms because it is not in the specified area of interest (green box). However, its position is known from the data shown in fig. S1 and marked by a dotted line in the histograms at $z = 35$ nm.

IV: Enhanced Adhesion of *Streptococcus Mutans* to Hydroxyapatite After Exposure to Saliva

Authors: C. Spengler,¹ N. Thewes,¹ F. Nolle,¹ **T. Faidt**,¹ N. Umanskaya,² M. Hannig,² M. Bischoff,³ and K. Jacobs¹

¹Experimental Physics, Saarland University, 66123 Saarbrücken, Germany.

²Clinic of Operative Dentistry, Periodontology and Preventive Dentistry, Saarland University, 66421 Homburg, Germany.

³Institute of Medical Microbiology and Hygiene, Saarland University, 66421 Homburg, Germany.

Reprinted with permission from *J. Mol. Recognit.* 30 (2017), pp. e2615.

Copyright 2017 John Wiley & Sons, Ltd.

<https://doi.org/10.1002/jmr.2615>

Author contributions:

C. Spengler designed the experiments, achieved experimental results and wrote the manuscript. N. Thewes designed the experiments and wrote the manuscript. F. Nolle designed the experiments and achieved experimental results. T. Faidt and N. Umanskaya designed the experiments. M. Hannig directed scientific work. M. Bischoff and K. Jacobs directed scientific work and wrote the manuscript.

Abstract – *Streptococcus mutans* cells form robust biofilms on human teeth and are strongly related to caries incidents. Hence, understanding the adhesion of *S. mutans* in the human oral cavity is of major interest for preventive dentistry. In this study, we report on atomic force microscopy–based single-cell force spectroscopy measurements of *S. mutans* cells to hydroxyapatite surfaces. We observe for almost all measurements a significant difference in adhesion strength for *S. mutans* as well as for *Staphylococcus carnosus* cells. However, the increase in adhesion strength after saliva exposure is much higher for *S. mutans* cells compared to *S. carnosus* cells. Our results demonstrate that *S. mutans* cells are well adapted to their natural environment, the oral cavity. This ability promotes the biofilm-forming capability of that species and hence the production of caries-provoking acids. In consequence, understanding the fundamentals of this mechanism may pave a way towards more effective caries-reducing techniques.

SPECIAL ISSUE ARTICLE

Enhanced adhesion of *Streptococcus mutans* to hydroxyapatite after exposure to saliva[†]Christian Spengler¹  | Nicolas Thewes¹ | Friederike Nolle¹ | Thomas Faidt¹ | Natalia Umanskaya² | Matthias Hannig² | Markus Bischoff³ | Karin Jacobs¹¹Experimental Physics, Saarland University, Saarbrücken, Saarland, Germany²Clinic of Operative Dentistry, Periodontology and Preventive Dentistry, Saarland University, Homburg, Saarland, Germany³Institute of Medical Microbiology and Hygiene, Saarland University, Homburg, Saarland, Germany

Correspondence

Karin Jacobs, Experimental Physics, Saarland University, Saarbrücken, Saarland, Germany. Email: k.jacobs@physik.uni-saarland.de

Funding information

German Research Foundation (DFG), Grant/Award Number: SFB 1027

Abstract

Streptococcus mutans cells form robust biofilms on human teeth and are strongly related to caries incidents. Hence, understanding the adhesion of *S. mutans* in the human oral cavity is of major interest for preventive dentistry. In this study, we report on atomic force microscopy-based single-cell force spectroscopy measurements of *S. mutans* cells to hydroxyapatite surfaces. We observe for almost all measurements a significant difference in adhesion strength for *S. mutans* as well as for *Staphylococcus carnosus* cells. However, the increase in adhesion strength after saliva exposure is much higher for *S. mutans* cells compared to *S. carnosus* cells. Our results demonstrate that *S. mutans* cells are well adapted to their natural environment, the oral cavity. This ability promotes the biofilm-forming capability of that species and hence the production of caries-provoking acids. In consequence, understanding the fundamentals of this mechanism may pave a way towards more effective caries-reducing techniques.

KEYWORDS

hydroxyapatite, saliva, single-cell force spectroscopy, *Streptococcus mutans*

1 | INTRODUCTION

It is known for decades that *Streptococcus mutans* is very closely related to the development of caries and other diseases in the oral cavity.^{1–3} Furthermore, it can also enter the bloodstream through wounds in the oral cavity and travel from there through the body and even reach the coronary artery, where it can cause severe cardiovascular diseases.⁴ The main pathogenicity of this organism arises when the cell adheres to appropriate surfaces, since with this step, the formation of a biofilm is initiated.

The process of caries formation is thereby influenced by substratum (eg, enamel, fluoridated, or not) and saliva.^{5–8} On exposure to saliva, a proteinaceous surface coating—called pellicle—is formed almost immediately on all solid substrates.⁹ This conditioning layer changes the properties of the substrate. The nature of the chemical groups exposed at the surface mainly defines the adhesion forces.⁸

Most studies focus on the adhesion of oral bacteria to salivary agglutinin (SAG) that is adsorbed to the oral pellicle on tooth surfaces.^{10–12}

Additionally, it has been shown that the characteristics of biofilm formation by *S. mutans* depend on many parameters like for example oxygen content or the presence of specific enzymes in the bacterial cell.^{13,14} Next to other constituents, the salivary sucrose content increases adhesion to surfaces significantly and is also a key factor in the production of biofilms.¹⁵ Furthermore, by using genetically modified *S. mutans* cells, the function of many proteins in adhesion processes and biofilm formation on SAG was identified.^{10–12}

Atomic force microscopy (AFM)-based force spectroscopy offers a unique tool to quantitatively investigate crucial parameters of initial bacterial adhesion. By using this technique, cantilevers functionalized with specific proteins of the bacterial cell wall provide access to probe molecular interactions between these proteins and various substrate surfaces. For example, the binding between SAG and the P1 adhesin of *S. mutans*, which is crucial for adhesion, has been characterized and quantified.^{16,17}

For this AFM-based force spectroscopy study, we prepared cantilevers with single, viable bacterial cells to probe the interaction of the entire bacterial cell with the substratum dependent on a pretreatment of the cell.¹⁸ Thereby, substrate parameters are kept constant. For force spectroscopy, a controlled, low roughness of the substratum is a precondition, since on rough, natural teeth surfaces, the contact

[†]This article is published in Journal of Molecular Recognition as part of the virtual Special Issue AFM BioMed Porto 2016, edited by Susana Sousa, INEB|3S, Portugal and Pierre Parot, CEA, France, and Jean-Luc Pellequer, IBS, France.

area between bacterial cell and surface is unpredictable. Therefore, as a model tooth material with low roughness and still high biological relevance, we used pressed, sintered, and polished high-density pellets of hydroxyapatite (HAP), which is the mineral component of human tooth enamel.⁸

To highlight the adaption of *S. mutans* cells for the human oral cavity and salivary environments, we performed the exact same experiments with *Staphylococcus carnosus* cells. *Staphylococcus carnosus* is an apathogenic representative of the genus *Staphylococci* that is used in meat production and has no affinity for the oral cavity.^{19–22}

2 | MATERIALS AND METHODS

2.1 | Bacteria

Streptococcus mutans strain ATCC 25175 was cultured from a deep-frozen stock solution on mitis salivarius agar selective for this species for 3 days.^{23,24} For every experiment, 1 colony from these plates (not older than 2 wk) was transferred into 5 mL of sterile Todd Hewitt broth and cultured for 24 hours at 37°C under agitation (150 rpm). Afterwards, 40 μ L of this solution were transferred into 4 mL of fresh Todd Hewitt broth and cultured for another 16 hours at 37°C and 150 rpm resulting in an optical density at 600 nm of 0.2 to 0.3. To remove extracellular material, we washed cell suspensions as follows: 1 mL of the culture was centrifuged for 3 minutes at 17 000 \times g. Afterwards, the supernatant was replaced by fresh phosphate buffered saline (PBS) and vortexed for 10 seconds. Then, the procedure was repeated 2 more times and the final solution was stored at 4°C for not longer than 6 hours.

For comparison, we used the apathogenic, nonoral species *S. carnosus* strain TM300.^{19–22} These cells were grown from a deep-frozen stock solution on a blood agar plate for 3 days, and a fresh plate was used not longer than 2 weeks. Before every experiment, 1 colony was suspended in 5 mL tryptic soy broth and cultured overnight at 37°C and 150 rpm. From this solution, 40 μ L were inoculated in 4 mL fresh tryptic soy broth and grown for another 2.5 hours resulting in an optical density at 600 nm of 0.3 to 0.4. Then, 1 mL of this suspension was washed 3 times as described above and afterwards stored at 4°C for not longer than 6 hours.

2.2 | Surfaces

Hydroxyapatite pellets were produced by pressing and sintering of pure HAP powder (Sigma Aldrich, Steinheim, Germany) resulting in an overall density of more than 97% of the density of a single crystal, following a standard procedure published elsewhere.²⁵ To increase their

smoothness, we treated pellets with abrasive paper and polishing solutions of decreasing particle size (final polishing step with a diamond suspension of 30 nm particle size). Subsequently, the samples were etched in an ultrasonic bath for 7 seconds in sodium acetate buffer (pH 4.5) to remove residues from the final polishing step. Finally, HAP pellets feature a root mean square roughness of around 1 nm or less, as determined by AFM.²⁵

In preparation for every experiment, the HAP samples were cleaned for 5 minutes in an ultrasonic bath in an aqueous solution of 1% Mucisol (Merz Pharma, Frankfurt a. M., Germany). Afterwards, they were rinsed in an ultrasonic bath of pure deionized water (0.055 $\frac{\mu\text{s}}{\text{cm}}$, Thermo Fischer Scientific, Waltham, Massachusetts) for another 5 minutes and dried in a stream of pure nitrogen.

2.3 | Collecting of saliva

On overall 5 different days, about 5 mL each of saliva were collected from a volunteer with good oral health by chewing on parafilm (50% paraffin and 50% polyethylene), and spitting into a sterile test tube. The volunteer refrained from eating and drinking (except for water) for 1 hour after brushing the teeth with normal toothpaste. The saliva sample was collected 30 minutes after renewed tooth brushing without toothpaste. Afterwards, the saliva samples were filtered first through a 2 μ m and then through a 0.45 μ m filter. Subsequently, they were frozen to -20°C. After the collection of all 5 samples, they were thawed, mixed

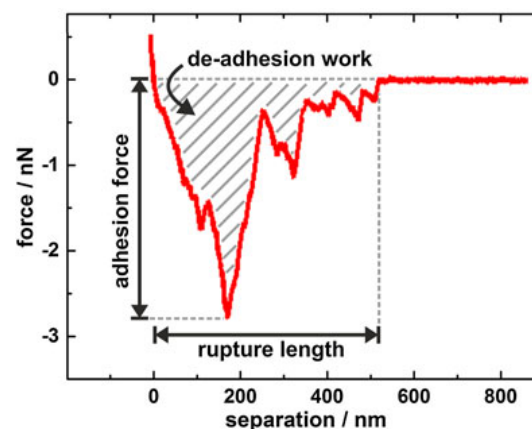


FIGURE 2 Retraction part of a typical force-distance curve, recorded with a single *Streptococcus mutans* cell on HAP displaying the main experimental measures

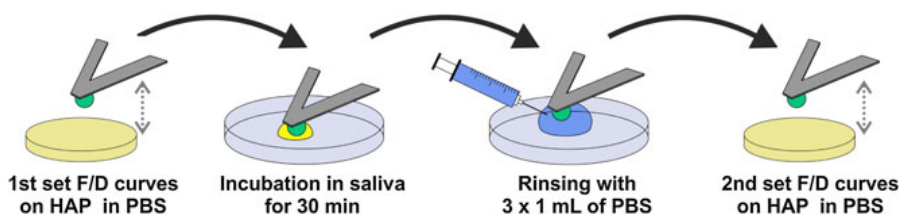


FIGURE 1 Scheme of the experimental procedure to expose a bacterial cell (green) to saliva

together, and again frozen to -20°C . For every experiment, a fresh sample was thawed and "vortexed" for 30 seconds to ensure proper mixing of all saliva components.

2.4 | Force-distance measurements

Force-distance measurements were performed on a Bioscope Catalyst (Bruker-Nano, Santa Barbara, California) with single bacterial cells immobilized on soft cantilevers, prepared by a method published earlier.¹⁸ We used tipless cantilevers (MLCT-0, Bruker) with a nominal spring constant of $0.03 \frac{\text{N}}{\text{m}}$ and a deflection sensitivity of $25 \frac{\text{nm}}{\text{V}}$. Cantilevers were calibrated before each set of experiments. The force trigger, which defines the maximum force with which the bacterial probe is pressed onto the substrate, was set to 300 pN, and the lateral distance between each single curve on the HAP surface was $1 \mu\text{m}$. For the influence of the binding kinetics to be tested, the force trigger can be held constant for a certain time, called surface delay (SD) time.^{26–28} We used SD of 0, 2, and 5 seconds. Thereby, 0 second stands for a very short contact time of some ms.²⁹ For every bacterial cell, first 3 sets of 40 force-distance curves (1 set for each SD time) were collected in PBS (pH 7.3) on a bare HAP surface. Next, the bacterial cell—still immobilized on the cantilever—was covered with $50 \mu\text{L}$ of filtered saliva for 30 minutes. Then, the cantilever was washed 3 times with 1 mL of pure PBS each to remove possible leftovers of the saliva solution. The thickness of the salivary layer remaining on the dopamin-coated cantilever can be estimated to be in the

range of some tens of nanometers at the maximum.³⁰ Since this is orders of magnitude smaller than the diameter of the bacterial cell, the cell itself serves as a spacer so that this salivary layer cannot make contact to the HAP surface in following force-distance measurements. Afterwards, the second 3 sets of force-distance curves were collected with the exact same parameters as before (see Figure 1). Subsequently, the measured force-distance curves were quantified for adhesion force (minimal force during retraction), rupture length (distance between cell and HAP surface at which the last connection breaks), and de-adhesion work (area under the retraction curve), as shown²⁶ in Figure 2.

Altogether, 10 individual *S. mutans* cells and 5 individual *S. carnosus* cells were tested, and with 1 and the same bacterial cell, in sum 240 force-distance curves on the HAP surface were taken (120 before and 120 after saliva exposure). A possible deterioration due to the measurement can be excluded, since with increasing number of scans, no systematic change in the force curves (eg, a decreasing adhesion) can be observed. This is in accordance with earlier studies.²⁶

2.5 | Statistical analysis

Statistical analysis of all data distributions before and after saliva exposure was performed using a Mann-Whitney-U test of the software Matlab (MathWorks, Natick, Massachusetts). Significance levels are indicated in the graphs by asterisks denoting the following levels of significance: *: $p < .05$, **: $p < .01$, and ***: $p < .001$.

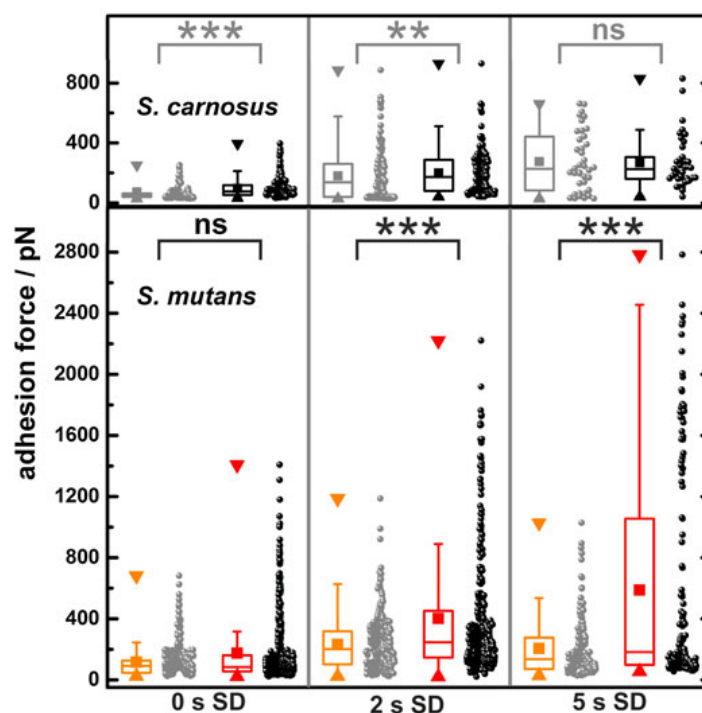


FIGURE 3 Adhesion forces of *Streptococcus mutans* (lower panel) and *Staphylococcus carnosus* cells (upper panel) to hydroxyapatite pellets before (light color) and after (dark color) saliva exposure for different surface delay (SD) times. For details of the box-and-whisker representation, see text

3 | RESULTS

Figure 3 depicts adhesion forces of 10 individual *S. mutans* and 5 individual *S. carnosus* cells before and after exposure to saliva. Three different SD times have been tested to study the influence of contact time to adhesion strength. Overall, the adhesion forces cover a range of 0 to 2800 pN for *S. mutans* cells and only 0 to 950 pN for *S. carnosus* cells. Within the same surface delay panel of Figure 3, *S. mutans* cells develop stronger adhesion forces after saliva exposure for SD times from 2 seconds onwards. Comparatively, *S. carnosus* cells exhibit much smaller differences in adhesion force before and after exposure. For this trend to be displayed, the results in Figure 3 are shown as box-and-whisker plots, where the median is marked by the horizontal line in the box and the whiskers are defined as 1.5 times the extent of the interquartile range (IQR).³¹ These measures quantify what is already visible by the eye: For both bacterial species, for $SD > 0$ seconds, larger adhesion forces (median as well as average) are recorded, but the median is not significantly affected by saliva treatment. For *S. mutans* cells, however, mean adhesion force, IQR as well as the whiskers gain clearly in size by saliva exposure. In some force-distance measurements, the treatment causes an especially enforced adhesion.

Similarly, as displayed in Figure 4, the rupture lengths of *S. mutans* cells are especially increased after inoculation: No matter of the applied SD time, mean values of the rupture length increase by almost an order of magnitude after treatment. Before, rupture lengths are in the range of some tens of nanometers, whereas after the saliva treatment, they

increase up to several hundreds of nanometers with a mean value of around 200 nm and maxima up to 1200 nm. For *S. carnosus* cells, rupture lengths on the HAP surface are in general smaller than for *S. mutans* cells and the relative increase after saliva treatment is much smaller, only about a factor of 2.

An even stronger effect of saliva treatment can be observed by examining the work that is necessary to remove the entire bacterial cell from the surface (see Figure 5). For *S. mutans* cells, the mean value (as well as the IQR and the whiskers) is strongly increased: From a mean value of around 10 000 $k_B T$ at 0-second SD to a mean value of roughly 30 000 $k_B T$ at 5-second SD. Remarkably, at closer inspection, data points seem to develop a bimodal distribution at long SD times. Thereby, the median of the de-adhesion work stays almost unchanged.

To highlight this trend, Figure 6 shows histograms of the de-adhesion work of *S. mutans* and *S. carnosus* cells on HAP after the exposure to saliva for different SD times. With increasing surface delay, a second regime of large values of de-adhesion work occurs for *S. mutans* cells. Simultaneously, the portion of force-distance curves with a de-adhesion work below 20 000 $k_B T$ decreases with increasing SD time. For $SD = 5$ seconds, the mean value of the second regime in the histogram is located at values of the de-adhesion work of around 110 000 $k_B T$. It is interesting to note that for *S. mutans*, the different adhesion strengths become directly apparent in the way the shape of the force-distance curves changes with increasing SD times (8 curves are exemplarily shown as inset to Figure 6): All curves display local minima, and the deepest is taken as a measure for the adhesion force. However, for a SD of 5 seconds, the deepest minimum in the retraction

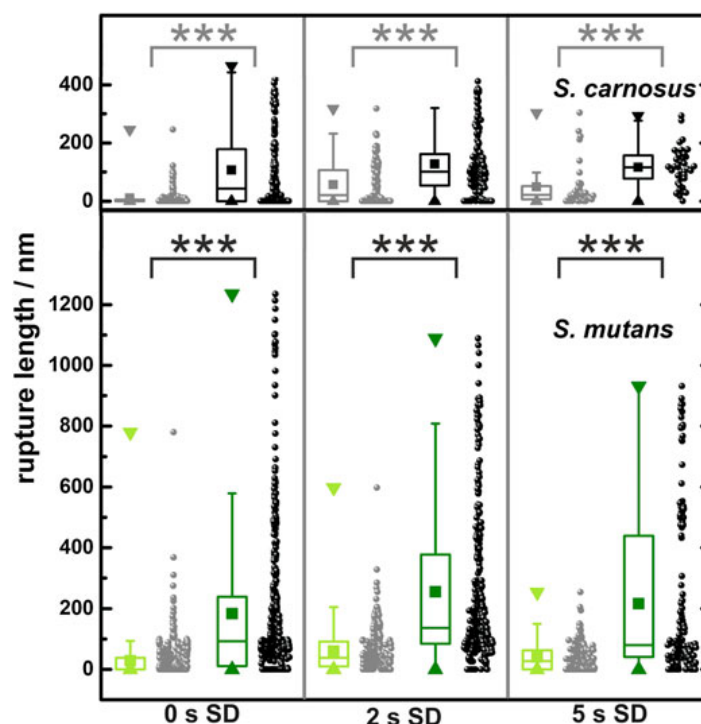


FIGURE 4 Rupture lengths for *Streptococcus mutans* (lower panel) and *Staphylococcus carnosus* cells (upper panel) removed from hydroxyapatite pellets before (light color) and after (dark color) saliva exposure for different surface delay (SD) times. For details of the box-and-whisker representation, see text

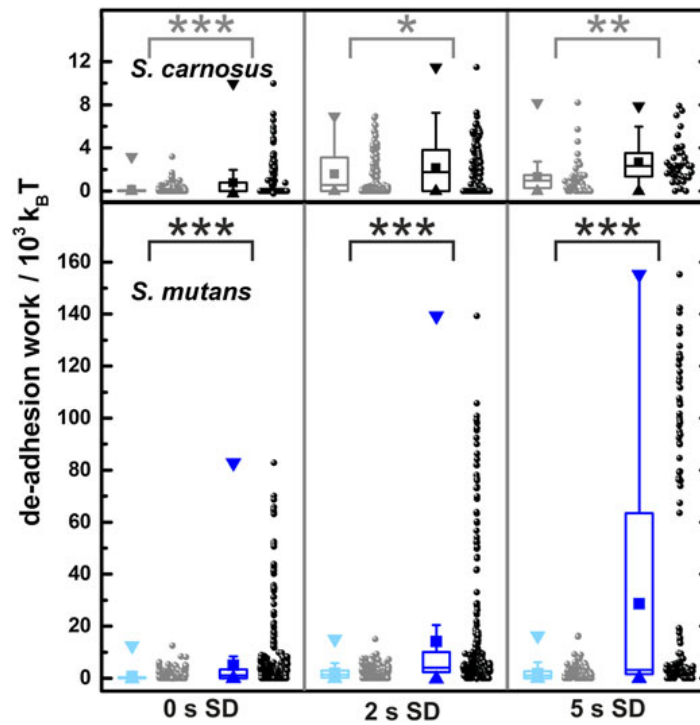


FIGURE 5 De-adhesion work of *Streptococcus mutans* (lower panel) and *Staphylococcus carnosus* cells (upper panel) on hydroxyapatite pellets before (light color) and after (dark color) saliva exposure for different surface delay (SD) times. For details of the box-and-whisker representation, see text. Note the 4-fold stretched energy scale in the upper panel

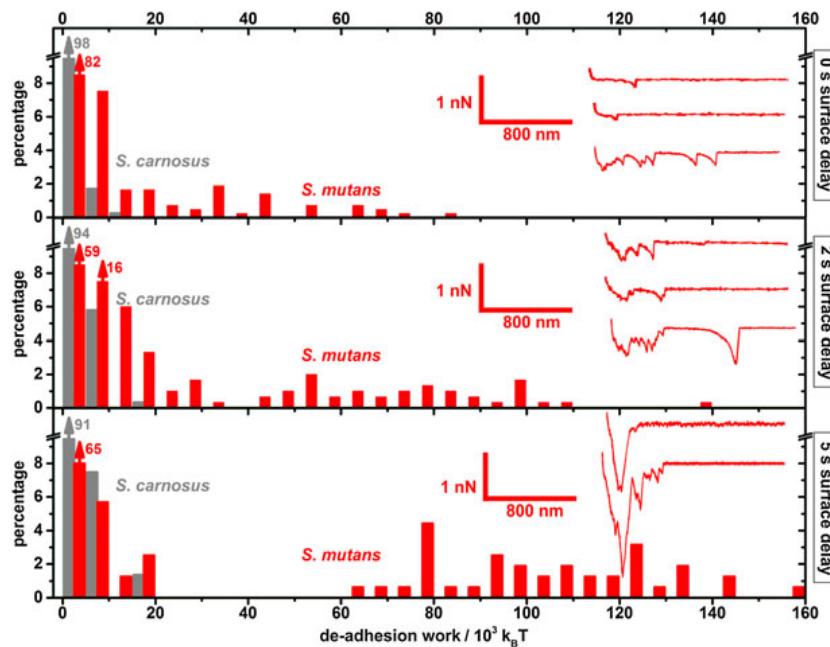


FIGURE 6 De-adhesion work histograms of *Streptococcus mutans* (red) and *Staphylococcus carnosus* cells (gray) for different surface delay times after saliva exposure. As insets, exemplary force-distance curves of *S. mutans* cells are shown. Note, that all distributions are significantly different from each other with a significance level $p < .001$

curve is much deeper than following local minima, whereas for curves with smaller SD times, all occurring local minima are in the same range of forces.

For *S. carnosus* cells, the scenario is completely different (see gray bars in Figure 6): The de-adhesion work is more than 1 order of magnitude smaller than for *S. mutans* cells. Also, for all SD times, the histogram of the de-adhesion work features only 1 regime and this is located at quite low values of around 10 000 $k_B T$.

4 | DISCUSSION

Bacterial cells in the human mouth always run the risk of getting washed out, ie, of getting swallowed. Therefore, the evolutionary success of mouth colonizing cells relies first of all on their ability to adhere in the oral environment. Here, we investigated the adhesion strength of cells of the mouth colonizing species *S. mutans* to HAP pellets before and after exposure of the cells to human saliva using AFM-based single-cell force spectroscopy. Our results demonstrate that the strength of adhesion between *S. mutans* cells and HAP increases significantly and strongly after exposure of the cells to saliva. In contrast, treating *S. carnosus* cells (whose natural habitat is not the human mouth) in saliva increases the cells' adhesive strength to HAP pellets only slightly. Hence, *S. mutans* cells exhibit a specific mechanism that enhances their adhesion in the human oral environment. This mechanism may be a result of the evolutionary adaption of this bacterial species to its natural habitat, the human oral cavity. Moreover, our study demonstrates that for a firm adhesion of *S. mutans* cells to HAP surfaces, it is not necessary that SAG is present on the substratum, rather, even the exposure of the bacterial cell to a salivary environment is sufficient.

Open questions are why adhesion is enhanced by saliva inoculation and why *S. mutans* cells are especially responsive to the treatment. This study focusses on the former. The observation can be explained by the common notion how bacterial adhesion proceeds: The adhesion process relies on the consecutive binding of bacterial cell wall macromolecules to a substratum.^{32,33} The binding strength of a single contact point cannot be altered by a saliva treatment of the bacterial cell. Therefore, saliva treatment must increase the number of contact points, for instance, by a larger number of macromolecules that tether to the surface. Two ways are possible to accomplish the latter: either certain salivary components link to the bacterial cell wall via *S. mutans*-specific surface molecules (or domains) or *S. mutans* produces additional cell wall macromolecules when exposed to its natural salivary environment.

We can name some properties of this additional macromolecules, using results of this study: In force-distance curves, the adhesion force value is defined as the minimum force during retraction. The distance at which this point appears is related to the mechanical properties—in particular the length—of the contact forming macromolecules. In our measurements, the minimal force is usually located at separating distances of less than 200 nm (see insets in Figure 6). Hence, adhesion forces are dominated by molecules with an untensioned length of less than 200 nm that tether to the surface. These forces, however, are only slightly influenced by the saliva treatment. In contrast, the rupture lengths feature a strong increase after saliva inoculation. This implies

that the additional macromolecules that contribute to the adhesion after saliva treatment are longer than the surface macromolecules responsible for adhesion before saliva treatment. The effect of saliva treatment has the strongest impact on the de-adhesion work. This is likely the result of the combination of 2 effects, the slight increase in adhesion forces as well as the significantly larger rupture lengths.

The adhesion strength moreover increases with SD time. This trend can be observed for many different bacterial force-distance curves.²⁶ After saliva treatment, longer SD times can additionally amplify the increase in adhesion force because additional macromolecules have more time to find a suitable position to tether to the HAP surface. This means that for a longer SD time, more new macromolecules find such a binding site and therefore, the increase in adhesion force due to the salivary treatment even grows with longer SD times. In contrast, SD times do not cause longer rupture lengths, because in this case, it is sufficient that few (or in the extreme case only a single) additional, long macromolecules tether to the surface. For an adequately high number of additional, long macromolecules, already the initial contact between bacterial cell and surface leads to such a binding event and hence, an additional contact time does not have an influence.

It is also possible that for longer SD times not only more bonds originate but also existing bonds develop a stronger binding to the surface. This phenomenon, called bond strengthening, has been measured for *Streptococci* as well as for *Staphylococci*.^{34,35} However, in the present study, this effect cannot be the primary reason for enhanced adhesion because bond strengthening usually appears when specific interactions between binding molecules of the cell and molecules on the surface are involved. In our case, although, the substratum is a bare, smooth HAP surface, where no specific binding is expected. Furthermore, bond strengthening is usually observed for contact times notably longer than the 5 seconds of this study. Yet, it was not possible with the present setup to apply longer SD times while keeping the force trigger constant. It shall be probed in the future if for much longer SD times, most data will fall into the second regime of the de-adhesion work histogram.

5 | CONCLUSIONS

In this study, we have analyzed the adhesion properties of *S. mutans* cells to HAP surfaces. To monitor the adhesion process, AFM-based single-cell force spectroscopy was used on ultra smooth, high-density HAP pellets. It has been shown that adhesion force, rupture length, and de-adhesion work increase significantly when the cell has been inoculated in human saliva compared to adhesion without salivary treatment. Thereby, rupture length and de-adhesion work are notably enlarged, which leads to the interpretation that especially long macromolecules contribute to this. These macromolecules either stem from the saliva or are produced by *S. mutans* cells, stimulated by the contact to saliva. By comparing identical measurements of *S. mutans* and *S. carnosus* cells, it has been shown that the adaption to a salivary environment is a particular property of *S. mutans* cells and is far less pronounced for *S. carnosus* cells. Future studies may now further analyze saliva properties and identify salivary components that are responsible for this enhanced adhesion. That way, new pathways may open up in caries prevention by applying saliva-influencing agents after tooth brushing.

ACKNOWLEDGMENT

The study has been funded by the German Research Foundation (DFG) within the framework of SFB 1027.

REFERENCES

- Hamada S, Slade HD. Biology, immunology, and cariogenicity of *Streptococcus mutans*. *Microbiol Rev*. 1980;44(2):331–384.
- Loesche WJ. Role of *Streptococcus mutans* in human dental decay. *Microbiol Rev*. 1986;50(4):353–380.
- Mitchell TJ. The pathogenesis of Streptococcal infections: from tooth decay to meningitis. *Nature Rev Microbiol*. 2003;1:219–230.
- Abranches J, Zeng L, Bélanger M, et al. Invasion of human coronary artery endothelial cells by *Streptococcus mutans* OMZ175. *Oral Microbiol Immunol*. 2009;24:141–145.
- Selwitz RH, Ismail AI, Pitts NB. Dental caries. *Lancet*. 2007;369:51–59.
- Takahashi N, Nyvad B. Caries ecology revisited: microbial dynamics and the caries process. *Caries Res*. 2008;42(6):409–418. <https://doi.org/10.1159/000159604>.
- Filоче S, Wong L, Sissons CH. Oral biofilms: Emerging concepts in microbial ecology. *J Dent Res*. 2010;89(1):8–18. <https://doi.org/10.1177/0022034509351812>.
- Loskill P, Zeitz C, Grandthyll S, et al. Reduced adhesion of oral bacteria on hydroxyapatite by fluoride treatment. *Langmuir*. 2013;29(18):5528–5533. <https://doi.org/10.1021/la4008558>.
- Hannig C, Hannig M. The oral cavity - a key system to understand substratum-dependent bioadhesion on solid surfaces in man. *Clin Oral Investig*. 2009;13(2):123–139. <https://doi.org/10.1007/s00784-008-0243-3>.
- Ray CA, Gfell LE, Buller TL, Gregory RL. Interactions of streptococcus mutans fimbria-associated surface proteins with salivary components. *Clin Diagn Lab Immunol*. 1999;6(3):400–404.
- Yoshida A, Ansai T, Takehara T, Kuramitsu HK. LuxS-based signaling affects streptococcus mutans biofilm formation. *Appl Environ Microbiol*. 2005;71(5):2372–2380.
- Miller JH, Avilés-Reyes A, Scott-Anne K, et al. The collagen binding protein cnm contributes to oral colonization and cariogenicity of *Streptococcus mutans* OMZ175. *Infect Immun*. 2015;83(5):2001–2010. <https://doi.org/10.1128/IAI.03022-14>.
- Ahn S-J, Burne RA. Effects of oxygen on biofilm formation and the AtlA autolysin of *Streptococcus mutans*. *J Bacteriol*. 2007;189:6293–6032. doi:10.1128/JB.00546-07.
- Ahn S-J, Ahn S-J, Wen ZT, Brady LJ, Burne RA. Characteristics of biofilm formation by *Streptococcus mutans* in the presence of saliva. *Infect Immun*. 2008;76(9):4259–4268.
- Costa EM, Silva S, Távora FK, Pintado MM. Study of the effects of chitosan upon *Streptococcus mutans* adherence and biofilm formation. *Anaerobe*. 2013;20:27–30. <https://doi.org/10.1016/j.anaerobe.2013.02.002>.
- Brady LJ, Piacentini DA, Crowley PJ, Oyston PCF, Bleiweis AS. Differentiation of salivary agglutinin-mediated adherence and aggregation of mutans streptococci by use of monoclonal antibodies against the major surface adhesin P1. *Infect Immun*. 1992;60(3):1008–1017.
- Sullan RMA, Li JK, Crowley PJ, Brady LJ, Dufrène YF. Binding forces of *Streptococcus mutans* P1 adhesin. 2015;9(2):1448–1460. <https://doi.org/10.1021/nn5058886>.
- Thewes N, Loskill P, Spengler C, Hümbert S, Bischoff M, Jacobs K. A detailed guideline for the fabrication of single bacterial probes used for atomic force spectroscopy. *Eur Phys J E Soft Matter*. 2015;38(12):140. <https://doi.org/10.1140/epje/i2015-15140>.
- Schleifer KH, Fischer U. Description of a new species of the genus *Staphylococcus*: *Staphylococcus carnosus*. *Int J Syst*. 1982;32(2):153–156.
- Barriere C, Leroy-Sétrin S, Talon R. Characterization of catalase and superoxide dismutase in *Staphylococcus carnosus* 833 strain. *J Appl Microbiol*. 2001;91:514–516.
- Rosenstein R, Nerz C, Biswas L, Resch A. Genome analysis of the meat starter culture bacterium *Staphylococcus carnosus* TM300. *Appl Environ Microbiol*. 2009;75(3):811–822. <https://doi.org/10.1128/AEM.01982-08>.
- Rosenstein R, Götz F. Genomic differences between the food-grade *Staphylococcus carnosus* and pathogenic *Staphylococcal* species. *Int J Med Microbiol*. 2010;300:104–108. <https://doi.org/10.1016/j.ijmm.2009.08.014>.
- Gold OG, Jordan HV, Van Houte J. A selective medium for *Streptococcus mutans*. *J Microbiol Methods*. 1973;18:1357–1364.
- Coykendall AL. Proposal to elevate the subspecies of *Streptococcus mutans* to species status, based on their molecular composition. *Int J Syst Bacteriol*. 1977;27(1):26–30.
- Zeitz C, Faidt T, Grandthyll S, et al. Synthesis of hydroxyapatite substrates: bridging the gap between model surfaces and enamel. *Appl Mater Inter*. 2016;8(39):25848–25855. <https://doi.org/10.1021/acsami.6b10089>.
- Thewes N, Loskill P, Jung P, et al. Hydrophobic interaction governs unspecific adhesion of *Staphylococci*: a single cell force spectroscopy study. *Beilstein J Nanotechnol*. 2014;5:1501–1512. <https://doi.org/10.3762/bjnano.5.163>.
- Zeng G, Müller T, Meyer RL. Single-cell force spectroscopy of bacteria enabled by naturally derived proteins. *Langmuir*. 2014;30(14):4019–4025. <https://doi.org/10.1021/la404673q>.
- Herman-Bausier P, El-Kirat-Chatel S, Foster TJ, Geoghegan JA, Dufrène YF. *Staphylococcus aureus* fibronectin-binding protein A mediates cell-cell adhesion through low-affinity homophilic bonds. *mBio*. 2015;6(3):e00413–15.
- Beaussart A, El-Kirat-Chatel S, Herman P, et al. Single-cell force spectroscopy of probiotic bacteria. *Biophys J*. 2013;104:1886–1892.
- Macakova L, Yakubov GE, Plunkett MA, Stokes JR. Influence of ionic strength changes on the structure of pre-adsorbed salivary films. A response of a natural multi-component layer. *Coll Surf B*. 2010;77(1):31–39. <https://doi.org/10.1016/j.colsurfb.2009.12.022>.
- McGill R, Tukey JW, Larsen WA. Variations of box plots. *Am Stat*. 1978;32(1):12–16. <https://doi.org/10.2307/2683468>.
- Thewes N, Thewes A, Loskill P, et al. Stochastic binding of *Staphylococcus aureus* to hydrophobic surfaces. *Soft Matter*. 2015;11(46):8913–9046. <https://doi.org/10.1039/c5sm00963d>.
- Song L, Hou J, van der Mei HC, Veeragowda DH, Busscher HJ, Sjollem J. Antimicrobials influence bond stiffness and detachment of oral bacteria. *J Dent Res*. 2016;95(7):793–799. <https://doi.org/10.1177/0022034516634631>.
- van der Mei HC, Rustema-Abbing M, de Vries J, Busscher HJ. Bond strengthening in oral bacterial adhesion to salivary conditioning films. *Appl Environ Microbiol*. 2008;74(17):5511–5515.
- Boks NP, Busscher HJ, van der Mei HC, Norde W. Bond-strengthening in staphylococcal adhesion to hydrophilic and hydrophobic surfaces using atomic force microscopy. *Langmuir*. 2008;24(22):12990–12994.

How to cite this article: Spengler C, Thewes N, Nolle F, Faidt T, Umanskaya N, Hannig M, Bischoff M, Jacobs K. Enhanced adhesion of *Streptococcus mutans* to hydroxyapatite after exposure to saliva. *J Mol Recognit*. 2017;30:e2615. <https://doi.org/10.1002/jmr.2615>

V: Photoactivatable Mussel-Based Underwater Adhesive Proteins by an Expanded Genetic Code

Authors: M. Hauf,¹ F. Richter,² T. Schneider,¹ **T. Faidt**,³ B. M. Martins,⁴ T. Baumann,¹ P. Durkin,¹ H. Dobbek,⁴ K. Jacobs,³ A. Möglich,^{2,5} and N. Budisa¹

¹Institut für Chemie, Technische Universität Berlin, 10623 Berlin, Germany.

²Institut für Biologie, Biophysikalische Chemie, Humboldt-Universität zu Berlin, 10099 Berlin, Germany.

³Experimental Physics, Saarland University, 66123 Saarbrücken, Germany.

⁴Institut für Biologie, Strukturbioogie/Biochemie, Humboldt-Universität zu Berlin, 10099 Berlin, Germany.

⁵Lehrstuhl für Biochemie, Universität Bayreuth, 95440 Bayreuth, Germany.

Reprinted with permission from *ChemBioChem* 18 (2017), pp. 1819–1823.

Copyright 2017 Wiley-VCH Verlag GmbH & Co. KGaA, Weinheim.

<https://doi.org/10.1002/cbic.201700327>

Author contributions:

M. Hauf designed the experimental aaRS library, designed and selected aaRS variants, performed experiments and wrote the manuscript. F. Richter performed the computational design process, designed the experimental aaRS library, designed experiments, and wrote the manuscript. T. Schneider performed chemical synthesis of ONB-Dopa isomers and wrote the manuscript. T. Faidt performed atomic force microscopy based force spectroscopy and wrote the manuscript. B. M. Martins performed protein crystallization and structure determination, and wrote the manuscript. T. Baumann designed experiments and wrote the manuscript. P. Durkin performed chemical synthesis and assisted in writing the manuscript. H. Dobbek directed structure determination and assisted in writing the manuscript. K. Jacobs directed atomic force microscopy studies and assisted in writing the manuscript. A. Möglich directed experimental work and assisted in writing the manuscript. N. Budisa directed experimental work and wrote the manuscript.

Abstract – Marine mussels exhibit potent underwater adhesion abilities under hostile conditions by employing 3,4-dihydroxyphenylalanine (DOPA)-rich mussel adhesive proteins (MAPs). However, their recombinant production is a major biotechnological challenge. Herein, a novel strategy based on genetic code expansion has been developed by engineering

efficient aminoacyl-transfer RNA synthetases (aaRSs) for the photocaged noncanonical amino acid *ortho*-nitrobenzyl DOPA (ONB-DOPA). The engineered ONB-DOPARS enables in vivo production of MAP type 5 site-specifically equipped with multiple instances of ONB-DOPA to yield photocaged, spatiotemporally controlled underwater adhesives. Upon exposure to UV light, these proteins feature elevated wet adhesion properties. This concept offers new perspectives for the production of recombinant bioadhesives.

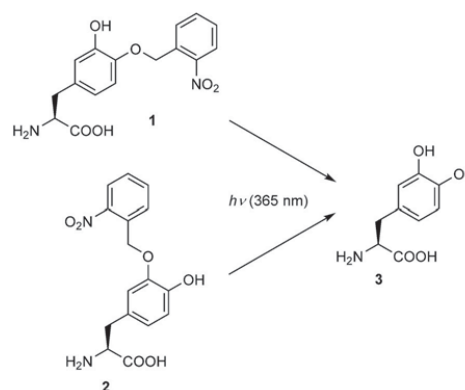


Photoactivatable Mussel-Based Underwater Adhesive Proteins by an Expanded Genetic Code

Matthias Hauf,^[a] Florian Richter,^[b] Tobias Schneider,^[a] Thomas Faidt,^[c] Berta M. Martins,^[d] Tobias Baumann,^[a] Patrick Durkin,^[a] Holger Dobbek,^[d] Karin Jacobs,^[c] Andreas Möglich,^[b, e] and Nediljko Budisa^{*[a]}

Marine mussels exhibit potent underwater adhesion abilities under hostile conditions by employing 3,4-dihydroxyphenylalanine (DOPA)-rich mussel adhesive proteins (MAPs). However, their recombinant production is a major biotechnological challenge. Herein, a novel strategy based on genetic code expansion has been developed by engineering efficient aminoacyl-transfer RNA synthetases (aaRSs) for the photocaged non-canonical amino acid *ortho*-nitrobenzyl DOPA (ONB-DOPA). The engineered ONB-DOPARS enables *in vivo* production of MAP type 5 site-specifically equipped with multiple instances of ONB-DOPA to yield photocaged, spatiotemporally controlled underwater adhesives. Upon exposure to UV light, these proteins feature elevated wet adhesion properties. This concept offers new perspectives for the production of recombinant bio-adhesives.

Marine mussels fabricate an underwater adhesive with great potential for technological and biomedical applications in wet conditions.^[1,2] The key element for adhesion is the amino acid 3,4-dihydroxyphenylalanine (DOPA; Scheme 1), owing to its versatile catechol side-chain chemistry, formed in nature post-translationally through tyrosine (Tyr) hydroxylation.^[3–6] Inspired by the remarkable ability of mussels to efficiently adhere to various types of surfaces, DOPA-containing peptides and polymers were synthesized that showed adhesive, coating, or self-healing properties,^[2,7–10] with applications as antibacterial agents and medical transplants.^[11,12] The mussel adhesive proteins (MAPs) located in the byssus thread, which have high



Scheme 1. Structures of DOPA and photocaged derivatives. *p*-ONB-DOPA (1) and *m*-ONB-DOPA (2) can be photocleaved to yield DOPA (3).

DOPA contents of up to 30 mol%, have particularly attracted attention.^[13] Due to low extraction yields from mussels, much effort has been devoted to recombinant production of MAPs. This includes enzymatic Tyr hydroxylation *in vitro*,^[14] coexpression of tyrosinase,^[15] and eukaryotic expression platforms.^[16] However, most approaches suffer from low hydroxylation efficiency and specificity or low protein yields.^[17] Residue-specific replacement^[18,19] of Tyr by DOPA, exploiting the substrate promiscuity of *Escherichia coli* tyrosyl-tRNA synthetase (*EcTyrRS*), has been reported for MAP types 3 and 5,^[17] but is limited by the poor activation of DOPA by *EcTyrRS*, accompanied by Tyr incorporation (Figure S1 in the Supporting Information), and impaired cell growth due to proteome-wide DOPA incorporation.

Herein, we present an alternative strategy to recombinantly produce MAPs by expanding the genetic code with a photocaged DOPA derivative through an engineered *Methanocaldococcus jannaschii* TyrRS (*MjTyrRS*). In recent years, orthogonal pairs (o-pairs) that consist of an engineered aminoacyl-tRNA synthetase (aaRS) and its cognate tRNA have been created. Commonly at amber (TAG) stop codons, noncanonical amino acids (ncAAs) can be site-specifically incorporated in live cells, ranging from bacteria to higher eukaryotes.^[20,21] As mussel protein adhesion depends on cooperative effects, efficient multi-site incorporation of DOPA (and analogues) is mandatory for recombinant production. Recently, *E. coli* strains lacking release factor 1 (RF1)^[22] and genomic amber codons^[23,24] have been

[a] Dr. M. Hauf, T. Schneider, Dr. T. Baumann, Dr. P. Durkin, Prof. Dr. N. Budisa
Institut für Chemie, Technische Universität Berlin
Müller-Breslau-Strasse 10, 10623 Berlin (Germany)
E-mail: nediljko.budisa@tu-berlin.de

[b] Dr. F. Richter, Prof. Dr. A. Möglich
Institut für Biologie, Biophysikalische Chemie
Humboldt-Universität zu Berlin, Unter den Linden 6
10099 Berlin (Germany)

[c] T. Faidt, Prof. Dr. K. Jacobs
Experimental Physics, Saarland University
Campus E2 9, 66123 Saarbrücken (Germany)

[d] Dr. B. M. Martins, Prof. Dr. H. Dobbek
Institut für Biologie, Strukturbiologie/Biochemie
Humboldt-Universität zu Berlin, Unter den Linden 6
10099 Berlin (Germany)

[e] Prof. Dr. A. Möglich
Lehrstuhl für Biochemie, Universität Bayreuth
Universitätsstrasse 30, 95440 Bayreuth (Germany)

Supporting information for this article can be found under:
<https://doi.org/10.1002/cbic.201700327>.

developed, leveraging the production of proteins site-specifically endowed with multiple ncAAs through amber suppression.

We aimed to develop an aaRS for ribosomal incorporation of our newly developed photocaged DOPA derivative *o*-nitrobenzyl DOPA (ONB-DOPA;^[25] Scheme 1). This strategy circumvents the recently encountered problem of having to evolve an aaRS that discriminates between DOPA and similar Tyr,^[26,27] and to avoid DOPA auto-oxidation, which has been shown to impair adhesive properties.^[13,28] Additionally, the ONB group, which is cleaved upon irradiation with $\lambda = 365$ nm light and frequently used to produce caged proteins,^[29–31] allows for spatiotemporal control of adhesive catechol side chain of DOPA. With an ONB-DOPA-specific aaRS, we then aim to recombinantly produce photoactivatable *Mytilus galloprovincialis* MAP type 5 (foot protein-5; fp-5), with ONB-DOPA in multiple positions, as a high-potential adhesive for applications in wet conditions.

Current methods of selecting novel aaRSs from site-saturation or random mutagenesis libraries often yield low-activity enzymes,^[32–34] which are a major obstacle for efficient multi-site ncAA incorporation.^[35,36] We hypothesize that the selection of inefficient aaRSs can be attributed to substantial under-sampling of relevant active-site sequence space arising from limited *E. coli* transformation efficiency. Thus, we employed established computational design methods^[37–39] to generate a *MjTyrRS* active-site library with focused diversity at 17 positions, including second-shell residues (Table S1).

The library was subjected to alternating rounds of *in vivo* double-sieve selection, as previously described,^[20] in the presence or absence of *p*- and *m*-ONB-DOPA. Caged by the ONB group, both regioisomers yield DOPA through photocleavage. After three rounds of selection, we observed sequence convergence into three variants (ONB-DOPARS-1–3) harboring nine or ten mutations (Table S1). They enabled ncAA-dependent bacterial growth on selective plates through amber suppression in the chloramphenicol acetyltransferase gene (Figure S2), with ONB-DOPARS-1 supporting strongest growth in the presence, and least growth in the absence, of the ncAA.

To assess the ncAA incorporation efficiency and fidelity, separate chemical synthesis strategies for *p*-/*m*-ONB-DOPA were developed. Furthermore, reporter constructs were employed that consisted of an N-terminal His₆-SUMO (SUMO: small ubiquitin-like modifier) sequence fused to a superfolder green fluorescent protein (sfGFP)-Strep II sequence, carrying one or five amber mutations at permissive loop positions (Figure S3). Protein expression and amber suppression efficiencies were evaluated by SUMO-sfGFP intact-cell fluorescence and purified protein yields. Despite the presence of endogenous RF1 in *E. coli* BL21(DE3), we observed highly efficient incorporation of *m*-ONB-DOPA into SUMO-sfGFP(1TAG) through ONB-DOPARS-1, with intact-cell fluorescence at the same level as those of both wild-type (WT, that is, amber-free) SUMO-sfGFP and SUMO-sfGFP(1TAG) with Tyr incorporated through *MjTyrRS* (Figure 1A). In addition, SDS-PAGE and western blot analyses of purified proteins showed a near-complete absence of truncated products in the presence of *m*-ONB-DOPA, which suggested that the ONB-DOPARS-1 o-pair was able to outcompete endog-

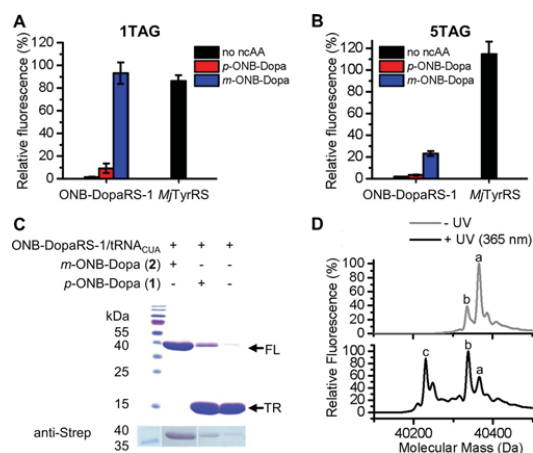


Figure 1. Characterization of ncAA incorporation by ONB-DOPARS-1. Intact-cell fluorescence of A) SUMO-sfGFP(1TAG) produced in *E. coli* BL21(DE3), and B) SUMO-sfGFP(5TAG) produced in *E. coli* C321.ΔA.exp(DE3). Fluorescence is normalized to strain-specific WT SUMO-sfGFP intensity and to the optical density at $\lambda = 600$ nm (OD_{600}) of the bacterial culture. Data represent mean \pm standard deviation (s.d.) of biological triplicates. C) SDS-PAGE and western blot analysis of purified SUMO-sfGFP(1TAG) produced in *E. coli* BL21(DE3) by using ONB-DOPARS-1 in the presence or absence of *p*-/*m*-ONB-DOPA (FL: full-length, TR: truncated). D) Deconvoluted ESI-MS spectra of SUMO-sfGFP(1TAG) protein equipped with *m*-ONB-DOPA before (gray) and after irradiation (black). SUMO-sfGFP(1 ONB-DOPA) (a): calcd: 40366.6 Da, obsd: 40366.7 Da. Peak b) is consistent with reduction of the nitro group to an amine: calcd: 40336.6 Da, obsd: 40337.8 Da. SUMO-sfGFP(1 DOPA) (c): calcd: 40231.5 Da, obsd: 40232.3 Da.

enous RF1 (Figure 1C). Moreover, in the absence of the ncAA, we only detected minute amounts of full-length (FL) protein; this demonstrates the exquisite selectivity of the aaRS. In contrast, fluorescence data indicate only moderate incorporation efficiency of *p*-ONB-DOPA into SUMO-sfGFP(1TAG) by ONB-DOPARS-1 ($\approx 10\%$ of WT). Notably, installation of five instances of *m*-ONB-DOPA into SUMO-sfGFP(5TAG) constructs still showed a signal of 23%, compared with that of WT (Figure 1B). With 61 and 23 mg L⁻¹ of SUMO-sfGFP equipped with one or five instances of *m*-ONB-DOPA, respectively, purified protein yields (Table S2 and Figure S5) are markedly above common protein yields with ncAA incorporation through *MjTyrRS*-based o-pairs.^[20,22] Mass spectrometry confirmed incorporation of *m*-ONB-DOPA into SUMO-sfGFP constructs (Figure S4) and showed a decaging efficiency of $> 50\%$ after protein exposure to $\lambda = 365$ nm monochromatic light for 45 min (Figure 1D). As recently described for different ONB-caged ncAAs,^[40] partial reduction of the nitro group to an amine was observed (Figure S4), which interfered with the decaging reaction. As these data demonstrate, we have developed an efficient aaRS for *m*-ONB-DOPA that provides a good starting point for the production of photocaged MAPs and other biopolymers equipped with multiple instances of the ncAA.

To elucidate the substrate binding mode and efficiency of ONB-DOPARS-1, we cocrystallized the aaRS with the ncAA (Figure 2 and Figure S6). The crystal structure shows that the

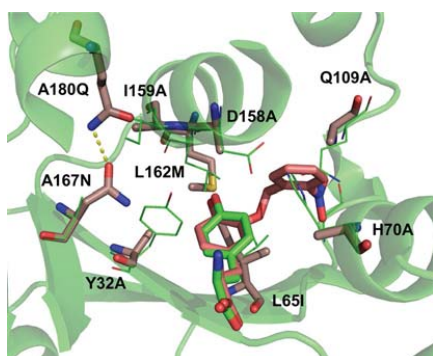


Figure 2. Crystal structure of ONB-DOPARS-1 in complex with *m*-ONB-DOPA. Mutations H70A, Q109A, and D158A expand the aaRS active site for the ONB moiety. A180Q and A167N form a hydrogen-bond interaction. Side chains are shown as sticks with brown for carbon, blue for nitrogen, and red for oxygen. WT residues of the *Mj*TyrRS–Tyr complex (PDB ID: 1J1U) are shown with carbon in green.

ONB group fits into a hydrophobic pocket created by H70A, Q109A, and D158A. Moreover, the substrate is anchored through its carboxyl and amino groups in a similar way to that seen in the WT *Mj*TyrRS–Tyr complex (PDB ID: 1J1U).^[41] Hydrogen bonds between the hydroxyl group of Tyr and side chains Y32 and D158 are abolished in ONB-DOPARS-1 (Y32A, D158A). A167N and A180Q form a new hydrogen bond and pack into the space vacated by Y32A, which is likely to be required to ensure discrimination against the native Tyr substrate.

Next, we chose fp-5 as the target protein due to its key role in the underwater adhesion of mussels.^[13] Naturally located in the adhesive plaque in direct contact to the substratum, fp-5 displays high DOPA contents of about 30 mol%. These traits make it attractive for the production of photoactivatable underwater adhesives through multi-site incorporation of *m*-ONB-DOPA or other photocaged DOPA analogues. To facilitate soluble-protein production, a maltose binding protein (MBP) sequence with a tobacco etch virus (TEV) protease cleavage site was N-terminally fused to an fp-5-His₆ sequence. Tyr codons in the fp-5 gene were replaced with amber codons at five, ten, or all 19 sites (Note 1 in the Supporting Information). After finding evidence for proteolytic degradation of the protein in genomically recoded *E. coli* C321,^[23] we chose *E. coli* BL21(DE3) strain derivative B-95.ΔA^[24] as the host organism, in which RF1 was likewise eliminated. Western blotting of purified protein variants confirmed the installation of five and ten instances of *m*-ONB-DOPA into fp-5, whereas only minute amounts of fp-5(19TAG) were detectable (Figure 3A). Although poor expression yields were reported for fp-5 in *E. coli*,^[14] we obtained 6 and 1 mg L⁻¹ of fp-5(5TAG) and fp-5(10TAG), respectively, in the presence of the ncAA, compared with 18 mg L⁻¹ of WT fp-5 (19 Tyr residues). Only fp-5(19TAG) showed clearly reduced yields in the low-microgram range per liter of culture volume. The drop in yield from 10 to 19 amber codons might be caused by inefficient interaction of the ncAA-tRNA with elongation factor Tu,^[42] endogenous factors beyond RF1 competition-limiting

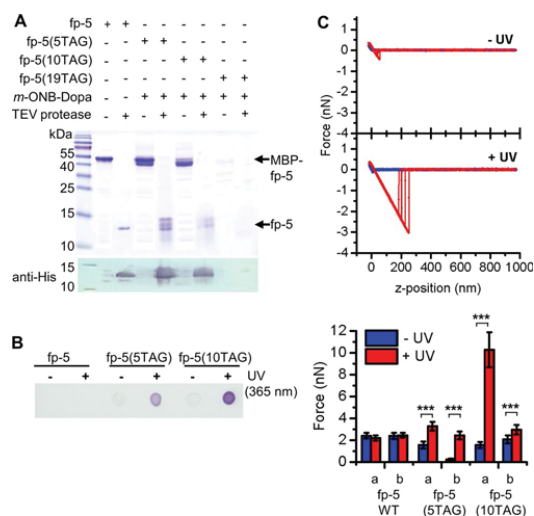


Figure 3. Analysis of purified fp-5 variants. A) SDS-PAGE and western blot analysis of MBP-fp-5 variants carrying 5, 10, or 19 instances of *m*-ONB-DOPA produced in *E. coli* B95.ΔA. Purified proteins were digested with TEV protease to yield insoluble fp-5 variants. B) NBT staining of fp-5 variants. After TEV protease treatment, equal amounts of purified protein were spotted before (-) or after (+) irradiation with $\lambda = 365$ nm light. Due to low production yields, fp-5(19TAG) was not tested. C) AFM analysis of tips functionalized with fp-5 variants on mica surfaces under wet conditions (pH 4.6). Top: Overlay of five typical FD curves of fp-5(5TAG) interacting with a mica surface before and after irradiation. Blue and red curves depict approach and retraction signals, respectively. Bottom: Force values of two tips (a, b) functionalized with different fp-5 variants before (blue) and after irradiation (red). Data represent mean \pm s.d. of 100 FD curves; significance is designated by symbols * $p < 10^{-3}$, ** $p < 10^{-6}$, *** $p < 10^{-9}$.

amber suppression,^[36] or structural clashes of adjacent ncAA residues. Production and photocleavage of fp-5 variants carrying the ncAA at five or ten sites were verified by mass spectrometry (Figure S7). In addition, we confirmed decaying by the redox-cycling nitro blue tetrazolium (NBT), which selectively stained DOPA- or dopaquinone-containing proteins.^[43] Only irradiated fp-5 variants showed pronounced staining (Figure 3B).

In order to demonstrate the underwater adhesive potential of photocaged MAPs, we employed atomic force microscopy (AFM)-based spectroscopy previously used to study DOPA-mediated wet adhesion.^[3] AFM tips were functionalized with MAPs by using a lysine-reactive acetal poly(ethylene glycol) (PEG)-*N*-hydroxysuccinimide (NHS) cross-linker.^[44] Force-distance (FD) curves of functionalized tips were measured in sodium acetate buffer (10 mM, pH 4.6) on mica surfaces before and after irradiation with UV light (Figure 3C). Whereas adhesion forces of WT fp-5 did not change significantly through irradiation in any measurement, we observed up to 12- and 6.5-fold increased adhesion of fp-5(5TAG) and fp-5(10TAG), respectively, following UV light exposure of the same tip. In some experiments, photocaged fp-5 failed to show elevated adhesion after irradiation, presumably due to incomplete decaging or

heterogeneous coupling of fp-5 through one or several of its 13 internal Lys residues. The former is substantiated by the observation that prolonged UV-light exposure led to elevated adhesion forces of fp-5(10TAG). To verify that DOPA accounted for the increased adhesion, we tested unmodified and amino-functionalized tips. Both showed adhesion in the low-pN range; in each case unaffected by UV light (Figure S8). Thus, our data for fp-5 equipped with five and ten instances of *m*-ONB-DOPA provide evidence for the feasibility of spatiotemporal control of DOPA-mediated underwater adhesion. This emphasizes the high potential of recombinantly produced photocaged bioadhesives.

Taken together, we have developed efficient aaRSs for ribosomal incorporation of the novel compound *m*-ONB-DOPA. To the best of our knowledge, ONB-DOPARS-1 enabled the first production of MAPs site-specifically equipped with multiple caged DOPA moieties through orthogonal translation. Computational enzyme design methodologies were used in this study to redesign the *M*TyrRS active site towards recognizing photocaged DOPA. They are able to rapidly scan through vast sequence spaces and filter large numbers of sequences that are incompatible with substrate binding or active-site organization. Thus, computation allows the consideration of residues not restricted to the few first shell positions. We believe computational design to broadly aid the development of potent aaRSs for desirable ncAAs. Such enzymes will become even more important as recent advancements, such as RF1 removal and amber codon emancipation,^[23,24] facilitate installation of ncAAs at multiple protein sites. Whereas genetic code expansion has traditionally focused on single-position modifications, multi-site incorporation of ncAAs will allow the biosynthesis of proteins with nCAA-derived physiochemical properties. Although in-depth characterization of the wet adhesive characteristics of fp-5 variants is underway, our force spectroscopy data exemplify the adhesive potential of recombinantly produced MAPs with *m*-ONB-DOPA at multiple sites. Compared with synthetic mussel-inspired polymers, the MAPs produced herein take advantage of the adhesion-optimized protein sequence, including a favorable lysine–DOPA interplay,^[4] and combine it with spatiotemporal control over the adhesive nature of the catechol group. These photoactivatable biomimetic proteins could thus serve as potent adhesives in water or high-moisture settings with applications in industry and biomedicine.^[1,2] Further investigation will reveal the contribution of individual (ONB-)DOPA sites to the overall adhesive potential, and thus, facilitate the production of variants optimized for site-specific incorporation of ncAAs. Our general concept of producing spatiotemporally controllable adhesives provides a valuable alternative to current MAP production strategies. Moreover, it can be extended in two ways: first, DOPA analogues photocaged with alternative chemical handles can be employed; second, other well-expressing protein scaffolds with multiple sites permissive for nCAA installation, such as elastin-like polypeptides,^[35] can be combined with our novel aaRS and ONB-DOPA. Together, these hold great promise for the production of diverse sets and large quantities of photocaged mussel-inspired biomaterials.

Acknowledgements

We thank Abhishek Chatterjee (Boston College) and Kensaku Sakamoto (RIKEN Center for Life Science Technologies) for providing plasmid pULTRA, and *E. coli* strain B-95.ΔA, respectively. We thank Roderich Süßmuth and Sascha Ramm (TU Berlin) for access to and support with MALDI-MS. Ludwig Sinn (TU Berlin) gave excellent assistance in aaRS purification. We thank Friederike Klemke and Tobias Werther (HU Berlin) for help in protein crystallization and data collection. We acknowledge access to beamlines of the BESSY II storage ring (Berlin) through the Joint Berlin MX-Laboratory sponsored by Helmholtz Zentrum Berlin für Materialien und Energie, Freie Universität Berlin, Humboldt-Universität zu Berlin, Max-Delbrück-Centrum, and the Leibniz-Institut für Molekulare Pharmakologie. M.H. was funded by the Beilstein-Institut zur Förderung der Chemischen Wissenschaften with a Ph.D. scholarship. T.B. acknowledges funding by the EU (SYNPEP-TIDE). Additional funding was provided by Deutsche Forschungsgemeinschaft grant RI2468/1 (F.R.), Sofja-Kovalevskaya Award (A.M.) by the Alexander-von-Humboldt Foundation, and by the Einstein Foundation Berlin grant IPF-2012-148 (F.R. and A.M.). N.B., A.M., and H.D. acknowledge funding through the cluster of excellence UniCat—EXC 314. T.F. and K.J. were supported by the German Research Foundation (DFG) in the framework of the Collaborative Research Centre SFB1027 “Physical modeling of nonequilibrium processes in biological systems”.

Conflict of Interest

The authors declare no conflict of interest.

Keywords: biomimetic synthesis · computational chemistry · mussel adhesive protein · photochemistry · scanning probe microscopy · synthetases

- [1] E. Dolgin, *Nat. Med.* **2013**, *19*, 124–125.
- [2] N. K. Kaushik, N. Kaushik, S. Pardeshi, J. G. Sharma, S. H. Lee, E. H. Choi, *Mar. Drugs* **2015**, *13*, 6792–6817.
- [3] H. Lee, N. F. Scherer, P. B. Messersmith, *Proc. Natl. Acad. Sci. USA* **2006**, *103*, 12999–13003.
- [4] G. P. Maier, M. V. Rapp, J. H. Waite, J. N. Israelachvili, A. Butler, *Science* **2015**, *349*, 628–632.
- [5] S. C. T. Nicklisch, J. H. Waite, *Biofouling* **2012**, *28*, 865–877.
- [6] H. G. Silverman, F. F. Roberto, *Mar. Biotechnol.* **2007**, *9*, 661–681.
- [7] B. P. Lee, P. B. Messersmith, J. N. Israelachvili, J. H. Waite, *Annu. Rev. Mater. Res.* **2011**, *41*, 99–132.
- [8] H. Lee, S. M. Dellatore, W. M. Miller, P. B. Messersmith, *Science* **2007**, *318*, 426–430.
- [9] B. K. Ahn, S. Das, R. Linstadt, Y. Kaufman, N. R. Martinez-Rodriguez, R. Mirshafian, E. Kesselman, Y. Talmon, B. H. Lipshutz, J. N. Israelachvili, J. H. Waite, *Nat. Commun.* **2015**, *6*, 8663.
- [10] M. Krogsgaard, M. A. Behrens, J. S. Pedersen, H. Birkedal, *Biomacromolecules* **2013**, *14*, 297–301.
- [11] J. Guo, W. Wang, J. Hu, D. Xie, E. Gerhard, M. Nisic, D. Shan, G. Qian, S. Zheng, J. Yang, *Biomaterials* **2016**, *85*, 204–217.
- [12] C. E. Brubaker, H. Kissler, L.-J. Wang, D. B. Kaufman, P. B. Messersmith, *Biomaterials* **2010**, *31*, 420–427.
- [13] E. W. Danner, Y. Kan, M. U. Hammer, J. N. Israelachvili, J. H. Waite, *Biochemistry* **2012**, *51*, 6511–6518.
- [14] D. S. Hwang, Y. Gim, H. J. Yoo, H. J. Cha, *Biomaterials* **2007**, *28*, 3560–3568.

- [15] Y. S. Choi, Y. J. Yang, B. Yang, H. J. Cha, *Microb. Cell Fact.* **2012**, *11*, 139.
- [16] S. Lim, K. R. Kim, Y. S. Choi, D.-K. Kim, D. Hwang, H. J. Cha, *Biotechnol. Prog.* **2011**, *27*, 1390–1396.
- [17] B. Yang, N. Ayyadurai, H. Yun, Y. S. Choi, B. H. Hwang, J. Huang, Q. Lu, H. Zeng, H. J. Cha, *Angew. Chem. Int. Ed.* **2014**, *53*, 13360–13364; *Angew. Chem.* **2014**, *126*, 13578–13582.
- [18] J. A. Johnson, Y. Y. Lu, J. A. Van Deventer, D. A. Tirrell, *Curr. Opin. Chem. Biol.* **2010**, *14*, 774–780.
- [19] N. Budisa, *Angew. Chem. Int. Ed.* **2004**, *43*, 6426–6463; *Angew. Chem.* **2004**, *116*, 6586–6624.
- [20] C. C. Liu, P. G. Schultz, *Annu. Rev. Biochem.* **2010**, *79*, 413.
- [21] R. J. Ernst, T. P. Krogager, E. S. Maywood, R. Zanchi, V. Beránek, T. S. Elliott, N. P. Barry, M. H. Hastings, J. W. Chin, *Nat. Chem. Biol.* **2016**, *12*, 776–778.
- [22] D. B. F. Johnson, J. Xu, Z. Shen, J. K. Takimoto, M. D. Schultz, R. J. Schmitz, Z. Xiang, J. R. Ecker, S. P. Briggs, L. Wang, *Nat. Chem. Biol.* **2011**, *7*, 779–786.
- [23] M. J. Lajoie, A. J. Rovner, D. B. Goodman, H.-R. Aerni, A. D. Haimovich, G. Kuznetsov, J. A. Mercer, H. H. Wang, P. A. Carr, J. A. Mosberg, N. Rohland, P. G. Schultz, J. M. Jacobson, J. Rinehart, G. M. Church, F. J. Isaacs, *Science* **2013**, *342*, 357–360.
- [24] T. Mukai, H. Hoshi, K. Ohtake, M. Takahashi, A. Yamaguchi, A. Hayashi, S. Yokoyama, K. Sakamoto, *Sci. Rep.* **2015**, *5*, 9699.
- [25] T. Schneider, J. Martin, P. M. Durkin, V. Kubyshekin, N. Budisa, *Synthesis* **2017**, *49*, 2691–2699.
- [26] A. K. Antonczak, Z. Simova, I. T. Yonemoto, M. Bochtler, A. Piasecka, H. Czapinska, A. Brancale, E. M. Tippmann, *Proc. Natl. Acad. Sci. USA* **2011**, *108*, 1320–1325.
- [27] L. Alfonta, Z. Zhang, S. Uryu, J. A. Loo, P. G. Schultz, *J. Am. Chem. Soc.* **2003**, *125*, 14662–14663.
- [28] J. Yu, W. Wei, E. Danner, R. K. Ashley, J. N. Israelachvili, J. H. Waite, *Nat. Chem. Biol.* **2011**, *7*, 588–590.
- [29] E. Arbely, J. Torres-Kolbus, A. Deiters, J. W. Chin, *J. Am. Chem. Soc.* **2012**, *134*, 11912–11915.
- [30] B. J. Wilkins, S. Mariomni, D. D. Young, J. Liu, Y. Wang, M. L. Di Salvo, A. Deiters, T. A. Cropp, *Biochemistry* **2010**, *49*, 1557–1559.
- [31] A. Deiters, D. Groff, Y. Ryu, J. Xie, P. G. Schultz, *Angew. Chem. Int. Ed.* **2006**, *45*, 2728–2731; *Angew. Chem.* **2006**, *118*, 2794–2797.
- [32] P. O'Donoghue, J. Ling, Y.-S. Wang, D. Söll, *Nat. Chem. Biol.* **2013**, *9*, 594–598.
- [33] S. Nehring, N. Budisa, B. Wiltschi, *PLoS One* **2012**, *7*, e31992.
- [34] M. J. Lajoie, D. Söll, G. M. Church, *J. Mol. Biol.* **2016**, *428*, 1004–1021.
- [35] M. Amiram, A. D. Haimovich, C. Fan, Y. Wang, H.-R. Aerni, I. Ntai, D. W. Moonan, N. J. Ma, A. J. Rovner, S. H. Hong, N. L. Kelleher, A. L. Goodman, M. C. Jewett, D. Söll, J. Rinehart, F. J. Isaacs, *Nat. Biotechnol.* **2015**, *33*, 1272–1279.
- [36] Y. Zheng, M. J. Lajoie, J. S. Italia, M. A. Chin, G. M. Church, A. Chatterjee, *Mol. Biosyst.* **2016**, *12*, 1746–1749.
- [37] A. Leaver-Fay, M. Tyka, S. M. Lewis, O. F. Lange, J. Thompson, R. Jacak, K. Kaufman, P. D. Renfrew, C. A. Smith, W. Sheffler, et al., *Methods Enzymol.* **2011**, *487*, 545–574.
- [38] F. Richter, A. Leaver-Fay, S. D. Khare, S. Bjelic, D. Baker, *PLoS One* **2011**, *6*, e19230.
- [39] F. Richter, R. Blomberg, S. D. Khare, G. Kiss, A. P. Kuzin, A. J. T. Smith, J. Gallaher, Z. Pianowski, R. C. Helgeson, A. Grjasnow, et al., *J. Am. Chem. Soc.* **2012**, *134*, 16197–16206.
- [40] D. P. Nguyen, M. Mahesh, S. J. Elsässer, S. M. Hancock, C. Uttamapinant, J. W. Chin, *J. Am. Chem. Soc.* **2014**, *136*, 2240–2243.
- [41] T. Kobayashi, O. Nureki, R. Ishitani, A. Yaremchuk, M. Tukalo, S. Cusack, K. Sakamoto, S. Yokoyama, *Nat. Struct. Biol.* **2003**, *10*, 425–432.
- [42] J. Guo, C. E. Melançon, H. S. Lee, D. Groff, P. G. Schultz, *Angew. Chem. Int. Ed.* **2009**, *48*, 9148–9151; *Angew. Chem.* **2009**, *121*, 9312–9315.
- [43] M. A. Paz, R. Flückiger, A. Boak, H. M. Kagan, P. M. Gallop, *J. Biol. Chem.* **1991**, *266*, 689–692.
- [44] L. Wildling, B. Unterauer, R. Zhu, A. Rupprecht, T. Haselgrübler, C. Rankl, A. Ebner, D. Vater, P. Pollheimer, E. E. Pohl, P. Hinderdorfer, H. J. Gruber, *Bioconjug. Chem.* **2011**, *22*, 1239–1248.

Manuscript received: June 20, 2017

Accepted manuscript online: June 26, 2017

Version of record online: August 1, 2017

CHEMBIOCHEM

Supporting Information

Photoactivatable Mussel-Based Underwater Adhesive Proteins by an Expanded Genetic Code

Matthias Hauf,^[a] Florian Richter,^[b] Tobias Schneider,^[a] Thomas Faidt,^[c] Berta M. Martins,^[d] Tobias Baumann,^[a] Patrick Durkin,^[a] Holger Dobbek,^[d] Karin Jacobs,^[c] Andreas Möglich,^[b, e] and Nediljko Budisa*^[a]

cbic_201700327_sm_miscellaneous_information.pdf

Table of Contents

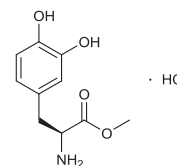
Experimental Procedures.....	3
Results and Discussion.....	22
SI Figures	22
SI Tables.....	30
SI Note 1. DNA sequences of constructs used in this study	32
References	34
Author Contributions.....	34

Experimental Procedures

Chemical synthesis. *m*-ONB-Dopa and *p*-ONB-Dopa were synthesized (see below).

Synthesis of *m*-ONB-Dopa ((S)-3-(2'-nitrobenzyl)-dihydroxyphenylalanine) and *p*-ONB-Dopa ((S)-4-(2'-nitrobenzyl)-dihydroxyphenylalanine)

1) Synthesis of (S)-dihydroxyphenylalanine (DOPA)-methylester hydrochloride

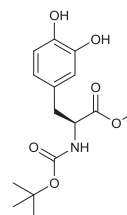


This compound was synthesized according to literature.^[1]

¹H-NMR (500 MHz, DMSO-*d*₆): δ 8.96 (s, 1H), 8.93 (s, 1H), 8.55 (b, 3H), 6.67 (d, *J* = 8.0 Hz, 1H), 6.59 (d, *J* = 2.1 Hz, 1H), 6.45 (dd, *J* = 8.0, 2.1 Hz, 1H), 4.10 (t, *J* = 6.5 Hz, 1H), 3.68 (s, 3H), 2.99 (dd, *J* = 14.1, 5.8 Hz, 1H), 2.91 (dd, *J* = 14.1, 7.0 Hz, 1H).

NMR-Data is consistent with literature.^[1]

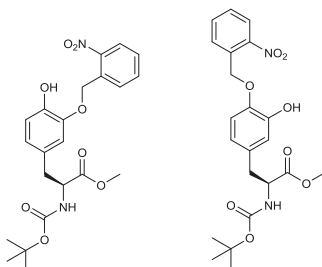
2) Synthesis of (S)-N-Boc-dihydroxyphenylalanine-methylester



The compound was synthesized according to literature with the slight modification.^[1] In addition the crude product was purified by silica column chromatography (*n*-hexane:ethylacetate 1:1). Evaporation of the solvents gave the product as a white solid (5.70 g, 18.3 mmol, 72.1 %).

¹H-NMR (500 MHz, DMSO-*d*₆): δ 8.71 (s, 1H), 8.66 (s, 1H), 7.11 (d, *J* = 7.9 Hz, 1H), 6.63-6.60 (m, 2H), 6.44 (d, *J* = 7.9, 1.8 Hz, 1H), 4.08-4.02 (m, 1H), 3.59 (s, 3H), 2.78 (dd, *J* = 13., 5.3 Hz, 1H), 2.67 (dd, *J* = 13.7, 9.5 Hz, 1H), 1.34 (s, 9H)

NMR-Data is consistent with literature.^[1]

3) Synthesis of (S)-3-(2'-nitrobenzyl)-N-Boc-dihydroxyphenylalanine-methylester and (S)-4-(2'-nitrobenzyl)-N-Boc-dihydroxyphenylalanine-methylester

5.70 g (18.3 mmol) of (S)-N-Boc-dihydroxyphenylalanine-methylester was dissolved in 50 ml of degassed acetone and 5.06 g of potassium carbonate (36.6 mmol), 3.95 g of 2-nitrobenzylbromide (18.3 mmol) and 274 mg of sodium iodide (1.83 mmol) were added under nitrogen atmosphere. The reaction mixture was stirred at roomtemperature for 24 hours. After this the reaction mixture was neutralized with 1M aqueous HCl and the solvent mixture was evaporated under reduced pressure. To the residue 20 ml of ethylacetate and 20 ml of water were added. The phases were separated and the aqueous phase was extracted with ethylacetate (2x20 ml). The organic phases were combined, dried over sodium sulfate and the solvent was removed under reduced pressure. The product was purified by silica column chromatography (dichloromethane:methyl-*tert*-butyl ether 10:1). The separation of a mixture of the two regioisomers from double *o*NB-protected material was achieved easily. The mixture of the regioisomers can be isolated as a yellow oil (2.5 g). The isolation of the pure regioisomers was achieved under the same conditions using multiple consecutive columns, since both isomers have similar R_f values. R_f (3-(2'-nitrobenzyl) derivative =0.7/ 4-(2'-nitrobenzyl) derivative = 0.65). Yield of 3-(2'-nitrobenzyl) derivative 1.55g (yellowish solid)// Yield of 4-(2'-nitrobenzyl) derivative 970 mg (yellowish solid).

(S)-3-(2'-nitrobenzyl)oxy-4-hydroxy-N-Boc-phenylalanine-methylester

¹H-NMR (500 MHz, CDCl₃) δ ppm: 8.18 (dd, *J*=8.1, 1.1 Hz, 1 H), 7.73 - 7.78 (m, 1 H), 7.70 (ddd, *J*=7.7, 1.0 Hz, 1 H), 7.54 (ddd, *J*=7.7 Hz, 7.7 Hz, 1.2 Hz, 1 H), 6.89 (d, *J*=8.1 Hz, 3 H), 6.68 (dd, *J*=8.1, 1.7 Hz, 1 H), 6.63 (d, *J*=1.8 Hz, 1 H), 5.53 (d, *J*=2.6 Hz, 2 H), 5.09-4.91 (m, 1 H), 4.65-4.46 (m, 1 H), 3.06 - 2.88 (m, 2 H), 3.68 (s, 3 H) 1.41 (s, 9 H)

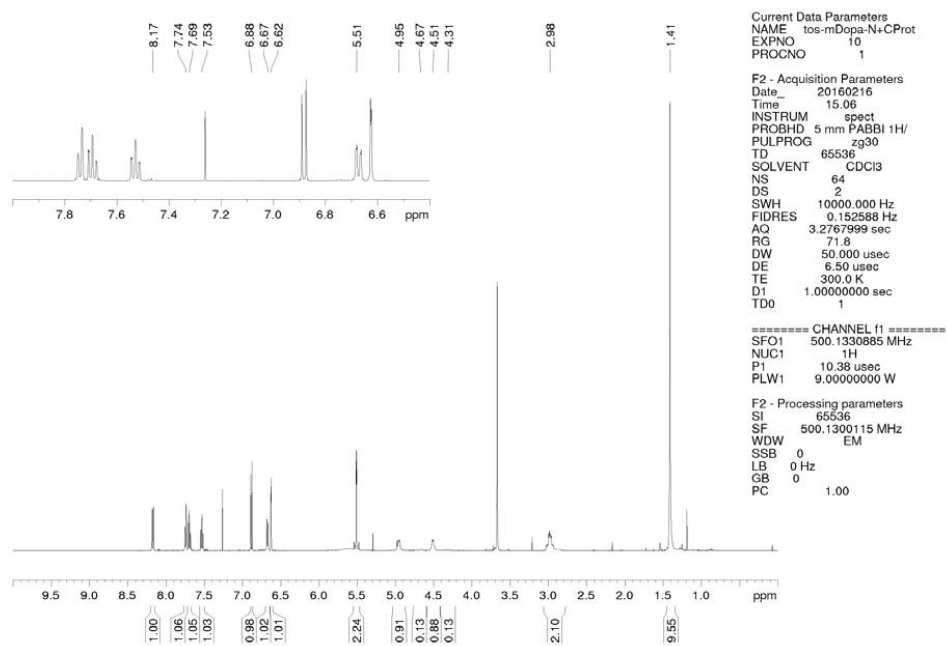
¹³C-NMR (125 MHz, CDCl₃) δ ppm: 172.4, 155.2, 147.3, 145.3, 145.1, 134.2, 133.0, 129.0, 128.8, 128.2, 125.3, 123.5, 115.4, 113.8, 80.1, 68.3, 54.6, 52.3, 38.0, 28.4

MS(ESI/HR): *m/z* = 391.1125 [MH⁺-C₈H₈] (9%) calc. 391.1141; *m/z* = 347.1126 [MH⁺-Boc] (100%) calc. 347.1243

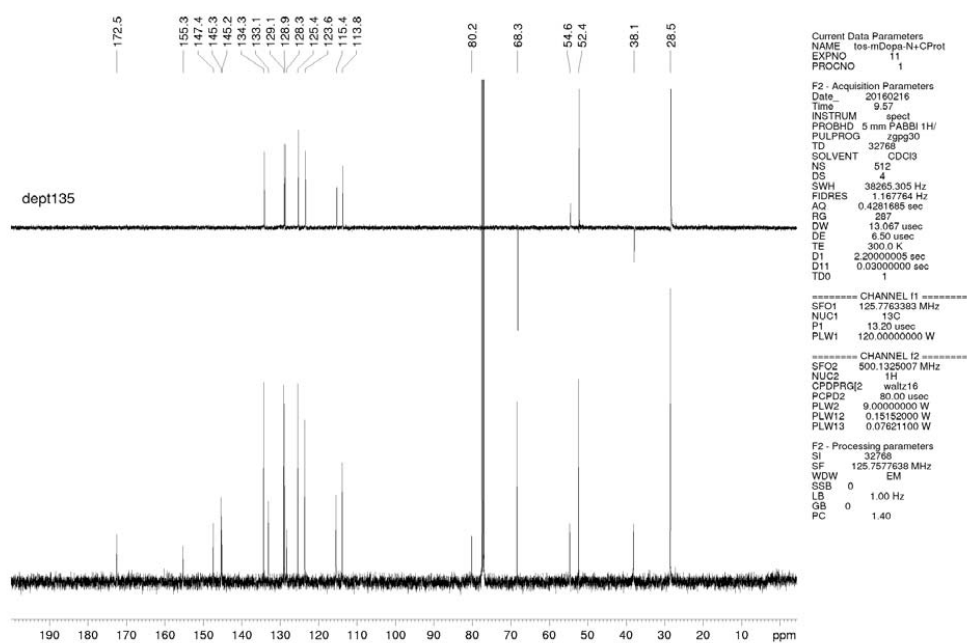
SUPPORTING INFORMATION

WILEY-VCH

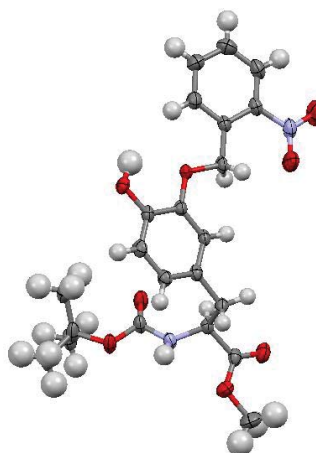
¹H-NMR (CDCl₃)



S5

13C-NMR+DEPT135 (CDCl₃)

S6



ellipsoids drawn at 50 % probability

Crystal color	white	
Empirical formula	C ₂₂ H ₂₆ N ₂ O ₈	
Formula weight	446.45	
Temperature	150.00(10) K	
Wavelength	1.54184 Å	
Crystal system	Monoclinic	
Space group	P2 ₁	
Unit cell dimensions	a = 14.5285(9) Å	a = 90°.
	b = 5.0154(3) Å	b = 100.440(6)°.
	c = 15.6583(10) Å	g = 90°.
Volume	1122.08(12) Å ³	
Z	2	
Density (calculated)	1.321 Mg/m ³	
Absorption coefficient	0.851 mm ⁻¹	
F(000)	472	
Crystal size	0.39 x 0.05 x 0.03 mm ³	
Theta range for data collection	2.87 to 67.50°.	
Index ranges	-17<=h<=13, -6<=k<=6, -18<=l<=16	
Reflections collected	6813	
Independent reflections	3900 [R(int) = 0.0540]	
Completeness to theta = 67.50°	99.9 %	
Absorption correction	Semi-empirical from equivalents	
Max. and min. transmission	0.9790 and 0.7348	
Refinement method	Full-matrix least-squares on F ²	
Data / restraints / parameters	3900 / 123 / 350	
Goodness-of-fit on F ²	0.989	
Final R indices [I>2sigma(I)]	R1 = 0.0519, wR2 = 0.1175	
R indices (all data)	R1 = 0.0705, wR2 = 0.1331	
Absolute structure parameter	0.1(3)	
Largest diff. peak and hole	0.164 and -0.225 e.Å ⁻³	

(S)-4-((2'-nitrobenzyl)oxy)-3-hydroxy-N-Boc-phenylalanine-methylester

¹H-NMR (500 MHz, CDCl₃) δ ppm: 8.16 (dd, *J* = 8.2, 1.2 Hz, 1 H), 7.73 (dd, *J* = 7.6, 1.0 Hz, 1 H), 7.68 (ddd, *J* = 7.6, 7.1, 1.2 Hz, 1 H), 7.52 (ddd, *J* = 8.2, 7.1, 1.0 Hz, 1 H), 6.75 (m, 2 H), 5.45 (dd, *J* = 8.2, 2.1 Hz, 1 H), 5.02-4.67 (m, 1 H), 4.59-4.31 (m, 1 H), 3.72 (s, 3 H), 3.06-2.77 (m, 2 H), 1.44-1.38 (m, 9 H)

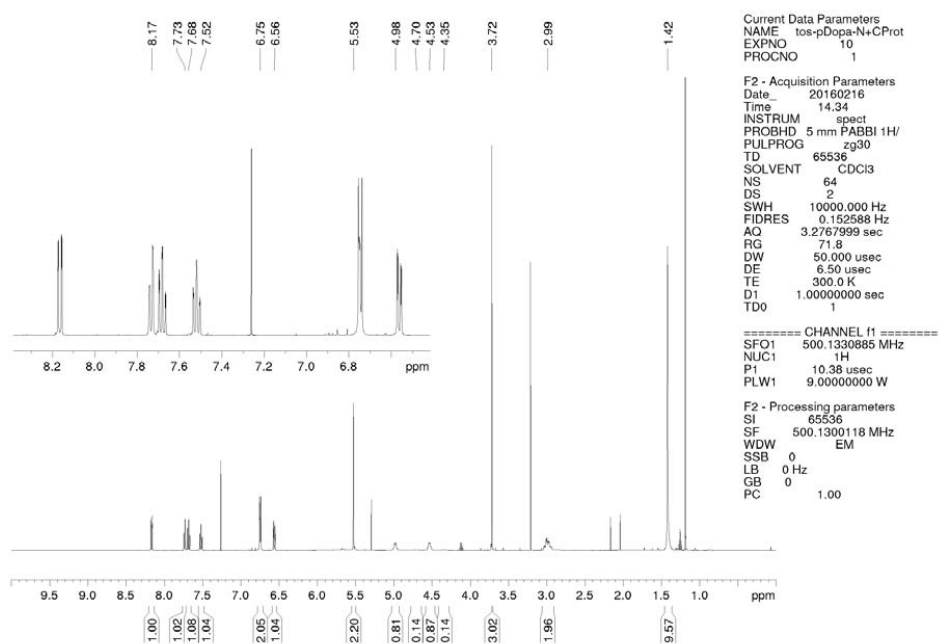
¹³C-NMR (125 MHz, CDCl₃) δ ppm: 172.4, 155.2, 147.3, 146.0, 144.4, 134.2, 133.2, 130.5, 128.9, 128.7, 125.3, 121.2, 116.4, 112.9, 80.1, 68.3, 54.6, 52.3, 37.8, 28.4

MS(ESI/HR): *m/z* = 391.1123 [MH⁺-C₆H₅] (5%) calc. 391.1141; *m/z* = 347.1124 [MH⁺-Boc] (100%) calc. 347.1243

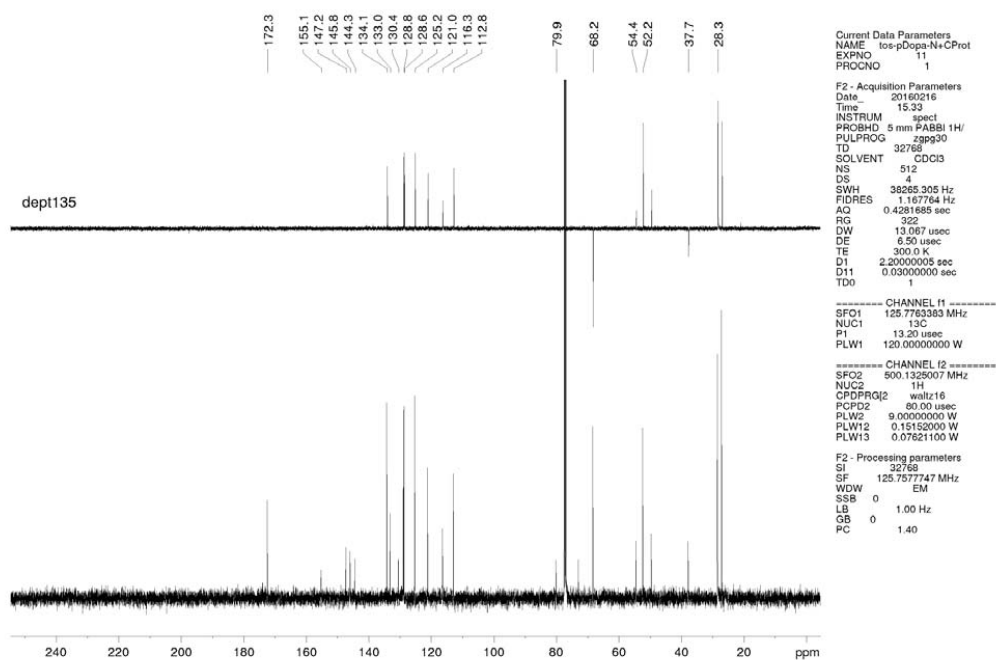
SUPPORTING INFORMATION

WILEY-VCH

¹H-NMR (CDCl₃)

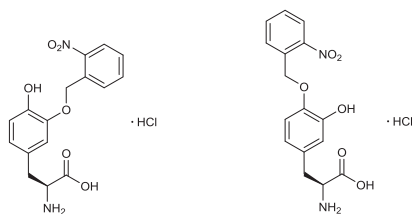


S9

13C-NMR+DEPT135 (CDCl₃)

S10

4) Synthesis of (S)-3-(2'-nitrobenzyl)- dihydroxyphenylalanine-hydrochloride and (S)-4-(2'-nitrobenzyl)- dihydroxyphenylalanine-hydrochloride



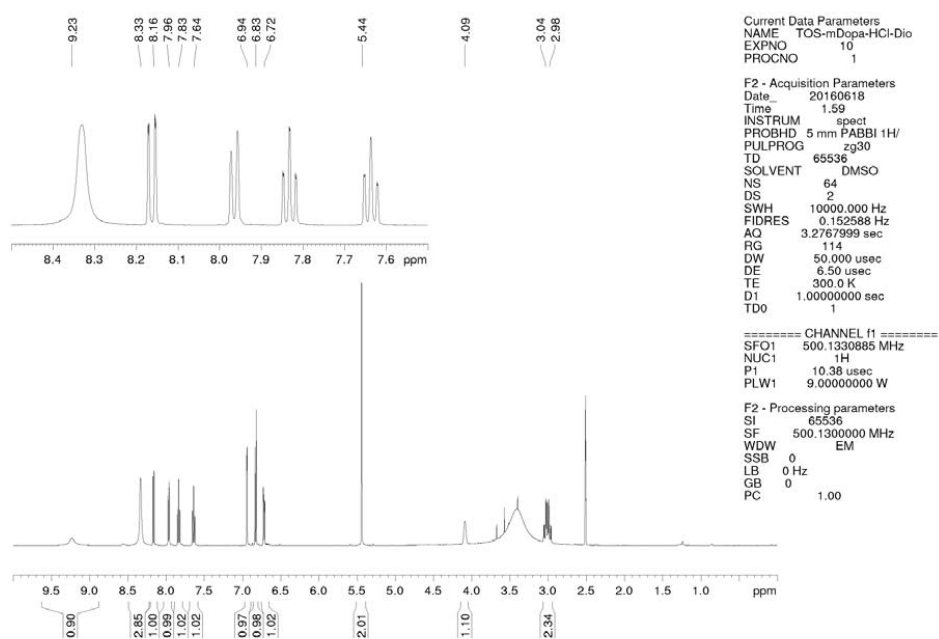
To 1.4 g of N-Boc-methylester-amino-acids (3.14 mmol) was added 20 ml of 32% aqueous HCl and 20 ml of 1,4-Dioxane. The mixture was heated to 50°C for 16 h and the solvent was removed under reduced pressure. The products were obtained as a white solids (1.1 g, 3.0 mmol).

(S)-3-(2'-nitrobenzyl)oxy-4-hydroxyphenylalanine

¹H-NMR (500 MHz, DMSO-d₆): 9.23(b, 1H), 8.33 (b, 3 H), 8.16 (dd, *J* = 8.2, 1.0 Hz, 1 H), 7.96 (d, *J* = 7.7 Hz, 1 H), 7.83 (dt, *J* = 7.7, 1.1 Hz, 1 H), 7.63 (td, *J* = 7.9, 1.3 Hz, 1 H), 6.94 (d, *J* = 1.9 Hz, 1 H), 6.83 (d, *J* = 8.1 Hz, 1 H), 6.72 (dd, *J* = 8.1, 1.9 Hz, 1 H), 5.44 (s, 2 H), 4.13-4.04 (m, 1 H), 3.03 (dd, *J* = 14.1, 6.1 Hz, 1 H), 2.98 (d, *J* = 14.1, 6.6 Hz, 1 H)

¹³C-NMR (125 MHz, DMSO-d₆) δ ppm: 170.4, 147.0, 146.4, 146.2, 134.2, 133.2, 129.1, 128.9, 125.4, 124.8, 123.0, 116.2, 116.1, 67.2, 53.3, 35.2

MS(ESI/HR/neg. Mode): 685.1761[2*M-2H+Na] (20%) calc. 685.1758; 663.1943[2*M-H] (100%) calc. 663.1938; 331.0933 [M-H] (20%) calc. 331.0931,

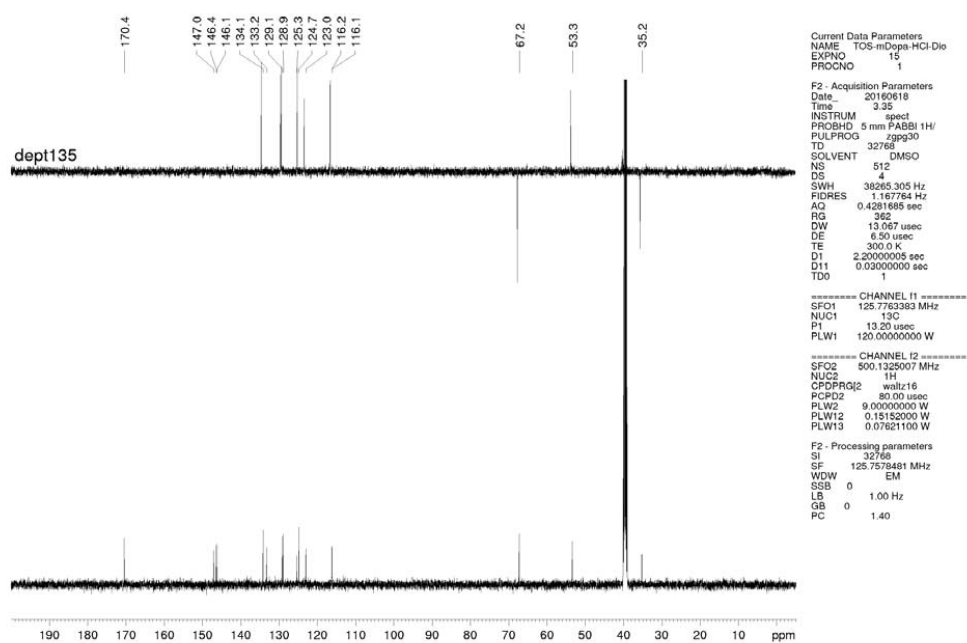
¹H-NMR (DMSO-d₆)

S12

SUPPORTING INFORMATION

WILEY-VCH

¹³C-NMR+DEPT135 (DMSO-d₆)



S13

(S)-4-((2'-nitrobenzyl)oxy)-3-hydroxyphenylalanine-hydrochloride

¹H-NMR (500 MHz, CD₃OD) δ ppm: 8.14 (dd, *J* = 8.1, 1.1 Hz, 1 H), 7.89 (dd, *J* = 7.8, 0.8 Hz, 1 H), 7.73 (td, *J* = 7.5, 1.2 Hz, 1 H), 7.56 (td, *J* = 7.6, 1.4 Hz, 1 H), 6.89 (d, *J* = 8.2 Hz, 1 H), 6.83 (d, *J* = 2.2 Hz, 1 H), 6.70 (dd, *J* = 8.2, 2.2 Hz, 1 H), 5.52 (s, 1 H), 4.18 (dd, *J* = 7.9, 5.2 Hz, 1 H), 3.21 (dd, *J* = 14.7, 5.2 Hz, 1 H), 3.03 (dd, *J* = 14.7, 7.9 Hz, 1 H)

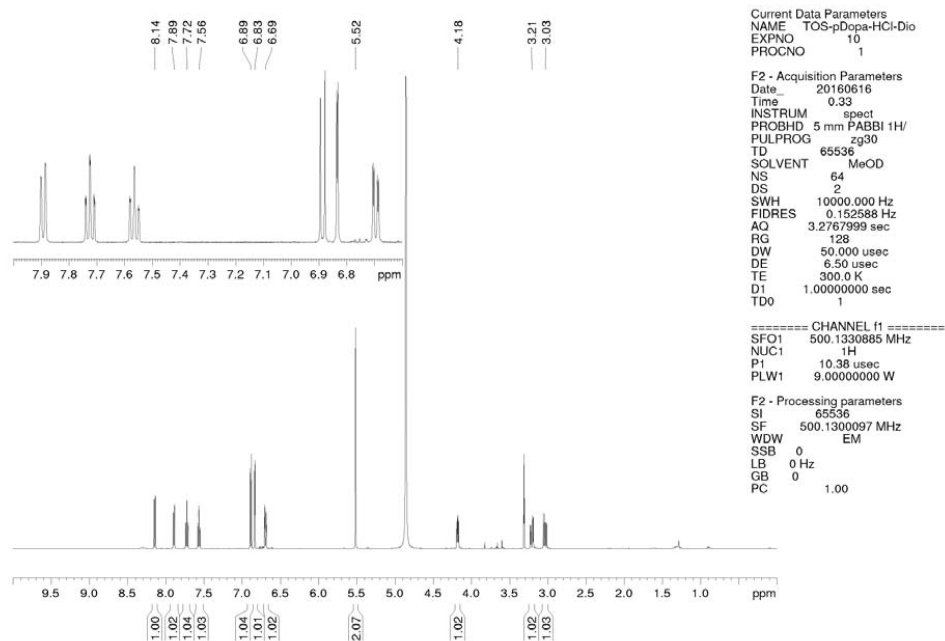
¹³C-NMR (125 MHz, CD₃OD) δ ppm: 171.2, 148.9, 148.7, 147.5, 134.9, 134.6, 130.2, 129.9, 129.3, 125.9, 121.8, 118.1, 115.6, 69.1, 55.2, 36.7

MS(ESI/HR/neg. Mode): 685.1760 [2*M-2H+Na] (10%) calc. 685.1761; 663.1943.1760[2*M-H] (100%) calc. 663.1938; 331.0933 [M-H] (60%) calc. 331.0931,

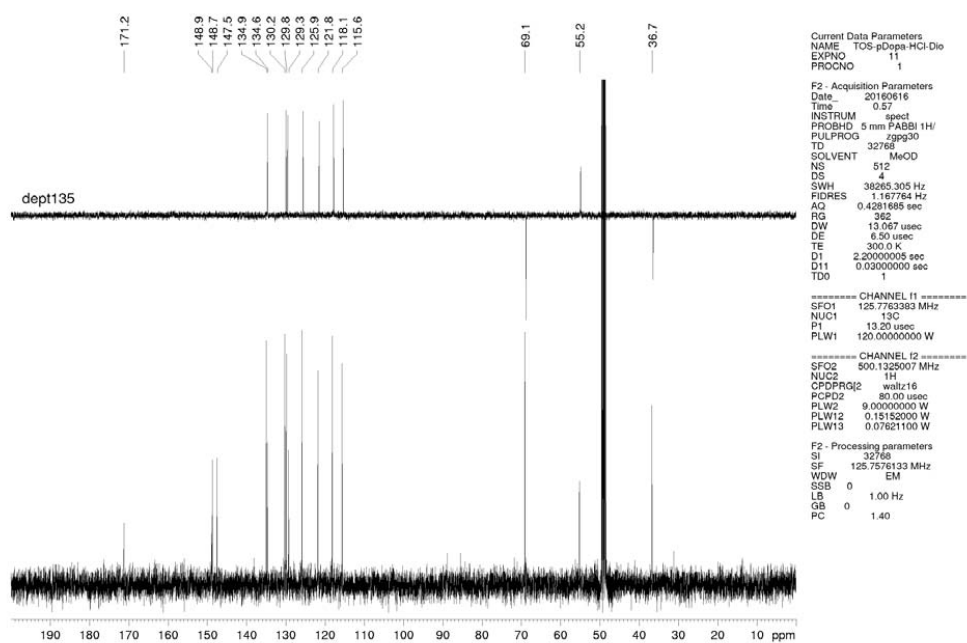
SUPPORTING INFORMATION

WILEY-VCH

¹H-NMR (MeOD)



S15

¹³C-NMR+DEPT135 (MeOD)

S16

SUPPORTING INFORMATION

WILEY-VCH

Computational design procedures. To build an initial model of *p*-ONB-Dopa, tyrosine coordinates taken from the substrate-tyrosine of the 1j1u crystal structure were loaded into Avogadro,^[2] and the extra atoms added. This model was then diversified around the χ 3-5 angles using OpenEye Omega,^[3] yielding 500 conformers. In addition, for every conformer, a version where χ 2 was rotated by 180° was created, to allow for the *m*-hydroxy group to be on either side of the *p*-ONB substituent, thus yielding a conformer ensemble of 1000 members. This ensemble, along with the protein coordinates of the 1j1u crystal structure, were then used as inputs for the Rosetta3 enzyme design protocol^[4]. The protocol's matching stage was set up such that the peptide backbone and dihydroxy-phenyl ring of ONB-Dopa were superimposed onto the WT tyrosine substrate, and that in addition, hydrogen-bonds between ONB-Dopa's nitro and *m*-hydroxy groups and uncharged protein residues (S/T/Y/N/Q/W) were formed. These matched interactions were then enforced with geometric constraints during the sequence design stage. Residues in the first and second shells around the side-chain binding pocket of 1j1u were redesigned, while those contacting the peptide backbone of ONB-Dopa were kept at their native identities. During this design stage, mutations at 26 positions in and around the active site, and correspondingly a sequence diversity of $20^{26} = 6.7 \cdot 10^{33}$, were considered. The resulting design models were then filtered for ligand binding score, match constraint score, and active site preorganization score. The best 49 designs were then used to define a library of size 10^8 .

Plasmid Construction. All plasmids were assembled by standard cloning methods and confirmed by DNA sequencing. For intact cell fluorescence experiments, SUMO-sfGFP based reporter constructs carrying an N-terminal His₆-tag and a C-terminal Strep-tag II were cloned in pET-28 (Novagen). Amber codons were introduced at position R2^[5] of sfGFP to yield SUMO-sfGFP(1TAG) and at positions R2, N39, K101, E132 and D190^[6,7] to yield SUMO-sfGFP(5TAG).

Plasmids harboring the orthogonal translation system consisting of the aaRS/tRNA_{CUA}-pair were constructed by cloning the aaRS genes into the pUltra vector^[8] or into the pBU16 plasmid. In the latter, the aaRS is placed under control of the *E. coli glnS*' promoter and terminator while an optimized mutant *Mj*tRNA_{CUA}^[9] is under control of the proK promoter/terminator. Additionally, it harbors a p15A origin of replication and an ampicillin resistance marker. The gene encoding WT *Mj*TyrRS was synthesized (GeneArt, Thermo Fisher Scientific) carrying the D286R mutation^[10] for improved amber suppression efficiency. aaRS encoding genes were cloned into pQE-80L (Qiagen) downstream of the His₆-tag to enable purification. The gene encoding *Mytilus galloprovincialis* fp-5, codon-optimized for expression in *E. coli*, was synthesized (GeneArt, Thermo Fisher Scientific) and cloned into plasmid pET-28a downstream of the MBP encoding gene. For sequence information see SI Note 1.

Library construction and selection. The library of the *Mj*TyrRS gene containing 17 mutagenic positions and a fixed D286R mutation^[10] was synthesized (GeneArt, Thermo Fisher Scientific). Library members were cloned into plasmid pBU18 under control of the *E. coli glnS*' promoter and terminator. Transformation of *E. coli* DH10b cells yielded $4 \cdot 10^9$ colonies, covering the theoretical library diversity of $1.6 \cdot 10^8$ by $> 99\%$.^[11] After plasmid DNA isolation, three alternate rounds of positive and negative selections were conducted as described earlier^[12]. Briefly, *E. coli* DH10b cells containing the plasmid pPAB26 carrying an optimized mutant *Mj*tRNA_{TyrCUA}^[9] under control of the proK promoter/terminator as well as the CAT gene harboring amber codons at positions Q98 and D181 were transformed with the library plasmid and plated on New Minimal Medium (NMM)^[13] agar plates supplemented with 1 mM of a mixture of *p*-/*m*-ONB-Dopa (~85:15) and 30, 50 or 70 $\mu\text{g ml}^{-1}$ chloramphenicol. Plates were incubated at 37°C for 48h followed by cell collection and purification of plasmid DNA. Next, cells containing the plasmid pBU26 with a barnase gene bearing amber codons at positions Q2 and D44 placed under control of an arabinose promoter and *rrnC* terminator as well as the optimized *Mj*tRNA_{TyrCUA}

were transformed and plated on LB agar plates containing ampicillin, kanamycin and 0.02 % (w/v) L-arabinose. Cells were collected after incubation at 37 °C for 16 h. Library plasmids were purified and used for the next selection round. After three rounds, clones specifically growing in presence of *p-/m*-ONB-Dopa were randomly selected and tested on NMM agar plates containing 20 or 100 µg ml⁻¹ chloramphenicol, in presence or absence of 1 mM of *p-/m*-ONB-Dopa. aaRS genes of 16 clones were sequenced, which survived on 100 µg ml⁻¹ chloramphenicol in the presence of the ncAA, but did not survive or only marginally grew at 20 µg ml⁻¹ chloramphenicol in the absence. Analysis revealed three different sequence groups (B9, A5, A72 named ONB-DopaRS-1, -2 and -3, respectively). aaRS genes were cloned into pUltra and pBU16.

Strain construction. C321.ΔA.exp^[14] was a gift from George Church (Addgene plasmid # 49018). The lambda DE3 lysogen was chromosomally introduced via the λDE3 Lysogenization Kit (Novagen).

Analysis of sfGFP expression by intact cell fluorescence measurements. SUMO-sfGFP variants and an Infinite M200 microtiter-plate reader (Tecan) were used. For constructs with one amber codon, *E. coli* BL21(DE) was employed, while C321.ΔA.exp(DE3)^[14] was used to examine production of constructs with five amber codons. Briefly, strains carrying an orthogonal translation system (placed on pBU16) and SUMO-sfGFP reporter plasmids were inoculated from glycerol stocks and grown to saturation overnight. Cultures were added to each well at 1:100 dilution in ZYP-5052 auto-induction medium^[15] to a final volume of 300 µl supplemented with antibiotics and the appropriate ncAA at a concentration of 1 mM. Cells were grown in 96 well µ-plates (Ibidi) covered with a gas-permeable foil (Sigma Aldrich) with orbital shaking for 17 h at 37°C. OD₆₀₀ and fluorescence were directly measured. Excitation and emission wavelengths of 481 nm and 511 nm, respectively, and a fixed manual gain were set. Fluorescence values were normalized to the corresponding OD₆₀₀. Biological triplicates were used for each measurement.

Protein Expression. The Selective Pressure Incorporation (SPI) method was used to incorporate Dopa into His₆-fp-5 employing the Tyr auxotrophic *E. coli* strain BL21(DE3)Δ*tyrA* Δ*pheA* (chromosomal gene deletions introduced via the method of Datsenko and Wanner^[16]). Briefly, cells transformed with the His₆-fp-5 encoding plasmid were grown overnight in LB medium at 37 °C. New minimal medium (NMM)^[13] supplemented with kanamycin and a limiting concentration of Tyr (30 µM) was inoculated in a 1:1000 ratio with the starter culture. Cells were grown overnight at 30 °C until depletion of Tyr at OD₆₀₀ ~ 0.8. Dopa was added to yield a final concentration of 1 mM, and target protein expression was induced by using 1 mM of IPTG. After shaking 4 h at 37 °C, cells were harvested by centrifugation. Purification via Ni-NTA affinity chromatography was performed as recently described^[17]. aaRSs and SUMO-sfGFP variants were produced in *E. coli* BL21(DE) or C321.ΔA.exp(DE3), respectively. ZYP-5052 media supplemented with appropriate antibiotics and, if necessary, the ncAA (1 mM final concentration) were inoculated with a starter culture and incubated for 16 h at 37 °C while shaking at 250 rpm. Cells were harvested by centrifugation. MBP-fp-5-His₆ proteins were produced in *E. coli* BL21(DE3) strain derivative B95.ΔA^[18] in presence of ONB-DopaRS-1 (gene placed on pUltra plasmid). Expressions were performed in EnPresso B media (BioSilta, Cambridgeshire, UK). Briefly, starter cultures of LB media supplemented with appropriate antibiotics were inoculated from glycerol stocks, and incubated for 8 h at 37 °C while shaking at 250 rpm. 250 ml of EnPresso B media supplemented with appropriate antibiotics were inoculated with 10 ml of the starter culture. After shaking at 30°C for 15 h, the ncAA was added (1.5 mM final concentration) and protein expression was induced using 1 mM of IPTG. After shaking at 37 °C for 24 h, cells were harvested by centrifugation.

Protein Purification. Cell pellets were resuspended (50 mM Tris-Cl or sodium phosphate, 150 mM - 300 mM NaCl, 20 mM imidazole, 10 % glycerol; pH 8.0) and lysed by high-pressure homogenization (M-110L Microfluidizer, Microfluidics). After centrifugation (18,000 g, 30 min), cleared lysates were loaded onto a Ni-NTA column and purified via an ÄKTA pure chromatography system. After washing, a linear gradient to 500 mM imidazole was applied to elute His-tagged proteins. For MBP-fp-5 variants, elution was performed with 50 mM sodium phosphate, 500 mM NaCl, 500 mM imidazole, 10% glycerol (pH 6.2). aaRSs were further purified via hydrophobic interaction chromatography (HIC). Relevant fractions were pooled and adjusted to 1.7 M $(\text{NH}_4)_2\text{SO}_4$ using a 25 mM HEPES, 3 M $(\text{NH}_4)_2\text{SO}_4$, 10 % glycerol (pH 7.5) solution. 8 ml were applied in each run onto a 1 ml HiTrap Phenyl HP column (GE Healthcare). After washing, a linear gradient to 0 M $(\text{NH}_4)_2\text{SO}_4$ was applied to elute the aaRS. Relevant fractions were pooled and dialyzed against storage buffer (25 mM HEPES, 150 mM NaCl, 10 % glycerol; pH 7.0). Concentrations of purified proteins were determined by measuring the OD_{280} or OD_{488} of purified sfGFP proteins.^[19] For fp-5, the following extinction coefficients were used (Figure S9): fp-5 (wt protein): $28,310 \text{ M}^{-1}\text{cm}^{-1}$; fp-5(5TAG)-ONB-Dopa: $54,515 \text{ M}^{-1}\text{cm}^{-1}$; fp-5(10TAG)-ONB-Dopa: $80,720 \text{ M}^{-1}\text{cm}^{-1}$.

TEV protease digestion. Purified MBP-fp-5 variants were dialyzed against a 50 mM Tris-HCl, 0.5 mM EDTA, 1 mM DTT (pH 8.0) solution and concentrated using an Amicon ultra 15 mL centrifugal filter (EMD Millipore). Digestion was performed overnight at room temperature with TEV protease added in a ratio of 1:50. Fp-5 variants were collected via centrifugation at 16,900g for 5 min, washed two times (50 mM Tris, pH 8.0) and resuspended in 5 % acetic acid or 70 % acetonitrile 0.1 % trifluoroacetic acid for mass spectrometry analyses.

Decaging of proteins. Purified proteins equipped with *m*-ONB-Dopa were decaged in a 10 mm quartz cuvette. A self-built 365 nm LED lamp (radiant flux ~ 1W) was used at a distance of ~ 3 mm for variable periods of time. Aliquots were analyzed by NBT dot blot analysis or LC/MS.

Western Blot analyses. SUMO-sfGFP or fp-5 protein variants were separated on 12 % or 15 % SDS polyacrylamide gels. After transfer onto nitrocellulose membranes, proteins carrying a His₆-tag were detected using rabbit anti hexahistidine antibody (Abcam) and goat anti-rabbit IgG alkaline phosphatase-conjugated antibody (Abcam). Proteins carrying a StrepII-tag were detected via mouse anti Strep tag II antibody (Merck Millipore) and goat anti-mouse IgG (whole molecule) alkaline phosphatase-conjugated antibody (Sigma Aldrich). Blots were developed using nitro-blue tetrazolium (NBT) and 5-bromo-4-chloro-3'-indolyphosphate (BCIP) staining.

NBT Dot Blot Analysis. A dot blot NBT staining assay was performed as described elsewhere^[17] with minor changes. Briefly, proteins were purified via Ni-NTA chromatography and digested with TEV protease. Proteins were prepared to a final concentration of 1 mg ml^{-1} in 5 % acetic acid. For decaging, proteins were irradiated for 45 min as described above. Next, 2 μl of each protein solution were spotted onto a nitrocellulose transfer membrane (0.2 μm pore size, Carl Roth). The membrane was immersed in 2 M sodium glycinate buffer (pH 10) containing 0.5 mg ml^{-1} NBT and incubated at room temperature until color development was observed. The membrane was washed with 0.2 M sodium borate solution (pH 8.5) and dH_2O .

Atomic Force Microscopy based Force Spectroscopy. Force-distance (FD) measurements were performed using a Bioscope Catalyst AFM (Bruker Nano, Santa Barbara, CA) with functionalized cantilevers (MLCT-D, Bruker Nano, Santa Barbara, CA) with

spring constants of $k = 0.04 - 0.06 \text{ N m}^{-1}$ (measured via thermal fluctuation method). After amino-functionalization with ethanolamine hydrochloride in dimethyl sulfoxide, AFM tips were functionalized with Acetal-PEG18-NHS linker molecules^[20] (Johannes Kepler University, Linz, Austria) and the respective mussel foot protein. For the functionalization with fp-5 variants, a protein solution with a concentration of 0.3 mg ml^{-1} in 10 mM sodium acetate buffer (pH 4.6) was used. Due to limited availability of the fp-5(10TAG) equipped with ten ONB-DOPA residues, the functionalization with this protein was performed at a concentration 0.1 mg ml^{-1} . Between functionalization and measurement, the cantilevers were stored under PBS at 4 °C for no longer than 96 h. For further details on the functionalization procedure, see references^[20–22]. All FD measurements were performed on freshly cleaved sheets of mica in 10 mM sodium acetate buffer (pH 4.6). The ramp size and ramp rate were set to 1 μm and 0.5 Hz, respectively. The force trigger was set to 200 pN with a surface delay of 1 s. With each AFM tip, 100 curves were recorded before and after excitation with UV light for 15 min. Fp-5(10TAG) was irradiated for up to 60 min. UV excitation was carried out with a Leica EL6000 light source (Leica Microsystems)

Mass Spectrometry. ESI-MS: Intact mass measurements of purified SUMO-sfGFP variants as well as MBP-fp5 variants were performed by electrospray LC-MS on an Agilent 6530 QTOF instrument coupled with an Agilent 1260 HPLC system (Agilent, Santa Clara, CA, USA) after external calibration. Samples were infused at a flow rate of 0.3 ml min^{-1} onto a gradient from 5 % acetonitrile 0.1 % formic acid in water to 80 % acetonitrile 0.1 % formic acid in water through a C5 column, 2.1·100 mm, 3 micron (Supelco analytical, Sigma-Aldrich) over 20 minutes. Spectra deconvolution was performed with Agilent MassHunter Qualitative Analysis software employing the maximum entropy deconvolution algorithm. **MALDI-MS:** After TEV digestion, purified fp-5(5TAG) and fp-5(10TAG) proteins were dissolved in 70 % acetonitrile 0.1 % trifluoroacetic acid of which 0.5 μl were mixed with 0.5 μl saturated 2,5-dihydroxybenzoic acid matrix solution (in 70 % acetonitrile 0.1 % trifluoroacetic acid). One μl sample of protein/matrix solution was spotted on the MALDI plate and then dried. The sample was analyzed with a Bruker ultrafleXtreme MALDI-TOF mass spectrometer (Bruker Daltonics). MS results were analyzed with Bruker Daltonics FlexAnalysis 4.0 software.

Protein Crystallization and Data Collection. ONB-DopaRS-1 was crystallized at room temperature (291 K). Crystals were obtained by the sitting-drop vapor diffusion method by mixing 1:1 protein (17 mg ml^{-1} previously incubated with 4-fold molar excess of a mixture of *p/m*-ONB-DOPA) with precipitant (200 mM CaCl_2 , 100 mM HEPES pH 7.5, 53 % PEG 400). For data collection at 100 K, crystals were harvested in precipitant solution and shock-frozen. Diffraction data were collected on BL14.1 operated by the Joint Berlin MX-Laboratory (BESSY II electron storage ring, Helmholtz-Zentrum Berlin, Germany).^[23] Diffraction data were indexed, integrated and scaled with XDS^[24] and XDSAPP.^[25] Crystals belong to space group $P2(1)2(1)2(1)$ (sg number 19) with cell constants of $a = 55.51 \text{ \AA}$, $b = 78.27 \text{ \AA}$ and $c = 137.88 \text{ \AA}$ corresponding to a solvent content of 50 % with two protein molecules per asymmetric unit. Statistics for data collection are in Table S3.

Structure Determination and Refinement. The crystal structure was determined by Patterson search techniques with Phaser^[26] as implemented in the CCP4 suite^[27] using two monomers from apo *Methanocaldococcus jannaschii* tyrosyl-tRNA synthase (PDB code 1U7D) as homologous search model. The replacement solution was validated with COOT^[28] and after rigid-body refinement using Refmac5^[29] the protein model was edited to match the ten introduced mutations in DopaRS-1 sequence: Y32A, L65I, H70A, Q109A, D158A, I159A, L162M, A167N, A180Q and D286R. Iterative rounds of model building and refinement were conducted respectively with COOT^[28] and Refmac5^[29]. Chain B showed clear electron density for a tyrosine derivative allowing us to model *m*-ONB-Dopa in the active site (Figure S5 stereo view).

SUPPORTING INFORMATION

WILEY-VCH

Chain A also displayed additional electron density but less defined. The last cycles of refinement were calculated with Phenix^[30] and the refined structure model validated with Molprobit^[31]. A final *R*-factor of 17.83% (R_{free} -Factor = 21.76%) at a resolution of 1.9 Å was obtained. The *B*-Factors for *m*-ONB-Dopa are in the same value range as surrounding residues. The refined model of ONB-DopaRS-1 with bound *m*-ONB-Dopa contains two monomers (chain A: Asp2-Ala138 and Asn143-Leu306; chain B: Met1-Leu306), one *m*-ONB-Dopa molecule (bound in chain B), one calcium and one chloride ion, and 341 solvent molecules. Each of the two protein molecules in the asymmetric unit builds, together with a crystallographic two-fold symmetry-related molecule builds a physiologic homodimer.^[32] The protein model displays one single outlier residue in chain B: Cys231, which is well defined in the electron density map. Refinement statistics and stereochemistry analysis calculated with Molprobit as implemented in Phenix^[30] are presented in Table S3. The simulated-annealing Polder omit map was calculated as implemented in Phenix.^[30] Structure comparisons were calculated using Dali.^[33] Figure S5a and S5b were prepared with Pymol.^[34] Atomic coordinates and structure factors have been deposited with the Protein Data Bank (www.pdbe.org) with accession code 5L7P.

SI Figures

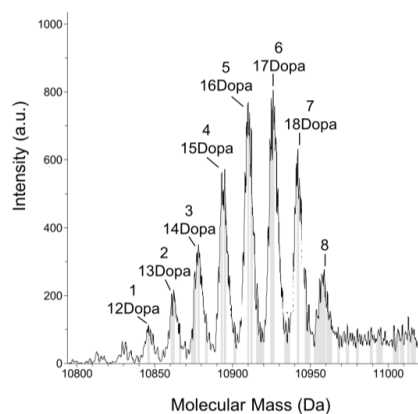


Figure S1. Deconvoluted ESI-MS spectrum of fp-5 after Dopa incorporation through SPI. Fp-5 was produced in Tyr auxotrophic *E. coli* strain BL21(DE3) Δ *tyrA* Δ *pheA* in NMM medium, and in the presence of 1 mM Dopa. Despite careful control of growth conditions, a highly heterogeneous product was obtained. Peaks correspond to fp-5 variants equipped with Dopa at 12-18 out of 19 Tyr sites (Peaks 1-7), while remaining positions still contain Tyr. Peak 8 could not be assigned to a distinct mass, but could represent fp-5 bearing 19 Dopa residues. The found and expected masses are as follows: fp-5(12Dopa), (1) observed: 10846.1 Da, expected: 10847.7 Da. fp-5(13Dopa), (2) observed: 10862.5 Da, expected: 10863.7 Da. fp-5(14Dopa), (3) observed: 10878.4 Da, expected: 10879.7 Da. fp-5(15Dopa), (4) observed: 10895.1 Da, expected: 10895.7 Da. fp-5(16Dopa), (5) observed: 10910.2 Da, expected: 10911.7 Da. fp-5(17Dopa), (6) observed: 10926.4 Da, expected: 10927.7 Da. fp-5(18Dopa), (7) observed: 10942.1 Da, expected: 10943.7 Da. fp-5(19Dopa), (8) observed: -, expected: 10959.7 Da.

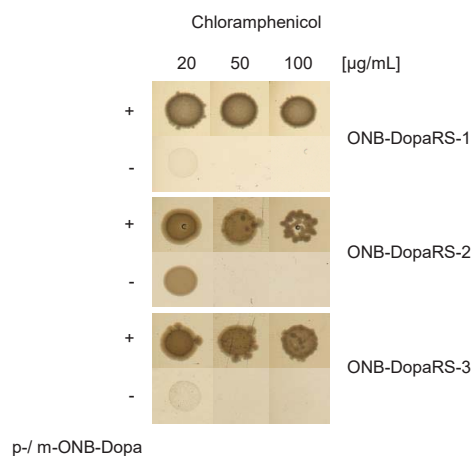


Figure S2. Growth assay of *E. coli* DH10b expressing CAT(2TAG) and o-pairs. ONB-DopaRS-1-3 and $MtRNA_{CUA}^{Tyr}$ were tested at different Cm concentrations in the presence (+) and absence (-) of 1 mM *p-/m*-ONB-Dopa, respectively. Cells expressing ONB-DopaRS-1, -2 and -3 and chloramphenicol acetyltransferase bearing two amber stop codons (CAT(2TAG)) displayed similar growth in the presence and absence of ONB-Dopa, with ONB-DopaRS-1 showing weakest growth in the absence of *p-/m*-ONB-Dopa. Bacteria were grown in LB medium, diluted to an OD_{600} of 1.0, followed by spotting of 2 μ l onto NMM agar supplemented with Amp, Kan and different concentrations of Cm and 1 mM of the ncAA.

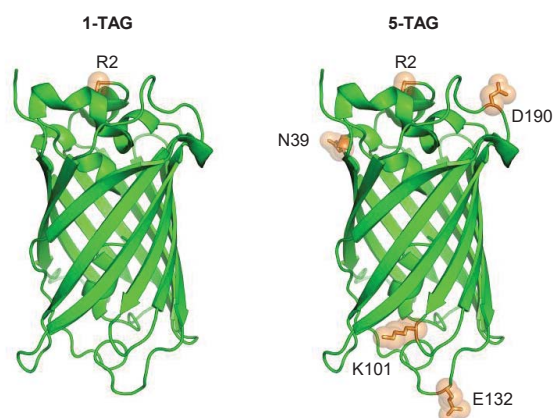


Figure S3. sfGFP variants carrying one or five amber sites. sfGFP structure (PDB code: 2B3P) illustrating the solvent-exposed sites where the amber (TAG) codons, and thus ncAAs, were introduced. In comparison to 2B3P, the sfGFP wildtype used in the present study bears a K2R mutation. The N-terminally fused His₆-SUMO protein and the C-terminal Strep tag II are not illustrated.

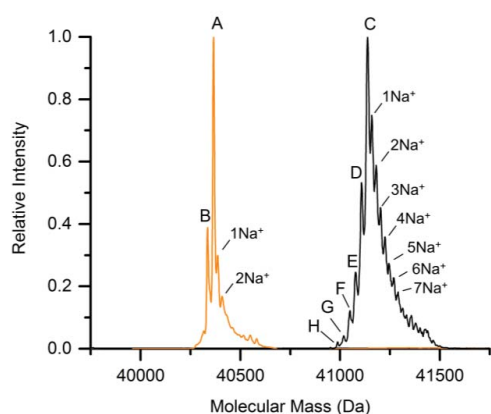


Figure S4. Deconvoluted ESI-MS spectra of SUMO-sfGFP(1TAG) and SUMO-sfGFP(5TAG) after incorporation of *m*-ONB-Dopa using ONB-DopaRS-1. The found and expected masses are as follows: SUMO-sfGFP(1ONB-Dopa), (A) observed: 40366.7 Da, expected: 40366.6 Da. Peak (B) is consistent with reduction of the nitro group to an amine^[35]: obs.: 40337.8 Da; exp.: 40336.6 Da. SUMO-sfGFP(5 ONB-Dopa), (C) observed: 41138.4 Da, expected: 41137.3 Da. Peak (D) and adjacent peaks (E, F, G, H) at lower masses are consistent with reduction of the nitro group to an amine. SUMO-sfGFP(4 ONB-Dopa, 1 O-Aminobenzyl-Dopa), (D) observed: 41109.2 Da, expected: 41107.3 Da. SUMO-sfGFP(3 ONB-Dopa, 2 O-Aminobenzyl-Dopa), (E) observed: 41079.6 Da, expected: 41077.3 Da. SUMO-sfGFP(2 ONB-Dopa, 3 O-Aminobenzyl-Dopa), (F) observed: 41050.8 Da, expected: 41047.3 Da. SUMO-sfGFP(1 ONB-Dopa, 4 O-Aminobenzyl-Dopa), (G) observed: 41019.2 Da, expected: 41017.3 Da. SUMO-sfGFP(5 O-Aminobenzyl-Dopa), (H) observed: 40988.2 Da, expected: 40987.3 Da. As different protein species could not be separated via HPLC, corresponding MS signal intensities were used to provide an estimation about relative quantities of protein species assuming similar ionization properties. For SUMO-sfGFP(1TAG) the ratio is as follows: 62 % (1 ONB-Dopa), 38 % (1 O-Aminobenzyl-Dopa). For SUMO-sfGFP(5TAG) the ratio is as follows: 51 % (5 ONB-Dopa), 27 % (4 ONB-Dopa/1 O-Aminobenzyl-Dopa), 13 % (3 ONB-Dopa/2 O-Aminobenzyl-Dopa), 6 % (2 ONB-Dopa/3 O-Aminobenzyl-Dopa), 2 % (1 ONB-Dopa/4 O-Aminobenzyl-Dopa), 1 % (5 O-Aminobenzyl-Dopa).

SUPPORTING INFORMATION

WILEY-VCH

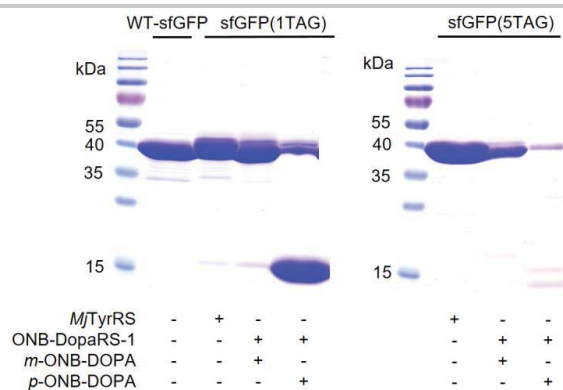


Figure S5. Coomassie-stained 15% SDS-PAGE of sfGFP(1TAG) and sfGFP(5TAG) constructs purified via Ni-NTA chromatography.

Left: sfGFP and sfGFP(1TAG) constructs expressed in BL21(DE3) with different o-pairs. Right: sfGFP(5TAG) constructs expressed in C321.ΔA.exp(DE3) with different o-pairs. Equal volumes of pooled Ni-NTA elutions were used for SDS-PAGE. The expected molecular weight of full-length sfGFP construct is ~ 40 kDa (varies slightly with different ncAAs), while translation termination at position 2 of sfGFP results in a mass of ~ 12.5 kDa.

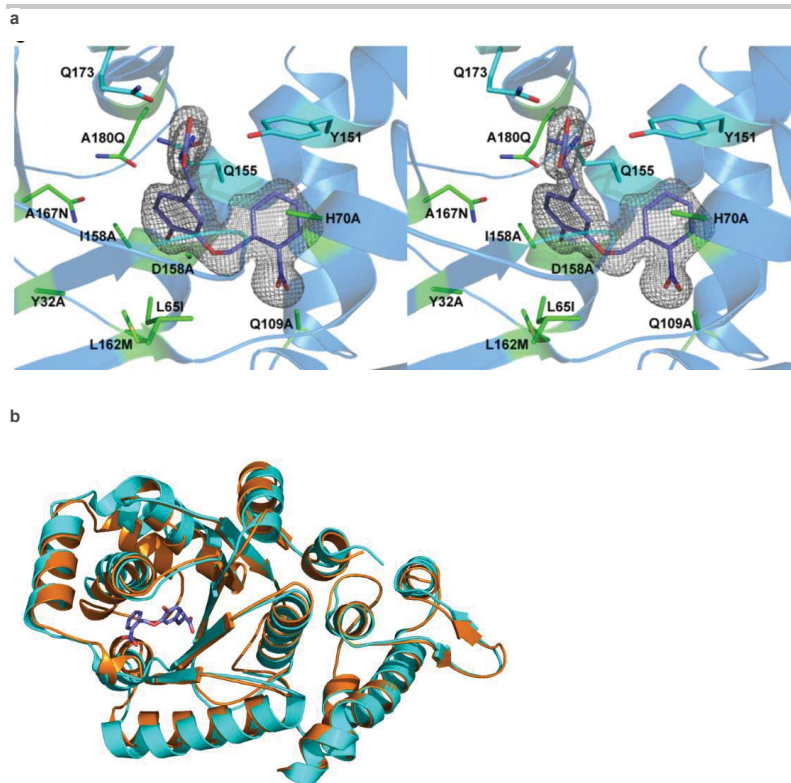


Figure S6. Stereo view of *m*-ONB-Dopa bound in the active site of ONB-DopaRS-1 (chain B) and comparison of the overall structure with *Mj*TyrRS. (a) The substrate was omitted for the calculation of the simulated-annealing Polder omit map (grey mesh countered at 3.6 sigma). The electron density is less defined for the nitro group of the ONB moiety, which might be explained by the absence of stabilizing interactions between ONB and the polypeptide. Side chains are shown as sticks with blue for nitrogen and red for oxygen. Residues with carbon in cyan, Q155, Q173 and Y151 are at hydrogen-bonding distance to the carboxyl- and amido groups of *m*-ONB-Dopa. Mutations are shown with carbon in green. (b) Comparison of the overall structures of ONB-DopaRS-1 in complex with *m*-ONB-Dopa (orange) and wild type *Mj*TyrRS (cyan; PDB code 1U7D). ONB-Dopa is shown in sticks with magenta for carbon, red for oxygen and blue for nitrogen. The structure of ONB-DopaRS-1 in complex with *m*-ONB-Dopa superimposes well on that of wild type *Mj*TyrRS with tyrosine bound with a r.m.s. deviation of 1.8 Å for the main chain atoms, as expected for the sequence similarity of 97%

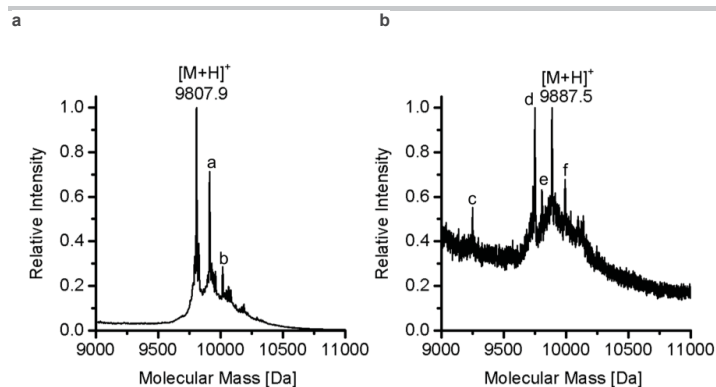


Figure S7. MALDI-TOF spectra of MBP-fp-5 variants. (a) MBP-fp-5(5TAG) and (b) MBP-fp-5(10TAG) after incorporation of *m*-ONB-Dopa, TEV digest and irradiation with UV light. The found and expected masses are as follows: fp-5(5 Dopa), observed: 9807.9 Da (M+H⁺), expected: 9807.7 Da (M+H⁺); fp-5(10 Dopa), observed: 9887.5 Da (M+H⁺), expected: 9887.7 Da (M+H⁺). Other observed masses are as follows: (a) observed: 9912.7 Da (M+H⁺); (b) observed: 10018.0 Da (M+H⁺); (c): 9250.3 Da (M+H⁺); (d): 9751.1 Da (M+H⁺); (e): 9808.4 Da (M+H⁺); (f): 9993.5 Da (M+H⁺). No signals were observed corresponding to protein species containing reduced ONB-Dopa residues.

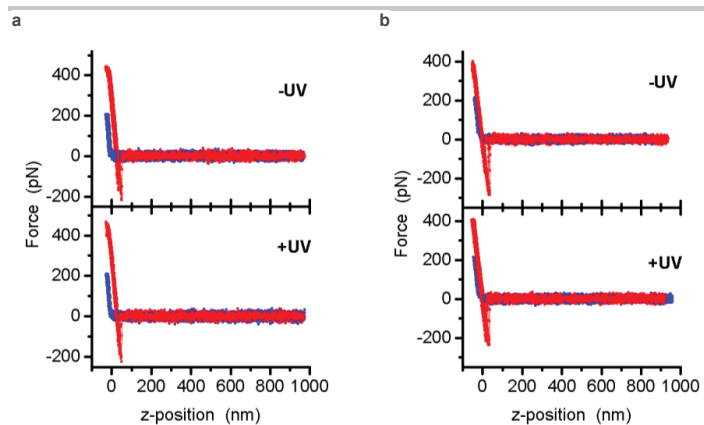


Figure S8. Typical FD curves of bare and amino-functionalized cantilever tips. Interaction of bare cantilever tips (a), and amino-functionalized tips (b) with a mica surface before and after irradiation with UV light. Blue and red curves depict approach and retraction signals, respectively.

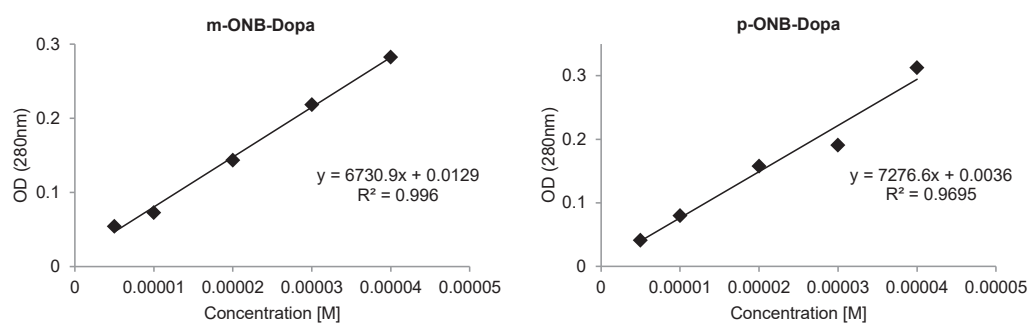


Figure S9. Calculations of nAA extinction coefficients. Extinction coefficients were determined by regression analysis of a 2x dilution series of each nAA in H₂O as a function of the OD₂₈₀ of the solution.

SI Tables

Table S1. Library resulting from Rosetta calculations and sequences of selected *Mj*TyrRS mutants.

<i>Mj</i> TyrRS Position	Library	ONB-DopaRS		
		-1	-2	-3
Y32	A, S	A	S	S
L65	A, I, L, F, S	I	I	I
A67	A, Q	A	A	A
L69	L, K, G, W	L	L	L
H70	A, N, S	A	A	A
G105	G, A, Q	G	G	G
F108	F, L	F	F	F
Q109	A, Q, Y	A	A	A
M154	E, M, T, G	M	M	M
D158	A, G, S	A	A	A
I159	A, G, S, I	A	G	G
L162	A, M	M	M	M
V164	A, T, V	V	A	V
A167	N, Q, G, S	N	N	S
H177	A, H, Q, Y	H	H	H
A180	A, Q	Q	Q	Q
V188	N, Q, T, V	V	V	Q

Table S2. Protein yields of the SUMO-sfGFP-TAG constructs expressed in *E. coli* BL21(DE3) and C321.ΔA.exp(DE3).

Protein	Strain	O-pair	Amino acid	Protein yield (mg l ⁻¹)
SUMO-sfGFP-WT	BL21(DE3)	-	-	89 ± 16
		<i>Mj</i> TyrRS	-	81 ± 23
SUMO-sfGFP(1TAG)	BL21(DE3)	ONB-DopaRS-1	<i>m</i> -ONB-Dopa	61 ± 9
		ONB-DopaRS-1	<i>p</i> -ONB-Dopa	6 ± 1
SUMO-sfGFP(5TAG)	C321.ΔA.exp(DE3)	<i>Mj</i> TyrRS		89 ± 12
		ONB-DopaRS-1	<i>m</i> -ONB-Dopa	23 ± 1
		ONB-DopaRS-1	<i>p</i> -ONB-Dopa	2 ± 0.2

Protein yields were determined from samples purified via Ni-NTA affinity chromatography by measuring the OD₄₈₈. n.d.: not determined since yields were too low. Data represent mean ± s.d. of biological triplicates.

SUPPORTING INFORMATION

WILEY-VCH

Table S3. Data collection and refinement statistics of ONB-DopaRS-1 bound with *m*-ONB-Dopa (molecular replacement).

	ONB-DopaRS-1
Data collection	
Space group	$P2_12_12_1$
Cell dimensions	
a, b, c (Å)	55.51, 78.27, 137.88
α, β, γ (°)	90.00
Resolution (Å)	43.23-1.90 (2.01-1.90)*
R_{sym} or R_{merge}	6.2 (80.3)
$I / \sigma I$	25.43 (2.90)
Completeness (%)	99.7 (98.6)
Redundancy	10.2 (9.8)
Refinement	
Resolution (Å)	43.23-1.90 (1.95-1.90)
No. reflections	48182
$R_{\text{work}} / R_{\text{free}}$ -Factors	0.178 / 0.218
No. atoms (total/non-H)	10351 / 5265
Protein	9931
Ligand/PEG/ion	39/38/2
Water	341
B -factors (Å ²)	
Protein	32
Ligand/PEG/ion	38/56/42.5
Water	46.7
R.m.s. deviations	
Bond lengths (Å)	0.012
Bond angles (°)	1.189

*values correspond to one crystal.

References

- [1] N. Guimond, P. Mayer, D. Trauner, *Chem. - A Eur. J.* **2014**, *20*, 9519–9523.
- [2] M. D. Hanwell, D. E. Curtis, D. C. Lonie, T. Vandermeersch, E. Zurek, G. R. Hutchison, *J. Cheminform.* **2012**, *4*, 17.
- [3] P. C. D. Hawkins, A. G. Skillman, G. L. Warren, B. A. Ellingson, M. T. Stahl, *J. Chem. Inf. Model.* **2010**, *50*, 572–84.
- [4] F. Richter, A. Leaver-Fay, S. D. Khare, S. Bjelic, D. Baker, *PLoS One* **2011**, *6*, e19230.
- [5] C. Fan, J. M. L. Ho, N. Chirathivat, D. Söll, Y.-S. Wang, *ChemBiochem* **2014**, *15*, 1805–9.
- [6] D. B. F. Johnson, J. Xu, Z. Shen, J. K. Takimoto, M. D. Schultz, R. J. Schmitz, Z. Xiang, J. R. Ecker, S. P. Briggs, L. Wang, *Nat. Chem. Biol.* **2011**, *7*, 779–86.
- [7] S. H. Hong, I. Ntai, A. D. Haimovich, N. L. Kelleher, F. J. Isaacs, M. C. Jewett, *ACS Synth. Biol.* **2014**, *3*, 398–409.
- [8] A. Chatterjee, S. B. Sun, J. L. Furman, H. Xiao, P. G. Schultz, *Biochemistry* **2013**, *52*, 1828–1837.
- [9] T. S. Young, I. Ahmad, J. A. Yin, P. G. Schultz, *J. Mol. Biol.* **2010**, *395*, 361–74.
- [10] T. Kobayashi, O. Nureki, R. Ishitani, A. Yaremchuk, M. Tukulko, S. Cusack, K. Sakamoto, S. Yokoyama, *Nat. Struct. Biol.* **2003**, *10*, 425–432.
- [11] S. Kille, C. G. Acevedo-Rocha, L. P. Parra, Z.-G. Zhang, D. J. Opperman, M. T. Reetz, J. P. Acevedo, *ACS Synth. Biol.* **2013**, *2*, 83–92.
- [12] C. C. Liu, P. G. Schultz, *Annu. Rev. Biochem.* **2010**, *79*, 413.
- [13] N. Budisa, B. Steipe, P. Demange, C. Eckerskorn, J. Kellermann, R. Huber, *Eur. J. Biochem.* **1995**, *230*, 788–96.
- [14] M. J. Lajoie, A. J. Rovner, D. B. Goodman, H.-R. Aerni, A. D. Haimovich, G. Kuznetsov, J. A. Mercer, H. H. Wang, P. A. Carr, J. A. Mosberg, et al., *Science* **2013**, *342*, 357–60.
- [15] F. W. Studier, *Protein Expr. Purif.* **2005**, *41*, 207–34.
- [16] K. A. Datsenko, B. L. Wanner, *Proc. Natl. Acad. Sci. U. S. A.* **2000**, *97*, 6640–5.
- [17] B. Yang, N. Ayyadurai, H. Yun, Y. S. Choi, B. H. Hwang, J. Huang, Q. Lu, H. Zeng, H. J. Cha, *Angew. Chem. Int. Ed. Engl.* **2014**, *53*, 13360–4.
- [18] T. Mukai, H. Hoshi, K. Ohtake, M. Takahashi, A. Yamaguchi, A. Hayashi, S. Yokoyama, K. Sakamoto, *Sci. Rep.* **2015**, *5*, 9699.
- [19] J.-D. Pédelacq, S. Cabantous, T. Tran, T. C. Terwilliger, G. S. Waldo, *Nat. Biotechnol.* **2006**, *24*, 79–88.
- [20] "Institute of Biophysics, Johannes Kepler University Linz." can be found under <http://www.jku.at/biophysics/content/e257042>, n.d.
- [21] A. Ebner, L. Wildling, A. S. M. Kamruzzahan, C. Rankl, J. Wruss, C. D. Hahn, M. Hölzl, R. Zhu, F. Kienberger, D. Blaas, et al., *Bioconjug. Chem.* **2007**, *18*, 1176–84.
- [22] L. Wildling, B. Unterauer, R. Zhu, A. Rupprecht, T. Haselgrübler, C. Rankl, A. Ebner, D. Vater, P. Pollheimer, E. E. Pohl, et al., *Bioconjug. Chem.* **2011**, *22*, 1239–48.
- [23] U. Mueller, N. Darowski, M. R. Fuchs, R. Förster, M. Hellmig, K. S. Paithankar, S. Pühringer, M. Steffien, G. Zocher, M. S. Weiss, *J. Synchrotron Radiat.* **2012**, *19*, 442–449.
- [24] W. Kabsch, *Acta Crystallogr. D. Biol. Crystallogr.* **2010**, *66*, 125–32.
- [25] M. Krug, M. S. Weiss, U. Heinemann, U. Mueller, *J. Appl. Crystallogr.* **2012**, *45*, 568–572.
- [26] A. J. McCoy, R. W. Grosse-Kunstleve, P. D. Adams, M. D. Winn, L. C. Storoni, R. J. Read, *J. Appl. Crystallogr.* **2007**, *40*, 658–674.
- [27] N. 4 Collaborative Computational Project, *Acta Crystallogr. D. Biol. Crystallogr.* **1994**, *50*, 760–3.
- [28] P. Emsley, K. Cowtan, *Acta Crystallogr. D. Biol. Crystallogr.* **2004**, *60*, 2126–32.
- [29] G. N. Murshudov, P. Skubák, A. A. Lebedev, N. S. Pannu, R. A. Steiner, R. A. Nicholls, M. D. Winn, F. Long, A. A. Vagin, *Acta Crystallogr. Sect. D Biol. Crystallogr.* **2011**, *67*, 355–367.
- [30] P. V. Afonine, R. W. Grosse-Kunstleve, N. Echols, J. J. Headd, N. W. Moriarty, M. Mustyakimov, T. C. Terwilliger, A. Urzhumtsev, P. H. Zwart, P. D. Adams, *Acta Crystallogr. D. Biol. Crystallogr.* **2012**, *68*, 352–67.
- [31] V. B. Chen, W. B. Arendall, J. J. Headd, D. A. Keedy, R. M. Immormino, G. J. Kapral, L. W. Murray, J. S. Richardson, D. C. Richardson, *Acta Crystallogr. D. Biol. Crystallogr.* **2010**, *66*, 12–21.
- [32] B. A. Steer, P. Schimmel, *J. Biol. Chem.* **1999**, *274*, 35601–6.
- [33] L. Holm, P. Rosenström, *Nucleic Acids Res.* **2010**, *38*, W545–9.
- [34] "The PyMOL Molecular Graphics System, Version 1.2r3pre, Schrödinger, LLC.," can be found under <http://www.pymol.org>, n.d.
- [35] D. P. Nguyen, M. Mahesh, S. J. Elsässer, S. M. Hancock, C. Uttamapinant, J. W. Chin, *J. Am. Chem. Soc.* **2014**, *136*, 2240–3.

Author Contributions

M.H. designed the experimental aRS library, designed and selected aRS variants, performed experiments and wrote the manuscript. F.R. performed the computational design process, designed the experimental aRS library, designed experiments, and wrote the manuscript. T.S. performed chemical synthesis of ONB-Dopa isomers and wrote the manuscript. T.F. performed atomic force microscopy based force spectroscopy and wrote the manuscript. B.M.M. performed protein crystallization and structure determination, and wrote the manuscript. T.B. designed experiments and wrote the manuscript. P.D. performed chemical synthesis and assisted in writing the manuscript. H.D. directed structure determination and assisted in writing the manuscript. K.J.

SUPPORTING INFORMATION

WILEY-VCH

directed atomic force microscopy studies and assisted in writing the manuscript. A.M. directed experimental work and assisted in writing the manuscript.

N.B. directed experimental work and wrote the manuscript.

Danksagung

An dieser Stelle möchte ich mich bei allen bedanken, die mich auf meinem Weg bis zur Fertigstellung dieser Arbeit unterstützt haben. Allen voran natürlich bei Prof. Dr. Karin Jacobs. Klar, als Chefin der Gruppe muss sie ganz vorne stehen, aber für mich ist der eigentliche Grund dafür die einfach ausgezeichnete Betreuung – bestimmt, aber doch mit allen Freiheiten, eigene Ideen zu verwirklichen und auch Dinge auszuprobieren, die vielleicht erst einmal wenig Aussicht auf Erfolg haben. Nicht zuletzt ist dieser Führungsstil sicherlich einer der Gründe für das sehr gute „Betriebsklima“ und damit auch dafür, dass ich immer gerne an die Uni gekommen bin, um weiter zu forschen.

Als Betreuer hatte PD Dr. Frank Müller für mich einen ähnlich hohen Stellenwert wie Karin. Ging's irgendwo mal nicht weiter, oder passierte irgendwas zunächst seltsam erscheinendes in einem Experiment, hatte Frank immer nochmal einen anderen Blickwinkel auf das Problem zu bieten. Davon abgesehen haben seine Fragen (stille eingeleitet mit den Worten „Ihr seid doch Physiker ...“) in den Mittagspausen oft zu unterhaltsamen Diskussionen geführt.

Dr. Christian Spengler war der wohl beste „Büromitbewohner“ den ich mir vorstellen kann: wenn es nötig war ruhig, aber trotzdem immer bereit über experimentelle, theoretische oder auch alle möglichen anderen Dinge zu reden.

Dr. Hendrik Hähl, Friedrike Nolle und Johannes Mischo waren tolle Kollegen, immer hilfsbereit und verlässlich. Je nach dem, welche Frage mir gerade unter den Nägeln brannte und je nach gewünschter Länge bzw. Ausführlichkeit der erwarteten Antwort war es möglich immer den/die passende/n Ansprechpartner/in auszuwählen.

Monika Schuck und Judith Rech möchte ich für ihre ausgezeichnete Hilfe in allen administrativen Dingen danken. Dank ihnen war von Chemikalienbestellungen bis zu Vertragsangelegenheiten alles kein Problem (zumindest nicht mehr für mich).

Dr. Christian Zeitz, Dr. Samuel Grandthyll, Dr. Nicolas Thewes, Dr. Mischa Klos und Andreas Friedrichs möchte ich hier ebenfalls für die gute Zusammenarbeit danken. Nach ihrem Weggang ist es in der Gruppe deutlich ruhiger (man müsste eigentlich sagen: etwas langweiliger) geworden.

Ich bedanke mich auch bei allen Kooperationspartnern, die mich mit Messungen unterstützt haben, insbesondere bei Jörg Schmauch (Elektronenmikroskopie) und Michael Deckarm (Röntgenbeugung).

Ich danke meinen Eltern für Ihre ständige Unterstützung von Anfang an, und damit ist nicht nur der Anfang des Studiums gemeint. Als ich noch ein Kind war, sagte mein Vater einmal zu mir: „Was du einmal hier drin hast (Er tippte sich dabei mit dem Zeigefinger gegen die Stirn), das kann dir nie wieder jemand wegnehmen.“ Ich glaube dieser Satz hat mich sehr geprägt und mich stets motiviert, immer Neues zu lernen.

Die für mich persönlich wichtigste Person kommt nun ganz zum Schluss: Kirstin Kochems ist seit nun mehr als 11 Jahren immer für mich da. Sie hat sich während der letzten Jahre oft meine Beschwerden anhören müssen, wenn (mal wieder) ein Experiment nicht funktioniert hat, doch hat sie mir irgendwie immer wieder die Hoffnung gegeben, dass es vielleicht beim nächsten Versuch besser läuft. Ich hoffe, sie ist noch viele weitere Jahre an meiner Seite, um diese Wirkung auf mich haben zu können.

Ohne euch alle wäre ich niemals so weit gekommen ... *Danke!*

Thomas